NOTE TO USERS

Page(s) not included in the original manuscript and are unavailable from the author or university. The manuscript was scanned as received.

48

This reproduction is the best copy available.

UMI®

ELECTROCHEMICAL OSCILLATIONS DURING THE ANODIC OXIDATION OF SULFIDE

A Thesis

.Presented to

The Faculty of Graduate Studies

of

Lakehead University

by

BRAD MILLER

In partial fulfillment of requirements

for the degree of

Masters of Science

August 2005

Your file Votre référence
ISBN: 978-0-494-15635-3
Our file Notre référence
ISBN: 978-0-494-15635-3

Abstract

Sulfide is most often encountered as a waste product of the pulp and paper, petroleum, and mining industries. Organic decomposition is another major source of sulfide. During my M. Sc. program, I have studied electrochemical oxidation of aqueous sulfide on Pt electrodes as well as on IrO_2-based electrodes using a number of electrochemical methods (*e.g.*, cyclic voltammetry, cyclic and linear galvanic voltammetry, differential capacitance, chronoamperommetry, chronopotentiommetry, galvanostatic technique, and electrochemical impedance spectroscopy (EIS)) and surface analytical techniques such as scanning electron microscopy (SEM) and energy dispersive X-ray spectroscopy (EDS).

Investigating electrochemical oscillations plays an important role in nonlinear dynamic studies. During the oxidation of sulfide on a platinum electrode we observed current oscillations and two distinct potential oscillations (Oscillation α and Oscillation β) as well as bistability features. Two peaks are observed in the CV curve when scanning the potential from −0.8 to +1.8 V. The small peak is located in the potential range between −0.5 and 0.0 V, while the large one is located between 0.6 and 1.4 V. The current oscillations occur within the large peak potential range and are likely caused by the periodic formation and removal of platinum oxide and sulfur deposits. Our EIS studies show that both Oscillation α and Oscillation β can be classified as hidden negative differential resistance (HNDR) oscillators. The formation and removal of sulfur on the Pt surface, switching the direct oxidation of S^{2-}/HS^- to polysulfides off and on, are responsible for Oscillation α, which occurs at low current densities (below 10 mA/cm^2). Oscillation β appears at high current densities and it may be due to the synergic effect of

sulfur formation/removal combined with oxygen evolution on the Pt oxide surface. The well-defined bistability features are caused by the change of the electrode surface states; in the low potential region sulfide is oxidized on a platinum surface, while in the high potential region platinum oxides are formed and sulfide is oxidized on a platinum oxide surface.

The above mentioned electrochemical techniques were also used to study the oxidation of sulfide on a microstructured oxide electrode Ti/Ta_2O_5-IrO_2. Our surface analysis illustrated that the Ta_2O_5-IrO_2 oxide layer has a "cracked mud" structure, typical of oxide electrodes prepared from the thermal decomposition technique, with oxide particles, sitting on the top of the electrode surface. For the first time, two distinct galvanostatic potential oscillations, named as Oscillation A and Oscillation B, are observed during the electrooxidation of sulfide on an oxide electrode. The appearance of these features strongly depends on the applied current densities. Oscillation A, located in the low current region, has larger amplitudes and much smaller frequencies than Oscillation B which occurs in the high current region. Our EIS studies indicate that both Oscillation A and Oscillation B can be classified as HNDR oscillators with oxygen evolution involved. Oscillation A is caused by the variation of the S^{2-}/HS^- surface concentration from diffusion-limited depletion by oxidation and from convection-induced replenishment by periodic oxygen evolution. Oscillation B is due to the synergic effect of sulfur formation/removal and constant oxygen evolution.

The impact of current density, concentration and temperature on the potential oscillations observed during the anodic oxidation of sulfide on Ti/Ta_2O_5-IrO_2 oxide electrodes was investigated. Raising current density increases the frequency of oscillations

as well the onset potential. Raising either concentration or temperature yields a significant increase in current density prior to the onset of potential oscillations. The activation energy for electrochemical oxidation of sulfide was estimated from temperature studies to be 24 kJ/mol. Potential oscillations were found to have a detrimental impact on electrode lifetime.

Acknowledgements

First and foremost I would like to express my utmost gratitude to my supervisor Dr. Aicheng Chen for his continuous and unwavering support. His insight and patience throughout this project have made my experiences incredibly rewarding.

I would also like to express my thanks to my advisory committee, Drs. S. Kinrade and M. Rappon for their willing and able assistance. I would also like to thank the Department of Chemistry for their continuous support over the past two years.

As well, I would like to extend thanks to my co-workers, both former and current, in Dr. Chen's lab group for their assistance and support; Dan LaRussa; Stephanie Nigro; Fang Wu; Kallum Koczkur; Dr. Xinsheng Peng; Linda Bakovic; Dr. Sreekumari Kurissery; Dr. Songquin Lui; Fengling Cheng; and Peter Holt-Hindle.

Additionally, I would like to express my gratitude to Al Mackenzie for his assistance in imaging and analyzing samples, Ainsley Bharath and Debbie Leach for their technical expertise and Ed Drotar for his work in the Science workshop.

Finally, I would like to thank my parents for their constant encouragement and support.

Table of Contents

List of Figures

List of Tables

List of Symbols and Abbreviations

A	Ampere
Cdl	Double layer capacitance
Cf	Capacitance of the oxide film
CNDR	Coupled negative differential resistance
CA	Chronoamperometry
CP	Chronopotentiometry
CPE	Constant phase element
CV	Cyclic Voltammetry
DSA®	Dimensionally stable anode
E	Potential
Ea	Activation Energy
EDS	Energy dispersive spectrometry
EIS	Electrochemical impedance spectroscopy
F	Faraday constant
GS	Galvanostatic technique
HB	Hoph bifurcation
HNDR	Hidden negative differential resistance
HS^-	Hydrosulfide
I	Current
j	Current density
k	Rate constant
LGV	Linear galvanic voltammetry

NDR	Negative differential resistance
Rct	Charge transfer resistance
Rf	Resistance of the oxide film
R	Universal gas constant
S^{2-}	Sulfide
SEM	Scanning electron microscopy
SCE	Saturated calomel electrode
S_x^{2-}	polysulfides
T	Temperature
Ta-Ir	Ta_2O_5-IrO_2
V	Voltage/potential
V vs SCE	Voltage vs saturated calomel electrode
Z_r	Real impedance
$-Z_i$	Imaginary impedance
α_T	Transfer coefficient at constant temperature
ΔV	Applied cell potential difference
ΔE	Equilibrium potential
ΔV_Ω	Voltage drop due to solution resistance
ΔV_t	Voltage drop due to change in electrode stability
η_a	anodic overpotential
η_c	cathodic overpotential

Chapter 1

1. Introduction

Chemically reacting systems exhibit interesting steady-state and dynamic behaviors such as simple and complex periodic oscillations, quasiperiodicity, and chaos. Electrochemical oscillations are attractive in nonlinear dynamic studies as one can easily monitor the change of both current and voltage. There are probably more examples of oscillating systems in electrochemistry than in any other area of chemistry. The following sections will outline the relevant theory associated with electrochemical oscillations, focusing on the classification of different oscillators with the aid of electrochemical impedance spectroscopy. Also, a discussion of dimensionally stable anodes (DSA®) involving common fabrication methods, morphological properties, and general composition characteristics will be presented. Finally, the electrochemical oxidation of sulfide will be reviewed with a focus on some of the observations noted during its oxidation as well as the electrode materials used.

1.1. Electrochemical Oscillators

The observation of spontaneous periodic variations in potential or current during electrochemical reactions was first reported in the late 1800's [1]. Since this first observation, numerous other systems have been shown to exhibit oscillatory phenomenon either at constant potential or current. These systems include the anodic dissolution of a variety of metals (Fe, Cu, Ni, Sn, and Zn) [2,3], the anodic oxidation of small organic molecules and hydrogen [4-10]. Oscillations have also been observed for a number of cathodic processes, including the reduction of

hydrogen peroxide, persulfate and iodate [11-17]. Although oscillations have been observed for a number of years, the underlying processes involved were poorly understood. The ease with which the current or electrode potential can be controlled during an electrochemical experiment has attracted a considerable amount of interest from researchers in the field of non-linear chemical kinetics. Several methods derived from the theory of dynamic systems and non-linear science have been applied, giving rise to a greater understanding of the origins of non-linearity generated in electrochemical systems [18]. Two variables are required for an oscillation to occur: a positive and negative component. If a system only contains one variable bistability can occur (where the system can be in one of two stable stationary states, for example one at high current density and another at low current density). To generate bistability, the mechanism of the reaction must contain a self-enhancing step known as a positive feedback loop [18]. The inclusion of a second feedback loop acting in a negative manner then allows for the appearance of oscillations.

Classification of electrochemical oscillations under both potentiostatic and galvanostatic control has led to a greater understanding of the conditions required to generate the observed instabilities. Initially, oscillations were characterized as either chemical or electrochemical in nature [19]. This has since been further expanded by researchers in the field of non-linear chemical kinetics. Their use of the theory of dynamical systems and non-linear science, most notably bifurcation theory, has allowed for a systematic determination of the origin of a variety of non-linear dynamical phenomena found in electrochemical systems [20]. This

discipline of science, in conjunction with electrochemical impedance spectroscopy, has allowed for significant expansion and classification of electrochemical oscillators. It has been determined that the unstable behavior is linked to the negative impedance characteristics of the faradaic processes occurring at the electrode surface [20]. The occurrence of negative impedance does not necessarily indicate the generation of oscillations or instabilities since it is dependent on the manner in which the electrode is coupled electrically to the rest of the system[20].

1.2. Classification of electrochemical oscillations

As mentioned oscillators were origionally classified as being either chemical or electrochemical in nature. In 1996 Koper suggested a classification system based on the experimental control mode as well as the impedance spectra where the oscillatory mechanisms included at minimum one autocatalytic variable that was either a chemical species or an electrical quantity [21]. Koper proposed three classes of oscillators. The first class contained current oscillations which occur under truly potentiostatic conditions. The second class pertained to oscillations which occur under potentiostatic conditions with a large ohmic drop. The third class contained oscillations which occur under both potentiostatic and galvanostatic conditions with a large ohmic drop present [22].

In the case of the first class of oscillator, the feedback on to the external circuit is not an essential component of the oscillatory mechanism and these oscillations will still occur under potentiostatic conditions providing that the ohmic drop can be minimized and thus neglected. Koper et al. pointed out that

the instability mechanism that give rise to oscillations in such systems must be purely chemical in nature [23]. These instabilities can be related to autocatalytic surface chemistries, adsorbate-induced surface phase transitions, or non-ideal adsorption isotherms [22]. Therefore, if every effort to minimize the ohmic drop is taken (minimize electrolyte resistivity or electrode surface area) and the oscillation disappears then it does not belong to the first class [22]. Due to the difficulties associated with minimizing the ohmic drop there is some dispute as to how many systems, if any, belong in this class of oscillator. However, even with the difficulties associated with minimizing the ohmic drop, there are a few systems which are thought to be related to or exhibit "class 1" oscillatory behavior. These include: electrocrystallization of zinc in the Leclanché cell; the electrodissolution of iron in nitric acid; and oscillatory electrodissolution of silicon in fluoride media [22].

The second class involved oscillations under potentiostatic conditions with a large ohmic drop. The conditions for the appearance of this type of oscillator include a region of negative slope in the steady-state current-voltage curve. Also, the current oscillations occur exactly in the area of the negative slope on the curve when a large enough ohmic potential drop is present. The negative polarization slope is thought to be related to inhibition of the electron transfer process via electrode passivation or electrostatic repulsion. Under galvanostatic conditions, this type of system will only exhibit bistability as opposed to oscillations [22].

The final class of oscillation proposed by Koper was oscillations under both galvanostatic and potentiostatic control with a large ohmic drop. This class

was further divided based on its respective mechanistic character, namely the presence or absence of "hidden" negative faradaic impedance (where the system exhibits positive real impedance at high frequencies, negative real impedance for intermittent frequencies and reverts back to positive real impedance when $\omega = 0$) [22]. They have since become known as negative differential resistance (NDR) and hidden negative differential resistance (HNDR) oscillators and comprise the bulk of the known electrochemical oscillators described in literature.

1.2.1. Negative differential resistance oscillators

The conditions for the appearance of a NDR type oscillator involves the double layer potential acting as an autocatalytic variable with chemical instabilities typically absent. In the case of a NDR, the current oscillations only appear on the negative slope of a I/Φ curve and, at vanishing ohmic resistance, a N-shaped voltammetric profile is generated that prevents oscillations from occurring under galvanostatic conditions and giving rise to bistable behavior under current controlled conditions [24].

1.2.2. Hidden negative differential resistance oscillators

Although the conditions leading to the appearance of a HNDR are the same as those for a NDR, the behavior of these two oscillators is significantly different. A HNDR's current oscillations can occur on a positive slope of an I/Φ curve and will have a potentiostatic Hoph Bifurcation (HB) associated with it [21]. A HNDR oscillator also generates galvanostatic potential oscillations, which indicates that the oscillation is hidden on the I/Φ curve and, therefore, working on a quick time scale [21]. It was also found to be necessary to divide the HNDR

class into three sub classes: potential dependant source of the inhibitor; the H_2/formic acid group; and the IO^{-3} group [24]. This has since been revised once it was determined that the mechanism involved with the iodate group was associated with mass transport/convection as opposed to a HNDR mechanism [25]. The first sub class requires the assumption of two conditions: the adsorption of the chemical species is potential dependant; and the source term of the slow, inhibiting species is also potential dependant [21]. The second sub class generally requires an independent current carrier that exhibits a normal potential regulation and an N-shaped profile during a cyclic voltammogram. This current carrier is created by rapid production and removal of an essential chemical species as it blocks active sites. At this point a second essential chemical species is added to the mechanism which generates the negative feedback and the production/removal of this second species is normally potential dependant [21]. The behavior of the second species may completely cover up the N-shaped profile of the NDR, thus generating a hidden NDR that is hidden for all potential ranges.

1.2.3. Coupled negative differential resistance oscillators

Further investigations into electrochemical oscillatory systems by Mukouyama et al. led to the development of another class of oscillator known as coupled negative differential resistance oscillator (CNDR) [11]. Investigating the oscillations during the reduction of H_2O_2 in acidic media led to the development of this new class of oscillation since previous mechanisms could not fully account for one of the observed oscillations. They explained the observed oscillation using the idea of active and non-active areas on the electrode surface where the

coupling of an electrochemical reaction in a potential region associated with positive differential resistance occurs with an NDR in another potential region giving the electrochemical oscillation. In addition, this oscillator also requires the presence of surface inhomogeneities (i.e. atomically rough surfaces) as well as solution stirring by an electrochemical reaction [11].

1.2.4. Mass transport/convection

The most recent oscillator was proposed by Li et al. to explain the origin of potential oscillations during iodate reduction in alkaline solution [17, 25]. Previous work with this system had demonstrated the presence of an HNDR oscillator [21], but Li et al. did not feel that classifying it solely as an HNDR oscillator took into account the impact of periodic gas evolution on the potential oscillation. They proposed a pair of overlapping positive and negative feedback loops involving the diffusion-controlled depletion of iodate at the electrode surface and the convection induced replenishment (by periodic hydrogen gas evolution) of iodate to account for the potential oscillations. Furthermore, they proposed that the presence of a crossing cycle in a CV which indicate the presence of overlapping positive and negative feedback steps maybe a better indicator for the presence of oscillatory phenomena with this type of system then the observation of negative impedance [26].

1.3. Dimensionally Stable Anodes

Dimensionally stable anodes (DSA®), also known as (mixed) oxide electrodes, are considered one of the greatest technological breakthroughs in electrochemistry in the 20th century [27]. It is interesting to note that oxide electrodes were more

or less unknown in electrochemistry and were undisclosed (while industry was testing their performance) for at least 7 years after their discovery [28]. Prior to their discovery, significant research was put forth in relation to metallic anodes, most notably platinized Ta and Ti [29]. Unfortunately, from an industrial standpoint, these anodes demonstrated numerous limitations: high electrode potential, high wear rate, and the occurrence of passivation with operation time [30]. The afore mentioned problems led to the development of metallic oxide coatings as anode catalysts for both chlorine and oxygen evolution reactions. DSA® consisting of both RuO_2 and IrO_2 as electroactive components demonstrated marked improvement over previous anodes in that they exhibited lower overpotential for both chlorine and oxygen evolution reactions compared to conventional anodes.

DSA® are generally comprised of oxides prepared by the thermal decomposition technique from chloride precursors. These chloride precursors are dissolved in an appropriate solvent and spread onto a metallic support. The metallic support is generally a valve metal (Ti, Ta, Zr etc.). Ta demonstrates the highest service life in acidic medium with a lifetime of 1700 hours [31]. Unfortunately, Ta has two significant drawbacks: a density of 16 654 kg m^{-3} (making it difficult for substrate pretreatment); and a high cost (in excess of \$740.00 kg^{-1}). This makes Ti one of the more popular choices for a substrate since it delivers good stability, its pretreatment is relatively easy, and it is fairly inexpensive (~\$250.00 kg^{-1}) [32]. The substrate is pretreated prior to application of the oxide precursor to give the appropriate support structure. This is

accomplished by polishing then acid etching the substrate to give better adhesion of the coating particles and a more consistent morphology by creating a uniform surface for the coating to be applied [31]. The preparation of a DSA® is normally accomplished by repeated applications of the combined precursor solutions alternated with a high temperature calcination step. Once the desired coating load is met, the oxidation process is completed by a final post bake. The selection of an electrocatalyst is driven by its ability to promote the desired reaction. The broad definition of electrocatalysis can be expressed as "the dependence of the electrode reaction rate on the nature of the electrode material" [33]. Depending on the field of application, this term can have different meanings. From a research point of view, it is an avenue to developing a guide to applied problems leading to the development of new materials. Industry views it as the potential to improve existing processes by improving electrocatalysis performance thereby reducing operation costs [33]. The primary target of the electrolytic industry is to generate an applied cell potential difference (ΔV) that lies close to the thermodynamic value as expressed in equation (1.1) where ΔE is the equilibrium potential, η_a and η_c are the

$$\Delta V = \Delta E + \eta_a + \eta_c + \Delta V_\Omega + \Delta V(t) \quad (1.1)$$

anodic and cathodic overpotentials (where the overpotential is the potential necessary to initiate the reaction) , ΔV_Ω is the potential drop due to ohmic drop (IR), and $\Delta V(t)$ is the potential drop related to changes in the electrode stability with time [33]. The changes in electrode stability can be attributed to deterioration of the catalyst, metal support, or the support/catalyst interface.

Therefore reducing η_a and η_c as well as $\Delta V(t)$ are the primary concerns of electrocatalysis with the proper selection of the oxide catalysts being paramount to improve these conditions [33].

The morphology of a DSA® varies depending on the preparation method, precursor selection, the solvent in which the precursor is dissolved, and the time and temperature of calcination [33]. Scanning electron microscopy (SEM) has shown that the oxide films can exhibit "cracked" or "compact", crystalline and amorphous morphologies [34]. In general, DSA® made by thermal decomposition of chloride precursors exhibit the "cracked mud" structure observed by Comninellis et al [35]. The morphology of the oxide layer is thought to contain three interfaces which again relate to the effectiveness of an oxide catalyst. The outer surface (comprised of the oxide/solution macroboundary), the inner surface (derived from penetration of the liquid into intergrain regions and pores), and the oxide layer/support interface. The outer and inner surface are thought to control the effectiveness of the oxide for electrocatalysis and the oxide layer/support interface governs the stability (lifetime) of the electrode which is derived from the potential for the formation of insulating TiO_2 film between the substrate and the oxide layer [33].

The oxide layer of a DSA® normally consists of two components, an active oxide which promotes the electrode reaction and a second oxide which acts as a stabilizer to help the stability of the active component in harsh operating conditions. The stabilizing oxide can either be conducting (addition of IrO_2 to RuO_2) [36] or nonconducting in the case of the addition of TiO_2 to RuO_2 [30].

The addition of a stabilizing agent to the electroactive component can lead to a reduction in the electrocatalytic activity, especially with the addition of non conductive oxides, of the DSA®. However, the addition of non-precious oxides is more attractive due to their significantly lower price. The loss of electrocatalytic activity is more than compensated by the longer operating lifetimes making the DSA economically viable.

1.4. Sulfide chemistry

The removal of sulfide from industrial processes is becoming increasingly important since sulfide compounds are known to have a detrimental impact on many industrial processes. Sulfide, in the form of H_2S, contaminates geothermal brines that are encountered during the drilling of oil wells [37]. In addition, hydrogen sulfide leads to corrosion of metallic components and generate sulfide scales which can plug tubulars, reduce the quality of the produced oil and increase the amount of biocides required to control sulfate reducing bacteria [37]. Sulfides also strongly poison the catalysts used in fuel cells and oil refining [38-39]. Additional sources of sulfide not related to industrial processes are naturally occurring water sources. These include mineral, deep-well, ground, and well water. Analysis for sulfide in these water sources is an important process due to the high toxicity of hydrogen sulfide as well as its organoleptic properties [39]. Although sulfide has numerous detrimental issues associated with it, sulfide in the form of sodium sulfide (as a component of white liquor) is an integral part of the Kraft pulping process. It has also been reported that the addition of polysulfides to white liquor can improve pulp yields by as much as 2% [40].

There are a number of existing techniques for the treatment and removal of H_2S. The treatment of liquid streams employs precipitation and oxidation reactions. Sulfide is either removed as insoluble sulfides of Zn or oxidized to sulfate or elemental sulfur using chromates and nitrites. Depending on the level of H_2S in the system, huge quantities of H_2S scavengers (in some cases up to hundreds of tons per month) are needed to control the problem making such processes expensive and environmentally detrimental [37]. For gas streams, H_2S is normally removed as elemental S using the high temperature (~500 – 700 °C) Claus catalytic process [41]. The use of electrochemistry to treat sulfide in its various forms is an attractive alternative to existing technologies since sulfide/hydrosulfide can be oxidized to sulfur, polysulfides, and oxyanions of sulfur according to the anodic half reactions (E/V vs SCE) listed below [42-43]:

$HS^- + OH^- \rightarrow S + H_2O + 2e^-$	-0.478	(1.2)
$S^{2-} \rightarrow S + 2e^-$	-0.508	(1.3)
$HS^- + 9OH^- \rightarrow SO_4^{2-} + 5\ H_2O + 8e^-$	1.10	(1.4)
$2OH^- + SO_3^{2-} \rightarrow SO_4^{2-} + H_2O + 2e^-$	0.6887	(1.5)
$6OH^- + S_2O_3^{2-} \rightarrow 2SO_3 + 3H_2O + 4e^-$	0.3388	(1.6)
$4OH^- + S_2O_4^{2-} \rightarrow 2SO_3 + 2H_2O + 2e^-$	0.8788	(1.7)
$2S^{2-} \rightarrow S_2^{2-} + 2e^-$	0.2388	(1.8)
$S^{2-} + S_2^{2-} \rightarrow S_3^{2-} + 2e^-$	0.2488	(1.9)
$S^{2-} + S_3^{2-} \rightarrow S_4^{2-} + 2e^-$	0.2788	(1.10)
$S + 6OH^- \rightarrow SO_3^{2-} + 3H_2O + 6e^-$	0.4188	(1.11)

Electrochemical oxidation of aqueous and gaseous sulfide has garnered significant attention for detection and removal/conversion of the highly toxic sulfide species [37, 39, 44-48]. The electrochemical behavior of sulfide has been investigated using different electrode materials, including platinum [40-41, 43, 49-51], graphite [37, 44-47, 52-53], and gold [54-55]. It has been demonstrated that electrochemical techniques including stripping voltammetric analysis [39], high sweep rate linear sweep voltammetry [48], and differential pulse polarography [56] can be used with good accuracy to identify and quantify a number of different sulfur and organosulfur compounds derived from naturally occurring water sources. In addition, the formation of a sulfur layer on the electrode surfaces as well as the production of polysulfides in solution are observed during the anodic oxidation of sulfide. The passive sulfur layer formed on the electrode surface prevents efficient removal/conversion of sulfide from a solution [44-45]. The composition of the produced polysulfides have also been determined experimentally using a range of diffusion coefficients for the various polysulfide ions as well as for the hydrosulfide ion in a ratio to calculate the number of electrons from those reactions. It has been demonstrated that the number of sulfur atoms in the chains can range from as low as 2 to as high as 5 and the stability of the polysulfide species is highly dependent on the pH of the solution [43, 54, 57]. In contrast, adsorbed sulfide/sulfur on noble metal electrodes significantly enhances the electrocatalytic activity of the anodic oxidation of carbon monoxide, formic acid, and methanol [58]. However, the mechanisms of sulfide oxidation and soluble polysulfide ions formation, and the

nature of the deposited sulfur are still not clear. In addition, oxyanions of sulfur, for instance, thiosulfate and sulfate, can also be formed. Thus, further investigation of sulfide oxidation is critical in order to effectively remove sulfide from wastewater streams and to economically convert sulfide into polysulfide for the white liquor of the kraft pulping process.

1.5. Scope of the Thesis

Chapter 2 will describe some of the electrochemical techniques used in this study as well as the surface analysis techniques used to characterize mixed oxide electrodes. Preparation procedures for all electrodes used will also be presented in chapter 2. Chapters 3 to 5 will present the experimental results. Chapter 3 describes the oscillatory instabilities observed during the electrochemical oxidation of sulfide on a platinum electrode. An oscillation mechanism to account for the observed oscillations will also be presented in this chapter. Chapter 4 shows the results observed for the potential oscillations during the electrocatalytic oxidation of sulfide on microstructured Ti/Ta_2O_5-IrO_2 electrodes Chapter 5 will describe the influence of both temperature and Na_2S concentration on the potential oscillations that are observed during the electrochemical oxidation of sulfide on the microstructured Ti/Ta_2O_5-IrO_2 electrode. Finally, Chapter 6 will provide a summary of the results and conclusions.

Chapter 2

Experimental Section

2.1. Electrochemical techniques

A wide variety of electrochemical techniques were used in this study including cyclic voltammetry, cyclic and linear galvanic voltammetry, chronoamperommetry, chronopotentiommetry, differential capacitance, galvanostatic technique, and electrochemical impedance spectroscopy were used in this study. The following sections outline the relevant theory and applications of electrochemical impedance spectroscopy.

2.1.1. Theory

All discussions involved in this section will be restricted to simple circuits to simplify the mathematics involved. Ohm's law, which can be expressed as

$$E = IR \qquad (2.1)$$

defines the relationship between potential and current. If we consider ac signals, the sinusoidal voltage can be expressed using the angular frequency

$$e = E \sin(\omega t) \qquad (2.2)$$

where ω is the angular frequency and is 2π times greater than the conventional frequency [59]. The voltage is normally considered as a phase quantity so that the observed potential at any time t is a component of the amplitude E and the frequency of rotation ω [59]. To compare related sinusoidal signals (ac potential and current), they can be expressed as separate phasors (E' and I') rotating at the same frequency that are not normally in phase (i.e. separated by a phase angle ϕ).

If the phasor E' is the reference signal and ϕ is measured with respect to it then the current can be expressed as

$$i = I \sin(\omega t + \phi) \qquad (2.3)$$

If the frequency is constant, the rotation component can be dropped from phasor diagrams and the phasors expressed as vectors with a common origin and separated by the appropriate angles [59].

Applying this information to simple circuits, a pure resistance with a sinusoidal voltage applied of $e = E \sin(\omega t)$, the current can be expressed as $I = (E/R)\sin(\omega t)$ due to Ohm's law, or in terms of phasor notation

$$I' = E'/R \qquad (2.4)$$

If a pure resistor is replaced with a pure capacitance the current can be written as

$$i = \omega CE \cos(\omega t) \qquad (2.5)$$

or

$$i = (E/X_c) \sin(\omega t + \pi/2) \qquad (2.6)$$

where the capacitive reactance (X_c) is equal to $1/\omega C$. In this case the phase angle is now $\pi/2$ as opposed to 0 for the case of a pure resistance and the current now leads the voltage [59]. Thus, it is a good idea to include complex notation to express phasors and they are multiplied by $j = \sqrt{-1}$. Even though the current's phase angle is measured with respect to the voltage, the voltage phasor E' can still be expressed for a pure capacitance

$$E' = -jX_cI' \qquad (2.7)$$

where $-jX_c$ takes the place of the resistance in Ohm's law [59].

At this point, a simple circuit can be constructed with a pure resistance and pure capacitance in series with an applied voltage (E') which must equal the sum of the voltage drops across each component. Thus,

$$E' = E'_R + E'_C \qquad (2.8)$$

$$E' = I'(R - jX_c) \qquad (2.9)$$

$$E' = I'Z \qquad (2.10)$$

This expression allows for the link between voltage and current through Z which is called the impedance and is equal to $R - jX_c$. Generally, the impedance is expressed as

$$Z(\omega) = Z_{Re} - jZ_{Im} \qquad (2.11)$$

where $Z_{Re} = R$ for a pure resistance and $Z_{Im} = 1/\omega C = X_c$ for a pure capacitance and the magnitude of the impedance is

$$|Z|^2 = (Z_{re})^2 + (Z_{Im})^2 \qquad (2.12)$$

Another method for the analysis of ac circuits is the idea of admittance (Y). Admittance is simply the inverse of impedance and in some cases may be easier to work with since procedures used to model circuits often involve the conversion of a series circuit to a parallel circuit and vice versa [60]. With this in mind admittance can be expressed as

$$Y = 1/Z = Y_{Re} + jY_{Im} \qquad (2.13)$$

and can also allow Ohm's law to be rewritten as

$$I' = E'Y \qquad (2.14)$$

This is a useful term when considering parallel circuit elements since the overall admittance is simply the sum of the individual admittance elements [59].

2.1.2. Equivalent circuits

To understand the behavior of an electrochemical system from an impedance standpoint it is often useful to express the resulting impedance in the form of an equivalent circuit. The equivalent circuit is an electrical representation of the behavior of the system at different potentials or currents. Table 2.1 is comprised of the available elements that can be used in the construction of an equivalent circuit [61].

Table 2.1: Available elements for equivalent circuits.

Notation	Identification	Notation	Identification
R	Resistance	C	Capacitance
CPE	Constant Phase Element	W	Warburg Element (Diffusion)
L	Inductance	T	Tangent Hyperbolic (Diffusion)
G	Gerischer Impedance	O	Cotangent Hyperbolic (Diffusion)

The simplest electrochemical cell essentially behaves like a resistor in series with a capacitor and can be expressed as shown in figure 2.1, where Rsol and Cdl represents the resistance of the solution and capacitance of the double layer respectively [61].

Figure 2.1: Equivalent circuit representation of a simple electrochemical cell.

When a faradaic process occurs at the electrode there is the generation of a faradaic impedance that is in parallel with the double layer. If the reaction is irreversible, then the faradaic impedance can be considered a pure resistance and

is called the charge transfer resistance and would be reflected in the revised equivalent circuit shown in figure 2.2.

Figure 2.2: Equivalent circuit for a simple faradaic process.

As in figure 2.1, Rsol and Cdl represent the solution resistance and double layer capacitance, and the new term Rct represents the resistance to charge transfer for the faradaic process. The equivalent circuit shown in figure 2.2 is generally referred to as the Randles circuit and is most often used as a starting point for modeling of an impedance set. The Randles circuit is also used for diffusion controlled, low frequency processes for which it may be expanded to include the Warburg impedance as shown in figure 2.3. The Warburg impedance is encountered whenever diffusion effects dominate the electrochemical reaction mechanism and can be easily identified by a 45° straight line in an impedance plots [61-62].

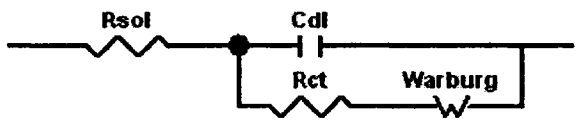

Figure 2.3: Equivalent circuit for a Randles circuit with diffusion control.

2.1.3. Representation of impedance data

The observed results from EIS experimentation can be expressed in a number of different manners with the most commonly reported being the Nyquist and Bode Plots. The Nyquist plot (also known as Cole-Cole or complex impedance plane

plot) is expressed by plotting the imaginary impedance component (Z_{Im}) against the real impedance component (Z_{Re}) for each frequency [62]. The main advantage of the Nyquist plot is the ease with which the ohmic resistance can be evaluated if data is acquired at high enough frequency. The disadvantage is that frequency dependant information cannot be easily derived from the plot [62]. The other common method of presenting impedance data is the Bode plot. The Bode plot uses the absolute impedance (eq 2.12) and the phase shift ϕ (of the impedance) as a function of the applied frequency. This method of presenting impedance has its advantages. It is easier to see how impedance is dependant on frequency and since frequency is plotted logarithmically, a wide range of frequencies can be plotted on one graph with each decade given equal weight [62]. The largest disadvantage associated with the Bode plot is that the shape of the curve can change if the values for the circuits change. The Nyquist and Bode plots will be discussed in greater detail in section 2.3. Other methods of plotting impedance data include Z_{Re} vs ωZ_{Re} or more commonly known as the Randles plot which for simple Randles circuit has the advantage of being a straight line and allows for a more reasonable fit for scattered data points than a Nyquist plot [62]. Also if the polarization resistance is determined, it is then easy to determine the capacitance for the system. Another plotting system that is sometimes encountered involves plotting Y_{Im}/ω vs Y_{Re}/ω, also known as a capacitance plot. This method is especially useful when circuits elements are in parallel [62]. The capacitance plot allows for easy identification of the capacitance since it only has an imaginary component which is independent of frequency and thus appears as a single point

on the graph and only requires extrapolation to the y-axis. Comparatively, the resistance only has a real component and is frequency dependant which means that it would show up as a straight line on a capacitance plot [62]. Although both the Randles and capacitance plots have their uses, they are generally encountered in specific cases including Randles or parallel type circuits and are not listed nearly as often as the Nyquist or Bode plots in literature.

2.1.4. Experimental applications

EIS experiments can be performed under either constant potential or constant current. If the constant potential case is considered, a small signal perturbation (time dependant) is applied to the equilibrated system to shift it slightly away from its equilibrium position. The applied perturbation must be kept small to ensure that the response of the system to the perturbation will remain linear [60]. The applied signal can be a single wave or a number of waves containing varying amplitudes, frequencies and phases which can be generated by potential steps, pulse shaped signals or noise [60]. Generally speaking, signal amplitudes of 10 mV or smaller are required to maintain linearity of the system, especially in low frequency applications. In high frequency applications, the signal can have a higher amplitude since the equivalent circuit can be said to have behavior similar to that in figure 2.1. Subsequently the bulk of the amplitude signal is consumed by the potential drop of the solution [60]. There are two techniques for the experimental measurement of impedance the time domain and frequency [63]. The time domain technique uses a frequency rich signal that acts as a perturbation and the cell response is measured as a function of time. The

resulting impedance data are then converted using a transformation algorithm to the frequency domain [63]. The frequency technique uses a sine wave perturbation and the impedance is obtained for a single frequency. This means that numerous measurements must be conducted over a wide frequency range, making the method far more time consuming than the time domain technique [63]. The above information outlines the methods for obtaining impedance data but external input is still required to determine potentials to be studied. This is normally accomplished by examining results obtained from cyclic voltammetry experiments for appropriate areas of interest. These may include, but are not limited to, positive and negative slopes, build up of material on the electrode surface, or gas evolution.

2.1.3. Modeling

Currently, several commercial programs are available that can model impedance plots quite effectively which only require reasonable starting points. The general method employed in these programs involves the generation of an equivalent circuit, from the elements listed in table 1, that will hopefully imitate the impedance data set fairly well when values for the parameters are loaded into the program [60]. The second step involves checking the validity of the impedance data using the Kramer-Kronig rule check. This system is derived from the Kramers-Kronig frequency domain transformations. These transformations can allow for the components of one impedance to be calculated from another, the determination of the phase angle from the magnitude of the impedance or the

polarization resistance from the imaginary resistance using the equations listed below [60].

$$Z_{Re}(\omega) - Z_{Re}(\infty) = (2\omega/\pi)_0\int^{\infty} [(xZ_{Im} - \omega Z_{Im}(\omega))/(x^2 - \omega^2)]dx \quad (2.15)$$

$$Z_{Re}(\omega) - Z_{Re}(0) = (2\omega/\pi)_0\int^{\infty} [((\omega/x)Z_{Im}(x) - \omega Z_{Im}(\omega))/(x^2 - \omega^2)]dx \quad (2.16)$$

$$Z_{Im}(\omega) = -(2\omega/\pi)_0\int^{\infty} [Z_{Re}(x) - Z_{Re}(\omega))/(x^2 - \omega^2)]dx \quad (2.17)$$

$$\delta(\omega) = -(2\omega/\pi)_0\int^{\infty} [(\log|Z|)/(x^2 - \omega^2)]dx \quad (2.18)$$

$$\delta(\omega) = (2/\pi)_0\int^{\infty} [(Z_{Im}(x))/x]dx \quad (2.19)$$

The main conditions for the application of the Kramers-Kronig transforms to validate an impedance data set are (a) the impedance must have finite values for $\omega \rightarrow 0$ and $\omega \rightarrow \infty$, and (b) all intermediate values must be continuous and finite valued functions [60]. The final step employs the use of complex non-linear regression least squares (CNRLS) method of adapting the model parameters to the measured data. In this step both the experimental and the optimized calculated data are plotted and compared (normally using the Nyquist and Bode Plots) to determine how closely the optimized data set compares to the experimental values for the frequency range in question [60]. It should be noted that although computer simulation has significantly decreased the time required to determine the best fit for a set of impedance values, it is still crucial to start with a reasonable equivalent circuit with the minimal amount of circuit elements to

generate a reasonable comparison with the calculated data and maintain low errors.

2.2. Electrode preparation

2.2.1. Ti/Ta_2O_5-IrO_2 Anode

The Ti substrate (area = 1.0 cm^2) was first polished using silicon carbide grit 600 powder and then by grade 1 diamond compound (particle size less then 2 μm). The polished Ti substrate was then etched in a 32% HCl solution at 85 °C for 15 minutes. The coating solution was prepared by mixing the chloride precursors of Ta and Ir. The combined coating solution was then brushed onto the pretreated Ti substrate. The solvent was evaporated at 80 °C under an air stream; and then calcinated to form the respective oxides at a temperature of 500 °C for 10 minutes. This process was repeated until a desirable coating load was obtained. A final post bake at 530 °C completed the preparation procedure.

2.2.2. Pt wire/Pt coil (counter electrode)

The Pt wire (A = 1.0 cm^2) was attached to a Ti lead and was flame annealed and quenched using pure water prior to experimentation . The counter electrode (A = 10.0 cm^2), Pt wire, was flame annealed and quenched with pure water.

2.3. Surface analysis

Analysis of the substrate and coating was accomplished via scanning electron microscopy (SEM) and X-ray dispersive spectrometry (EDS) using a JEOL 5900LV.

2.4. Electrochemical experiments

The three electrode cell system used in this study is described in ref [64]. Cyclic voltammetry (CV), linear galvanic voltammetry (GL), chronoamperommetry (CA), and chronopotentiommetry (CP) were performed using a Solartron Analytical SI 1287 electrochemical interface with data acquisition accomplished with Corrware electrochemical software. Electrochemical Impedance Spectroscopy (EIS) was performed with a Solartron Analytical 1252A frequency response analyzer in conjunction with the 1287 electrochemical interface. Zplot electrochemical software was used to acquire the impedance data. Unless otherwise stated, the amplitude of the AC modulation potential was 10 mV and the frequency range selected was 40 KHz to 25 mHz.

Lifetime tests were conducted using an Arbin Instruments four-channel potentiostat/galvanostat with data acquisition accomplished using Arbin Instruments MITS Pro software.

2.5. Solution Preparation

Sulfide solutions of 2.0, 1.0, 0.6M, and 0.3 M were prepared by dissolving the appropriate mass of reagent-grade sodium sulfide crystal $Na_2S \cdot 9H_2O$ (Caledon Laboratories Ltd.) in pure water obtained from a NANOpure® Diamond™ UV ultrapure water purification system (18.2 MΩ cm). Solutions of

1.0 M and 0.65 M reagent-grade sodium hydroxide (Anachemia) of the same concentrations listed above were prepared in the same manner for comparison purposes. Prior to experimentation, all solutions were deaerated with ultrapure argon (99.9995%) to remove dissolved oxygen, and argon was passed over the solution during the experiment.

Chapter 3

Oscillatory Instabilities during the Electrochemical Oxidation of Sulfide on a Pt Electrode

3.1 Current oscillations during the sulfide oxidation

3.1.1 Cyclic voltammetry and linear voltammetry

Cyclic voltammetry (CV) was used for the general characterization of the electrochemical behavior of sulfide on a Pt electrode. Fig. 3.1 shows the effect of potential sweep rate and sulfide concentration on the CV curves during sulfide oxidation. Two CV curves from -0.8 V to 1.8 V/SCE recorded in 1.0 M Na_2S (solid line) and 1.0 M NaOH (dotted line) solutions at a sweep rate of 20 mV/s are shown in Fig. 3.1a. As seen by the CV curve in the sodium hydroxide solution (dotted line), oxygen evolution occurs at around 0.8 V/SCE and, by further increasing the electrode potential, the current of the oxygen evolution increases linearly. In the presence of sulfide (solid line), sweeping the potential from -0.8 V to 1.8 V/SCE, a broad hump occurring in the negative potential range is observed in the CV, followed by a large and wide peak. The inset to Fig. 3.1a presents a CV curve in the range between −1.1 and 0.4 V/SCE recorded in a 1.0 M Na_2S solution at a sweep rate of 20 mV/s. It is obvious that the strong adsorption of sulfide on the Pt electrode surface inhibits hydrogen adsorption. The broad hump starting at around −0.6 V corresponds to the oxidation of sulfide to sulfur, which can be converted to polysulfides [41]. Fig. 3.1b presents the CV curve measured in a 1.0 M Na_2S solution at a sweep rate of 5 mV/s; the current density of all the peaks becomes smaller compared to those in Fig. 3.1a. In addition, a new peak centered at 1.37 V appears when sweeping back from 1.8 to -0.8 V. Further decreasing the potential scan rate to 1 mV/s, current

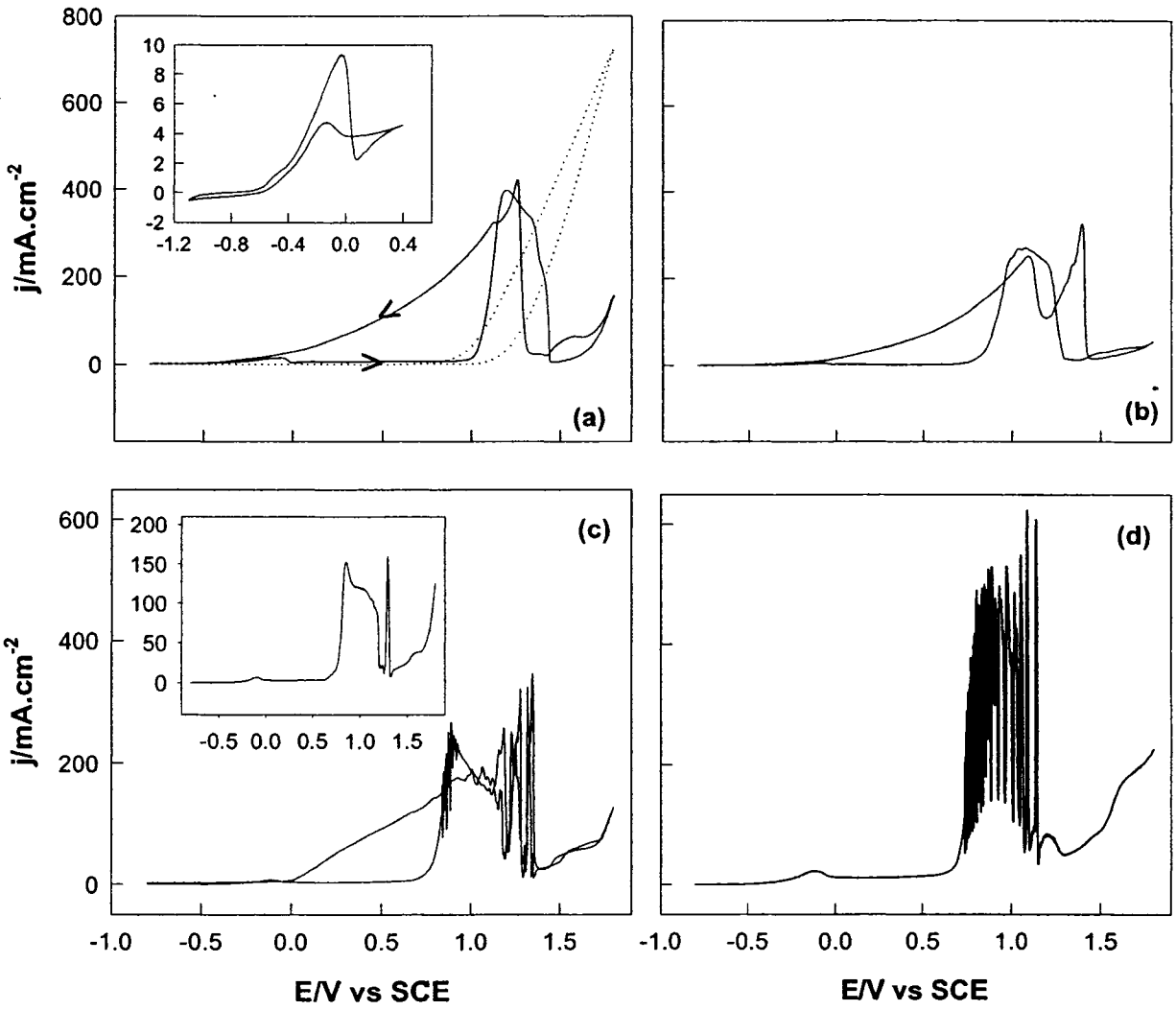

Figure 3.1. Cyclic voltammograms (CV) of (a) 1.0 M Na_2S (solid line) and 1.0 M NaOH (dotted line) at a sweep rate of 20 mV/s; (b) 1.0 M Na_2S at 5 mV/s; (c) 1.0 M Na_2S at 1 mV/s. Linear voltammograms (LV) of (d) 2.0 M Na_2S at 1 mV/s; and the inset to Fig. 1c: 0.65 M Na_2S at 1 mV/s. Inset to Figure 1a is a CV curve of 1.0 M Na_2S from −1100 mV to +400 mV.

oscillations are observed in the CV curve as seen in Fig. 3.1c. The current oscillations are located in the large peak range; their amplitude and frequency depend on the applied electrode potential. The inset to Fig. 3.1c presents a linear voltammetric (LV) curve measured in a 0.65 M Na_2S solution from -0.8 V to 1.8 V at 1 mV/s. Instead of the current oscillations, only one large spike centered at 1.3 V is observed. On the other hand, when we increase the sodium sulfide concentration to 2.0 M, as seen in Fig. 3.1d, current oscillations with higher frequency and larger amplitude are observed in the LV curve compared to the oscillations presented in Fig. 3.1c. The above results show that the current oscillations observed during the sulfide oxidation strongly depend on the potential sweep rate and the sulfide concentration.

3.1.2 Chronoamperommetric study and stirring effect on the current oscillations

Chronoampermmetric (CA) technique was employed to determine the behaviors of the current oscillations. Fig. 3.2 is comprised of three CA curves recorded in 1.0 M Na_2S at three different electrode potentials: (a) 1.0 V, (b) 1.1 V and (c) 1.3 V. The frequency of the current oscillations increases with the increment of the potential from 1.0 V to 1.3 V. The amplitude of the current oscillations at these potentials is similar, around 300 mA/cm^2. The current oscillates between 0 and 300 mA/cm^2, which indicates the electrode surface is activated and deactivated periodically. The change from the deactivated state (lowest current) to the activated state (highest current) is very slow. For instance, at 1.1 V it takes approximately 20 seconds to change the surface from the deactivated state to the activated state as seen in Fig. 3.2b. This is consistent with the above CV studies where the oscillations only appear at the very slow sweep rate. Fig. 3.2c also shows the effect of stirring on the current oscillations. A magnetic device was used for stirring. The magnetic

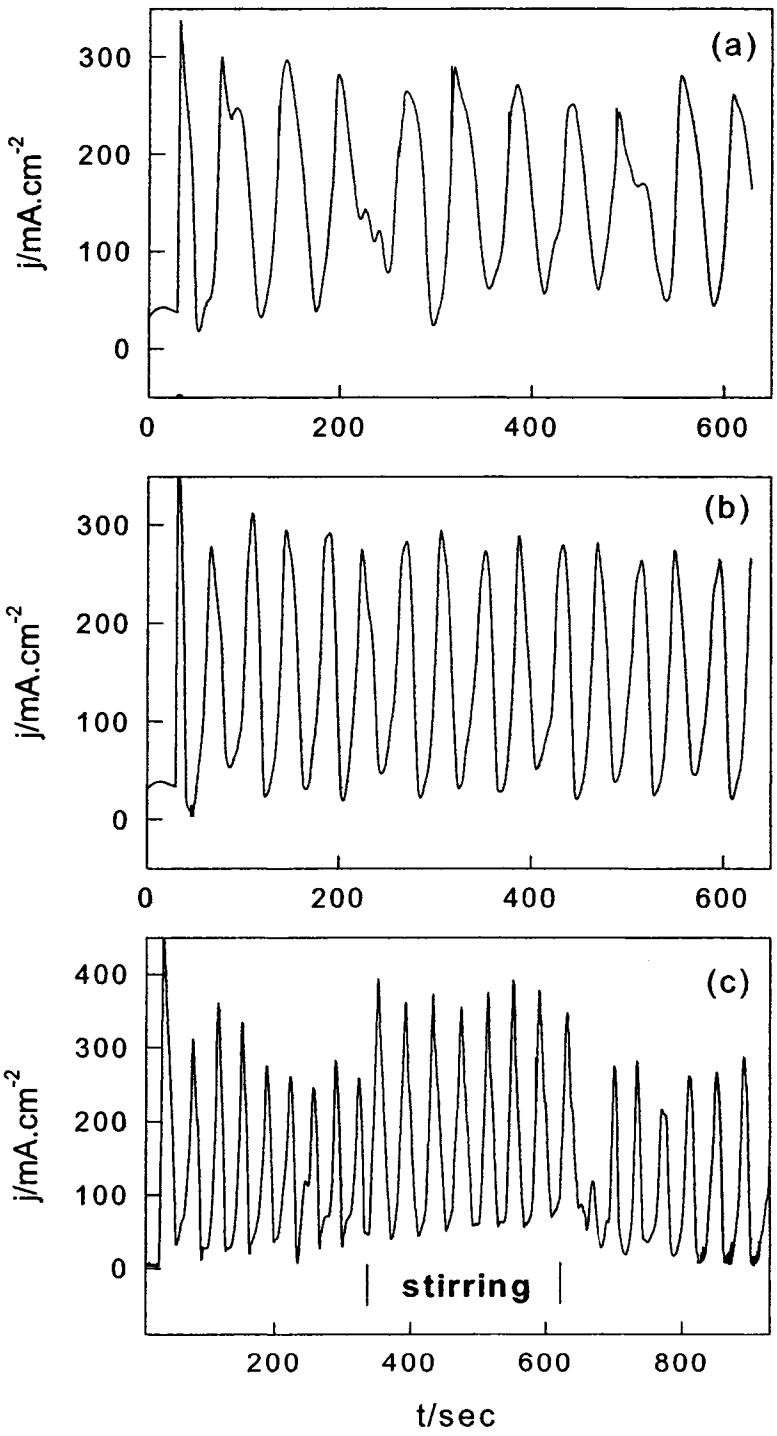

Figure 3.2. Chronoamperometric curves of 1.0 M Na_2S on a Pt electrode at: (a) 1000 mV; (b) 1100 mV; and (c) 1300 mV with stirring effect.

device was turned on at 350 seconds, and turned off at 630 seconds during the CA study as marked in Fig. 3.2c. The stirring enhances the amplitude of the oscillations. The current oscillates between 20 mA/cm^2 and 400 mA/cm^2 with the stirring. In contrast, the frequency of the oscillations decreases slightly. When the stirring is turned off, the oscillations quickly recover to their initial behavior. These results indicate that mass transport, through solution stirring, strongly affects the current oscillations. Now let us look at the behavior of sulfide oxidation under galvanostatic conditions.

3.2 Potential oscillations during the sulfide oxidation

3.2.1 Cyclic galvanic voltammetry

Fig. 3.3 presents cyclic galvanic voltammetric (CGV) curves at a current scan rate of 10 μA/s. As shown in Fig. 3.3a, when sweeping the current from 2 to 150 mA/cm^2, potential oscillations are observed at low current densities. Increasing the current from 20 to 80 mA/cm^2, the electrode potential only slightly increases ($\Delta E \approx 50$ mV). When further increasing the current to 114 mA/cm^2, the potential suddenly jumps to 2.0 V, then decreases while the current continues to increase, resulting in a peak centered at 116 mA/cm^2. Further increasing the current, the potential only slightly increases. In the reversing scan, potential oscillations are also observed and they disappear when the current decreases to 20 mA/cm^2. When further decreasing the current to 11 mA/cm^2, the potential suddenly falls from 1.3 V to 0.0 V. For discussion purposes, we refer the potential oscillations at the low potential range as Oscillation α and the potential oscillations occurring at the high potential range as Oscillation β. To determine whether the oscillations observed at the high current densities are related to the processes which occur on the electrode surface at the low current density another CGV was run

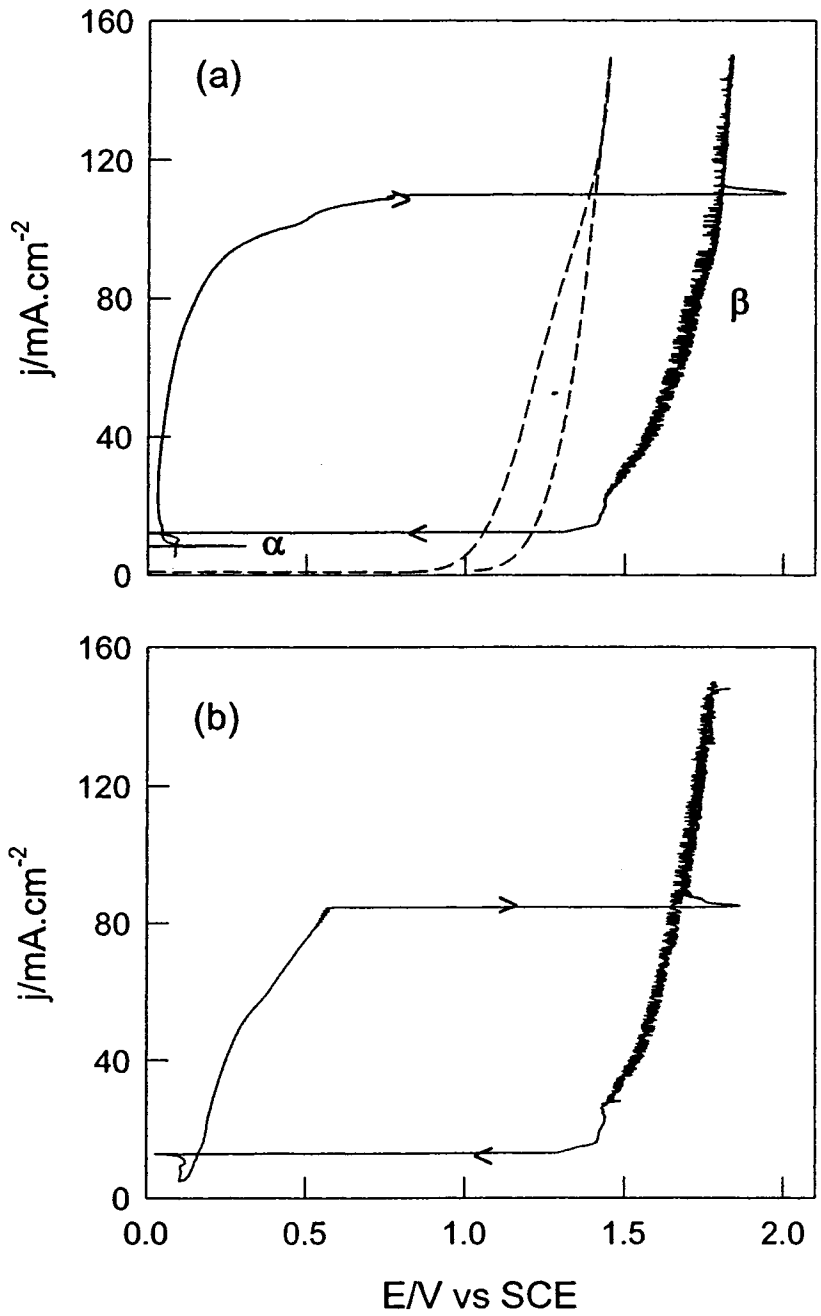

Figure 3.3. Cyclic galvanic voltammograms of 1.0 M Na_2S (solid line) and 1.0 M NaOH (dotted line) on a Pt electrode: (a) starting from the low current 2 mA; and (b) starting from the high current 150 mA. Galvanic scan rate: 10 μA/s.

starting with a fresh solution at a high current (150 mA/cm^2) as shown in Fig. 3.3b. This CGV curve is very similar to the CGV curve presented in Fig. 3.3a. The above results show that two distinct potential oscillations, plus well-defined bi-stability features, are observed in the CGV studies during the anodic oxidation of sulfide. The dashed line shown in Fig. 3.3a represents a CGV curve of Pt measured in 1 M NaOH solution: no oscillation and no bi-stability feature are observed. Chronopotentiometric technique was employed to further characterize the behavior of Oscillation α and Oscillation β during sulfide oxidation.

3.2.2 Chronopotentiometric study

Figure 3.4 presents four chronopotentiometric (CP) curves at: (a) 5 mA/cm^2, (b) 40 mA/cm^2, (c) 50 mA/cm^2, and (d) 100 mA/cm^2. In all cases the initial current density (j_1) was set at 0.0 mA/cm^2 for one minute. The current was then stepped to j_2 and held there for 15 minutes. No oscillation is observed at the low current 2 mA/cm^2, where the electrode potential is constant, at around –0.2 V/SCE. At j_2 = 5 mA/cm^2, the potential increases from –0.15 V to –0.08 V as seen in Fig. 4a, then jumps to 1.2 V and suddenly falls to 0.35 V; five large spikes with some small oscillations are observed during the first 8 minutes and then the potential decreases slowly. When the potential drops below 0.25 V, instead of the large spikes, oscillations with small amplitude but high frequency are observed. The inset to Fig. 3.4a shows a portion of the potential oscillations during the period between 570 second and 600 second. The amplitude of the oscillations is around 150 mV (between 0.1 V and 0.25 V), and the frequency of the oscillations is approximately 0.3 Hz. At j_2 = 20 mA/cm^2, except for the initial one large spike, no

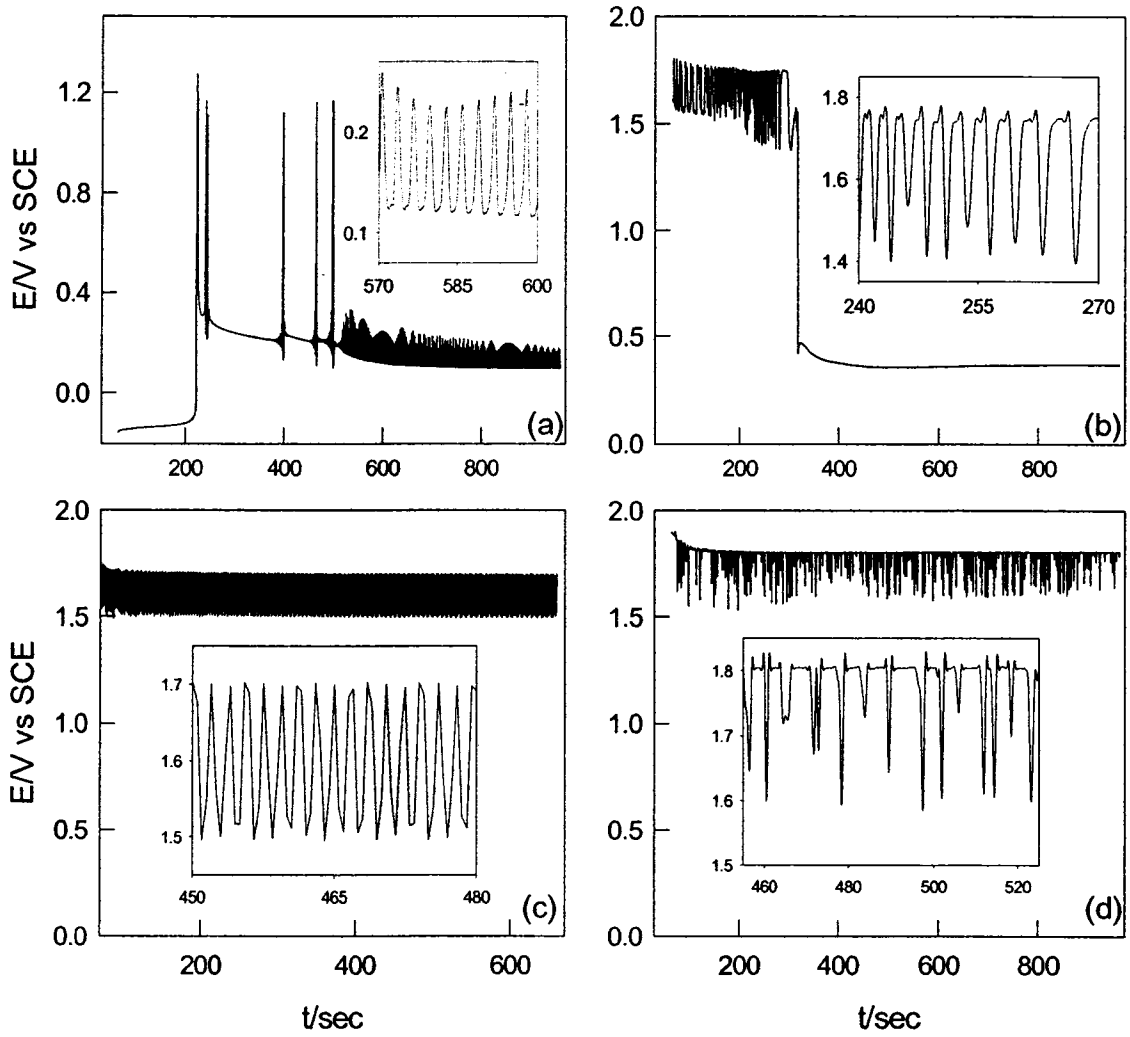

Figure 3.4. Chronopotentiometric curves of 1.0 M Na_2S on a Pt electrode at: (a) 5 $mA.cm^{-2}$; (b) 40 $mA.cm^{-2}$; (c) 50 $mA.cm^{-2}$; and (d) 100 $mA.cm^{-2}$. The insets present a portion of the corresponding CP curves.

oscillation is observed, when the electrode potential is above 0.25 V. When further increasing the current to 40 mA/cm^2 (Fig. 3.4b), the potential jumps to 1.75 V and oscillations with small amplitude and high frequency are observed; after five minutes, the potential falls down to 0.4 V and the oscillations disappear immediately. The inset to Fig. 3.4b presents a portion of the potential oscillations during the period between 240 second and 270 second. The frequency of the oscillation is similar to that observed in Fig. 3.4a; however, the amplitude is over two times larger (approximately 400 mV) and at much higher potential (between 1.4 V and 1.75 V). Further increasing the current to 50 mA/cm^2, potential oscillations with high frequency are observed during the entire electrolysis (Fig. 3.4c). The inset to Fig. 3.4c displays a portion of the potential oscillations in the period between 450 second and 480 second, showing that the potential oscillation range is between 1.5 V and 1.7 V. As seen in Fig. 3.4d, when increasing the current to 100 mA/cm^2 the potential oscillations occur at a higher potential range between 1.6 V and 1.85 V and the potential oscillations become non-periodic. While at the current j_2 = 160 mA/cm^2, the electrode potential is above 1.8 V and no oscillation is observed. All these results indicate that both Oscillation α and Oscillation β strongly depend on the applied current. Oscillation α occurs at the low current densities, where the potential oscillation range is located between 0 and 0.3 V. In contrast, Oscillation β takes place at the high current, where the potential range is between 1.4 V and 1.8 V. Electrochemical impedance spectroscopy (EIS) is a powerful technique in classifying unknown electrochemical oscillators [21-22]. Thus, we investigated further using EIS to decipher the nature of Oscillation α and Oscillation β.

3.3 Electrochemical impedance study

Figure 3.5 presents Nyquist plots recorded in 1.0 M Na_2S at the electrode potential: (a) -150 mV, (b) +100 mV, (c) 400 mV and (d) 1450 mV, where Z_r and Z_i are the real and imaginary components of the impedance, respectively. The frequency used in this study was varied from 40 kHz to 25 mHz. The behavior of the impedance plots at +100 mV is totally different from the Nyquist plots recorded at −150 mV and +400 mV. Only positive faradic impedance is observed at -150 mV and 400 mV. In contrast, negative real impedance appears at the potential +100 mV. This is very consistent with the above galvanostatic studies. No potential oscillation is observed at 2 mA/cm^2 and 20 mA/cm^2, where the electrode potential is below −0.15 V or above 0.25 V. On the contrary, potential oscillations are observed at 5 mA/cm^2 when the potential locates between 0 and 0.25 V (Fig. 3.4a). Further increasing the potential, negative faradic impedance is also observed at 1.45 V (Fig. 3.4d) and only positive faradic impedance is observed at 1.35 V and 1.85 V. This is very consistent with Oscillation β, whose amplitude is in the potential range between 1.4 V and 1.85 V. For instance, when the potential falls from 1.5 V to 0.4 V, the potential oscillations vanish immediately (Fig. 3.4b). All these results clearly show the presence of a hidden negative differential resistance (HNDR) (i.e., negative differential resistances in a region of intermediate frequencies and positive differential resistances in low frequencies) in both Oscillation α and Oscillation β.

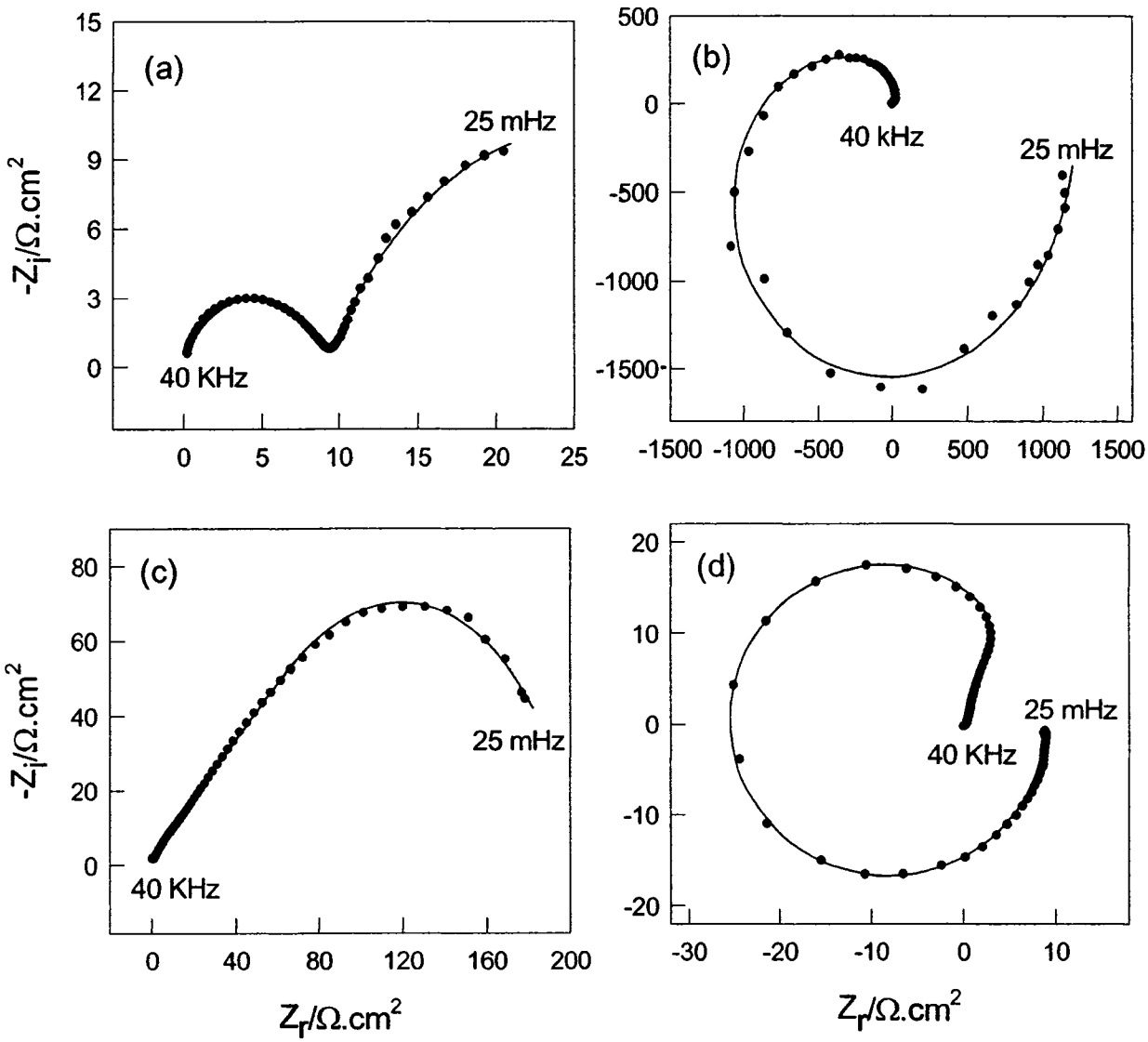

Figure 3.5. EIS complex plane plots of 1.0 M Na_2S with electrode potential measured vs SCE at: (a) −150 mV; (b) 100 mV; (c) 400 mV; and (d) 1450 mV. Experimental data: •. Fitting curve: sold line.

Equivalent electric circuits were also used to fit the experimental impedance spectra. The equivalent circuit shown in Fig. 3.6a was used to fit the EIS data presented in Fig. 3.5a and 3.5c [65], where only positive faradic impedance was observed. The other equivalent circuit shown in Fig. 3.6b was employed to fit the hidden negative impedance spectra presented in Fig. 3.5b and 3.5d [66]. All the fitting curves are shown as solid lines together with the experimental data denoted as symbols in Fig. 3.5. The excellent fits to the impedance spectra at all four potentials demonstrate the utility of the two equivalent circuits. In both circuits, the R_s represents the uncompensated solution resistance. In Circuit *a*, the parallel combination of a charge transfer resistance (R_{ct}) and a constant phase element (CPE_{dl}) takes into account the sulfide oxidation, while the parallel combination (R_1CPE_1) is associated with the properties of specific adsorbed species on the electrode surface at the investigated electrode potential. A CPE is defined by CPE-T and CPE-P. If CPE-P equals 1, then the CPE is identical to a capacitor C_{dl}. The parallel combination (RCPE) leads to a depressed semi-circle in the corresponding Nyquist impedance plot. In Circuit *b*, the parallel combination of a charge transfer resistance (R_{ct}) and a capacitor (C_{dl}) takes into account the sulfide oxidation. Another branch consists of a parallel combination of a capacitor (C_1) and a resistor (R_1), where R_1 is in series with a parallel combination of a resistor (R_2) and a capacitor (C_2). This branch is associated with specific adsorbed species and sulfur deposits formed on the electrode surface to account for the negative faradic impedance. The values for the parameters determined by the fitting of the experimental EIS data (Fig. 3.5a & 3.5c) using Circuit *a* are summarized in Table 3.1. The fitting results of Fig. 3.5b and 3.5d using Circuit *b* are summarized in

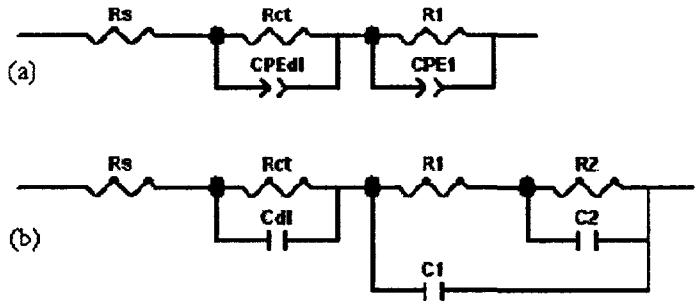

Figure 3.6. Equivalent circuits used to model the EIS data for (a) positive faradaic impedance and (b) negative faradaic impedance.

TABLE 3.1: Impedance Components for Positive Faradaic Impedance on a Platinum Electrode by Fitting the Experimental Data Measured in 1.0 M Na_2S Using the Equivalent Circuit Shown in Figure 3.6a.

Potential (mV)	R_1 ($\Omega.cm^2$)	CPE_1-T ($mF.cm^{-2}$)	CPE_1-P	R_{ct} ($\Omega.cm^2$)	CPE_{dl}-T ($mF.cm^{-2}$)	CPE_{dl}-P
-150	33.62	121.8	0.7	9.421	0.195	0.72
400	117.2	0.514	0.51	87.01	1.05	0.98

TABLE 3.2: Impedance Components for Negative Faradaic Impedance on a Platinum Electrode by Fitting the Experimental Data Measured in 1.0 M Na_2S Using the Equivalent Circuit Shown in Figure 3.6b.

Potential (mV)	R_1 ($\Omega.cm^2$)	C_1 ($mF.cm^{-2}$)	R_{ct} ($\Omega.cm^2$)	C_{dl} ($mF.cm^{-2}$)	R_2 ($\Omega.cm^2$)	C_2 ($mF.cm^{-2}$)
100	-400	-0.24	26.74	0.069	1600	0.17
1450	-31	-0.052	6.8	0.041	32.5	0.051

Table 3.2. All the associated errors are within 6 %, indicating that the proposed models shown in Figure 6 can fit the experimental EIS data presented in Fig. 3.5 effectively. R_{ct} is the charge-transfer resistance, and the inverse charge-transfer resistance R_{ct}^{-1} describes how fast the rate of charge transfer changes with a change in electrode potential, i.e., the potential dependence of the rate constants for charge transfer [65-66]. As shown in Table 3.1 & 3.2, the R_{ct} value increases as:

$$R_{ct}\,(1450\text{ mV}) < R_{ct}\,(-150\text{ mV}) < R_{ct}\,(100\text{ mV}) < R_{ct}\,(400\text{ mV}).$$

This is consistent with the observation in the CV studies shown in Fig. 3.1. It is expected that R_{ct} has the lowest value at 1.45 V as both sulfide oxidation and oxygen evolution are expected at the potential 1.45 V vs SCE. As shown in Fig. 3.1a & 3.1b, a current peak is seen at around -150 mV, and the current change with the change of potential at 400 mV is very small. The CPE_{dl}-P value at 400 mV is very close to 1, which indicates the CPE_{dl} in Circuit *a* can be replaced with a capacitor when it is used to fit the EIS data measured at 400 mV. As shown in Table 3.2, at 100 mV and 1450 mV, both R_1 and C_1 are negative, which is consistent with oscillations occurring in the above two potential ranges during the electrooxidation of sulfide. The large value of the R_2 at 100 mV indicates that sulfur deposits are formed on the electrode surface since the conductivity of a sulfur layer is very low. All these EIS results are consistent with the above CGV and CP studies. Both Oscillation α and Oscillation β can thus be classified as HNDR oscillators.

3.4. Discussion

The mechanisms for the electrochemical oxidation of sulfide are complicated since sulfur has a number of different oxidation states such as -2, 0, +4 and +6. Anodic oxidation of sulfide can produce elemental sulfur, polysulfides (S_x^{2-}) or sulfur oxyanions depending

on the potential, pH and temperature of the electrolyte. In what follows, we aim: (i) to describe how the electrode surface states influence nonlinear kinetics, and (ii) to explain the occurrences of oscillations and the bistability during sulfide oxidation on a Pt electrode.

3.4.1. Mechanistic consideration for Oscillation α, Oscillation β and the bistability

Although the above EIS study shows that both potential Oscillation α and Oscillation β occurring under galvanostatic conditions can be classified as HNDR oscillators, there is a significant difference between Oscillation α and Oscillation β. As shown in Fig. 3a, the onset potential for oxygen evolution on the Pt electrode surface in a 1 M NaOH solution (dashed line) is around 0.8 V. Oxide growth and oxygen evolution on noble metals have been studied extensively and the reaction mechanism has been proposed as [30,67]:

$$Pt + OH^- \rightarrow Pt\text{-}OH + e^- \quad (3.1)$$

$$Pt\text{-}OH + OH^- \rightarrow Pt\text{-}O + H_2O + e^- \quad (3.2)$$

$$2\ Pt\text{-}O \rightarrow 2\ Pt + O_2 \quad (3.3)$$

An electrochemical FTIR study by Sun and Chen has also shown that the formation of platinum oxide (Pt-O) occurs at potentials higher than 0.55 V vs SCE in a 0.05 M NaOH solution [68]. Oscillation α occurs at low current densities (below 10 mA/cm^2), where the electrode potential is between 0 and 0.3 V. It should be recognized that there is no oxide formation at such a low potential range. On the other hand, the adsorption of sulfide on a Pt surface is much stronger than that of hydroxide, and sulfur adsorption on the Pt surface even occurs at very low electrode potential (~ −1.4 V):

$$Pt + S^{2-} \rightarrow PtS + 2\ e^- \quad (3.4)$$

$$Pt + HS^- + OH^- \rightarrow PtS + H_2O + 2\ e^- \quad (3.5)$$

This is consistent with the fact that there is no hydrogen adsorption/desorption peak seen in the CV curves of Fig. 3.1. The pH of the 1.0 M Na_2S electrolyte used in this study is close to the pH value of the 1.0 M NaOH solution, which indicates that HS^- ions are the predominant species. It is well known that hydrosulfide can be oxidized to sulfur and polysulfides. Sulfide and polysulfides can also be oxidized to form sulfur. Based on our CP study, the electrode potential is almost constant, staying at around –0.2 V during the 15 minute electrolysis at 2 mA/cm^2. This indicates that there is no sulfur build-up on the electrode surface at the applied low current. As the conductivity of the sulfur layer is very low, if there was a sulfur layer build-up, the electrode potential would go up in order to satisfy the applied constant current. The small impedance observed in Fig. 3.5a further supports the absence of sulfur build-up on the electrode surface at –0.15 V. It is known that the sulfur deposits can be removed from the Pt surface by the formation of polysulfides:

$$PtS + HS^- + OH^- \rightarrow Pt + S_2^{2-} + H_2O \qquad (3.6)$$

$$PtS + S_2^{2-} \rightarrow Pt + S_3^{2-} \qquad (3.7)$$

Thus, even if there were sulfur formation on the electrode surface, it would not be seen if the dissolution of sulfur was equal to or faster than its formation. In contrast, at 5 mA/cm^2 (Fig. 4a), the potential slowly increases from –150 mV to –80 mV during the first 200 seconds, and then jumps to over +1000 mV. This potential jump indicates that there was a build-up of sulfur deposits. Further evidence showing the formation of sulfur deposits is the large negative faradic impedance observed in Fig. 3.5b. When strongly bonded sulfur forms, surface sites are blocked and the potential must increase so that the rates of reactions increase at the remaining vacant sites to satisfy the applied constant current. As

shown in the inset to Fig. 3.4a, the potential oscillations are in the range between 0.1 V and 0.3 V. At the bottom part of the oscillations, the sulfur formation (Reaction 3.4 & 3.5) is faster than the sulfur dissolution (Reaction 3.6 & 3.7), resulting in sulfur build-up, thus the electrode potential goes up. When the potential reaches the top part of the oscillations, sulfide can be directly oxidized to form polysulfide (S_2^{2-}) at around 0.23 V [41]:

$$2\,S^{2-} \rightarrow S_2^{2-} + 2\,e^- \qquad (3.8)$$

The effects of Reaction 3.8 are two-fold: (i) the sulfur formation becomes less as the applied current is constant and partial current is used for Reaction 8; and (ii) the product (S_2^{2-}) of Reaction 3.8 also increases Reaction 3.7. Thus, the oxidation of S^{2-} to S_2^{2-} results in sulfur removal from the electrode surface. As a result, the electrode potential drops down Reaction 3.8 switches off, and sulfur deposits are formed on the electrode surface again. Therefore, the deposition of sulfur on the Pt surface alternating with its removal by forming soluble polysulfides are the main reasons for Oscillation α.

Oscillation β appears at higher current densities with the electrode potential between 1.4 V and 1.8 V. At such a high potential range, platinum oxides (PtO_x) are formed and oxygen evolution also occurs on the Pt surface. As seen in Fig. 3.3, there are well-defined bistability features in the presence of sodium sulfide; however, we did not observe any oscillations or a bistability feature in the *j-E* curve in the NaOH solution. The appearance of the bistability feature is an indicator of the change of the electrode surface states. At the low potential region, sulfide is oxidized on a platinum surface, while at the high potential region platinum oxide forms and sulfide is oxidized on the platinum oxide surface. The appearance of the bistability features indicates that the electrochemical activities of the Pt surface and the platinum oxide surface towards sulfide oxidation are

different. As seen in Fig. 3.4c, periodic potential oscillations are observed at 50 mA/cm^2. At the bottom portion of the oscillations, the predominant reaction is sulfide oxidation to sulfur. Indeed, we did observe sulfur deposits formed on the electrode surface. Bue to the build up of sulfur, the electrode potential increases. It can be seen in Fig. 3.1a that oxygen evolution strongly depends on the applied potential. Thus, at the top part of the oscillations, oxygen evolution becomes the predominant reaction where we observe more gas evolution, i.e., much less sulfur is produced at the top part of the oscillations than that at the bottom of the oscillations as the applied current is constant. Therefore, more HS^- /S^{2-} are used for sulfur dissolution (Reaction 3.6 & 3.7) at the top part of the oscillation than at the bottom of the oscillation. Also, oxygen evolution increases mass transport, and, more HS^-/S^{2-} are available for sulfur dissolution (Reaction 3.6 & 3.7). Actually, we observed partial removal of sulfur deposits periodically from the electrode surface during the experiments. Thus, Oscillation β is caused by the synergic effect of sulfur formation/removal and oxygen evolution at the high potential range.

3.4.2. Mechanistic consideration of the current oscillations

As shown in Fig.3.1, the current oscillations strongly depend on the potential sweep rates. They appear in the CV curves recorded in 1.0 M Na_2S at 1 mV/s (Fig. 3.1c), but they do not show up at the sweep rates of 20 mV/s (Fig. 3.1a) and 5 mV/s (Fig. 3.1b), which indicates that the current oscillations occur on a relatively slow time scale. The sulfide concentrations also play a key role in the current oscillations. No current oscillation is observed in 0.65 M Na_2S (the inset to Fig. 3.1c); in contrast, significant current oscillations are seen in Fig. 3.1c (1.0 M Na_2S) and in Fig. 3.1d (2.0 M Na_2S). The current oscillations are located in the large peak during anodic oxidation of sulfide as shown in

the CV curves (Fig.3.1). Several reactions may occur in the potential range of the large peak: (1) HS^-/S^{2-} may be oxidized to form sulfur and polysulfides as we discussed in Section 3.4.1; (2) the increase of the current with the increment of the potential on the climbing portion of the peak (positive slope of the j – E profile) indicates the occurrence of hydroxide adsorption comparing the CV curves recorded in 1 M Na_2S and 1 M NaOH (Fig. 3.1a); (3) the adsorbed hydroxide radicals may react with sulfide or hydrosulfide to form sulfate [43,51]; (4) the decrease of the current with the increment of potential on the declining portion of the peak (negative slope of the j – E feature) may result from platinum oxide ($Pt\text{-}O_x$) formation which inhibits sulfide oxidation; and (5) sulfide species can also reduce the formed platinum oxide. As shown in Fig. 3.2, the amplitude of the current oscillations is very large (~ 300 mA/cm^2), which indicates that the electrochemical activity of the electrode is much higher at the top part of the oscillations than that at the bottom portion of the oscillations. The lower activity of the electrode surface at the bottom of the oscillations is likely due to the formation of sulfur deposits and platinum oxide. Indeed, we did observe a sulfur coating on the electrode surface during the CV and CA studies. At the bottom of the oscillation, a large amount of HS^-/S^{2-} and OH^- is available for sulfur dissolution (Reaction 3.6) to form polysulfide (S_2^{2-}). The formation of S_2^{2-} further catalyzes the dissolution of sulfur deposits (Reaction 3.7). On the other hand, the formed platinum oxide can be reduced by sulfide and this also frees Pt sites:

$$PtO_x + 2x\ HS^- \rightarrow Pt + 2\ S + x\ H_2O \qquad (3.9)$$

More Pt sites are available for sulfide oxidation, thus increasing the current. When the current reaches the top portion of the oscillation, because of the very large current (~300

mA/cm^2), it is expected that most sulfide species available in the double-layer region are consumed by the oxidation reactions. Sulfur deposits and platinum oxide may be formed; hence, the activity of the surface decreases and the current decreases. This is consistent with the effects of high sulfide concentration (Fig. 3.1) and stirring (Fig. 3.2c). In summary, the above results indicate that the current oscillations results from the formation of platinum oxide (by the oxidation of hydroxide) and sulfur deposits (by the oxidation of HS^-/S^{2-}) followed by the subsequent removal of the platinum oxide (by the reduction of sulfide) and sulfur deposits (by forming polysulfides).

3.5. Summary

The electrooxidation of sulfide on a Pt electrode has been investigated through a number of electrochemical methods such as cyclic voltammetry, cyclic/linear galvanic voltammetry, galvanostatic/potentostatic techniques and electrochemical impedance spectroscopy. Sulfide and hydrosulfide are oxidized to sulfur, polysulfides and sulfate depending upon the electrode potential. Three distinct electrochemical oscillations as well as a bistability feature are observed during the anodic oxidation of sulfide. Two peaks are observed in the CV curve when scanning the potential from –0.8 to +1.8 V. The small one is located in the potential range between –0.5 and 0.0 V, while the large peak locates in between 0.6 and 1.4 V. The current oscillations with very large amplitude and small frequency are located in large peak potential range. The current oscillations strongly depend on the potential sweep rate and the concentration of sulfide. The current oscillations are likely caused by the periodic formation of platinum oxide (via oxidation of hydroxide) and sulfur deposits (via oxidation of HS^-/S^{2-}) and by removal of the platinum oxide (via reduction of sulfide) and sulfur deposits (by forming polysulfides).

Oscillation α and Oscillation β are galvanostatic potential oscillations. Our EIS studies show that both Oscillation α and Oscillation β can be classified as HNDR oscillators. Oscillation α occurs at low current densities (below 10 mA/cm^2), where the electrode potential is between 0 and 0.3 V. The formation of sulfur on the Pt surface and the removal of sulfur from the Pt surface through forming soluble polysulfides, switching the direct oxidation of S^{2-}/HS^- to polysulfides (Reaction 3.8) off and on, are the main reasons for Oscillation α. Oscillation β appears at high current densities, with an electrode potential between 1.4 V and 1.8 V. Oxygen evolution occurs at this high potential range and platinum oxides (PtO_x) are also formed on the Pt electrode surface. Oscillation β is due to the synergic effect of sulfur formation/removal and oxygen evolution at the high potential range. Our EIS studies show that both Oscillation α and Oscillation β can be classified as HNDR oscillators. The well-defined bistability feature is due to the change of the electrode surface states: in the low potential region, sulfide is oxidized on a platinum surface, while in the high potential region platinum oxides are formed and sulfide is oxidized on a platinum oxide surface.

Chapter 4

Potential Oscillations during the Electrocatalytic Oxidation of Sulfide on a Microstructured Ti/Ta_2O_5-IrO_2 Electrode

4.1 Microstructure of the Coatings

The surface morphology of the IrO_2-Ta_2O_5 oxide coatings was examined by scanning electron microscopy (SEM). As shown in Figure 4.1a, the oxide coatings exhibit a typical porous 'cracked mud' structure. This is consistent with the observation by Comninellis et al [35]. Sitting on the 'cracked mud' are some oxide particles. Figure 4.1b shows that the size of the particles is between 100 and 150 nm. The above images indicate that the IrO_2-Ta_2O_5 oxide electrode prepared in this study has a much larger surface area than a planar metal electrode surface such as Pt and Au. A large electrode surface area is desirable for most industrial electrochemical processes. EDX analysis of the oxide coating shows a higher iridium content in the oxide particles than that in the 'cracked mud' region.

4.2 Cyclic Voltammetry and Differential Capacity

Figure 4.2a shows two cyclic voltammograms (CVs) recorded in 0.65 M Na_2S (solid line) and 0.65 M NaOH (dotted line) solutions. The pH of the sulfide solution is close to that of the 0.65 M hydroxide solution, and thus HS^- ions are presumed to be the major sulfide species. As seen by the CV curve in the sodium hydroxide solution, oxygen evolution occurs at around 0.5 V/SCE and, by further increasing electrode potential, the current of the oxygen evolution linearly increases. All these results indicate that the Ti/Ta_2O_5-IrO_2 electrode possesses high electrocatalytic activity for oxygen

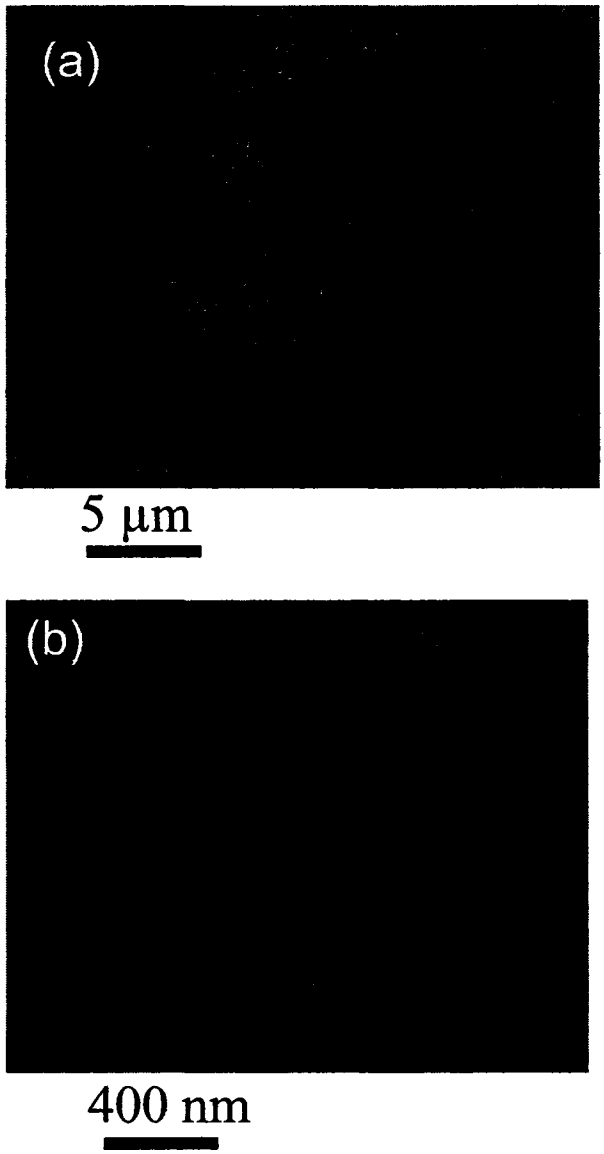

Fig. 4.1. Scanning electron micrographs of Ta and Ir oxide based electrodes (Ti/Ta_2O_5-IrO_2) (a) Magnification: x 3,000; (b) Magnification: x 35,000

evolution. In the presence of sulfide (solid line), sweeping potential from -0.8 V to 1.0 V/SCE yielded a broad hump starting at -0.62 V/SCE in the CV, followed by a large and wide peak centred at ~0.1 V/SCE. The broad hump may be due to sulfide adsorption and/or polysulfide formation. The large (irreversible) peak may correspond to sulfide oxidation [41, 43]. When scanning back from 1.0 to -0.8 V/SCE, three peaks at approximately 0.9, 0.2 and 0.05 V are observed in the CV curves. The multiple-peaks shown in the CV curves indicate that a number of different oxidation state sulfur compounds could be formed during the electro-oxidation of sulfide. Figure 4.2b shows two differential capacity (DC) curves determined from the AC impedance measurements using 0.65 M Na_2S (solid line) and 0.65 M NaOH (dotted line) solutions. The shape of these two DC curves is consistent with the forward scan of the CV curves shown in Fig. 4.1a, which indicates that both cyclic voltammetry and differential capacity can be used to characterize the electrode surface and the electro-oxidation of sulfide. The capacitance of this Ti/Ta_2O_5-IrO_2 electrode is 215 $\mu F\ cm^{-2}$ at the electrode potential -0.75 V/SCE (Fig. 4.2b); in contrast, the capacitance of Pt is 4.78 $\mu F\ cm^{-2}$ at the same potential, which indicates that the Ti/Ta_2O_5-IrO_2 electrode has much larger real surface area than regular metal electrodes such as Pt due to the porous structure of the oxide coating as observed in the SEM images.

4.3 Galvanostatic Potential Oscillations during the Anodic Oxidation of Sulfide

Figure 4.3 shows a linear galvanic voltammetric curve recorded in the 0.65 M Na_2S solution from 5 mA to 150 mA at a current scan rate of 20 μA/s. Two different regions of potential oscillation are observed in the galvanic curve, named here as Oscillation A and

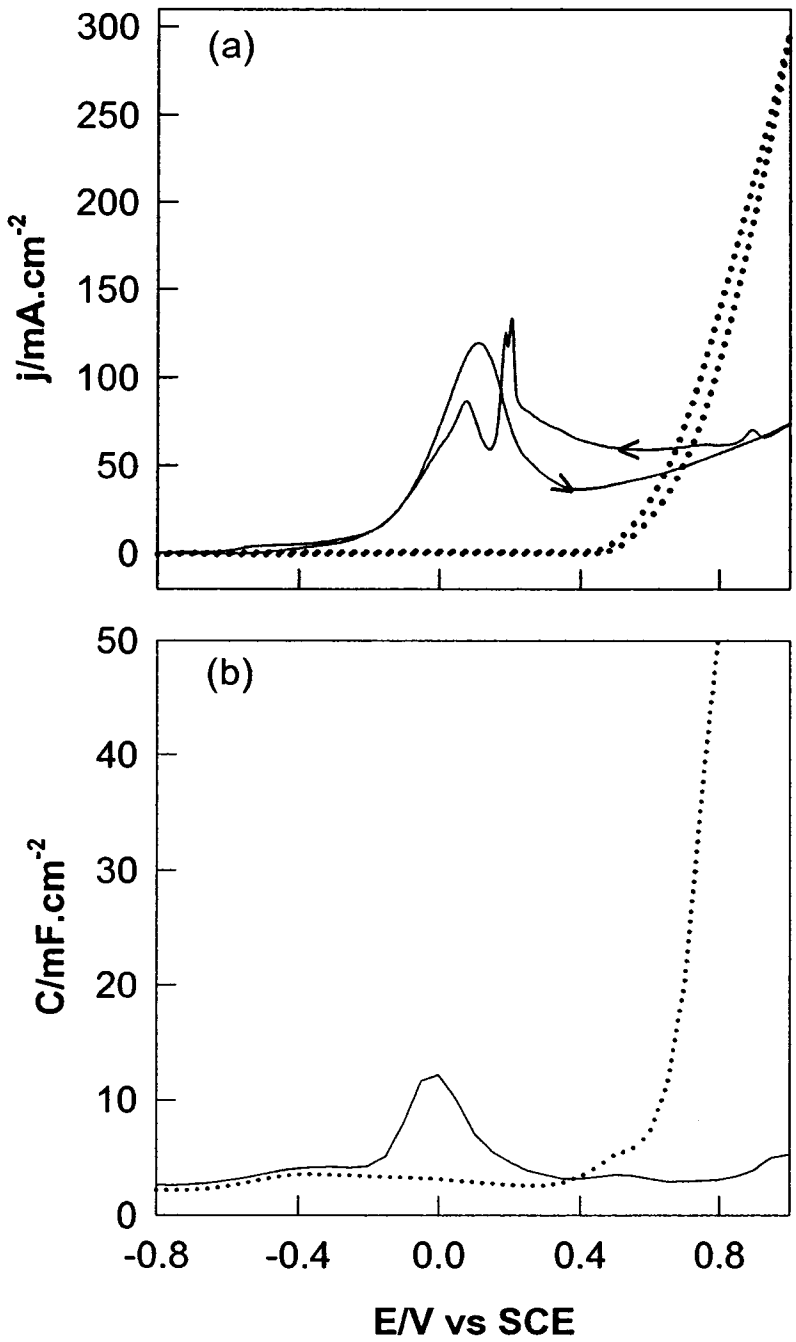

Fig. 4.2. (a) Cyclic voltammograms of 0.65 M Na_2S (solid line) and 0.65 M NaOH (dotted line) at a potential sweep rate of 20 mV/s; and (b) differential capacitance plots of 0.65 M Na_2S (solid line) and 0.65 M NaOH (dotted line).

Oscillation B, respectively. The amplitude of Oscillation A is significantly larger than that of Oscillation B. In contrast, the frequency of Oscillation A is much smaller than that of Oscillation B.

Figure 4.4 shows Oscillation A under galvanostatic conditions. In each galvanostatic experiment, the initial current density (j_1) was set at 0 mA/cm^2 for one minute. The current was then increased and held at j_2 for 15 minutes. At the low current density j_2 = 20 mA/cm^2 the potential increases slowly from -0.115 V and then stays constant at around -0.1 V. In contrast, periodic potential oscillations are observed when j_2 is increased to 25, 30 and 35 mA/cm^2. The amplitude of these oscillations is very large, ranging between -0.1 and +1.4 V/SCE, and similar for the three different current densities. Initially, the potential increases slowly from -0.1 V to 0.0 V. Then, after suddenly jumping to + 1.4 V, it slowly down to -0.1 V. The time to increase the potential from -0.1V to 0.0 V decreases when increasing j_2 from 25 to 35 mA/cm^2; thus, the frequency of the oscillations increases. On the other hand, there is a shoulder present at around 1.0 V when the potential drops from 1.4 V to -0.1 V. This shoulder becomes more and more definitive with increasing current density. At 40 mA/cm^2, the shoulder becomes a platform and dominates the E – t curve with the presence of some small oscillations and two large oscillations. When further increasing j_2 to 45 mA/cm^2, all oscillations disappear, and the electrode potential is slightly higher than +1.0 V. All these results show that the potential oscillations strongly depend on the applied current density. Figure 4.5 presents four galvanostatic curves in the Oscillation B region. The high frequency oscillations observed at 60 mA/cm^2 range between 1.15 and 1.4 V/SCE. Increasing

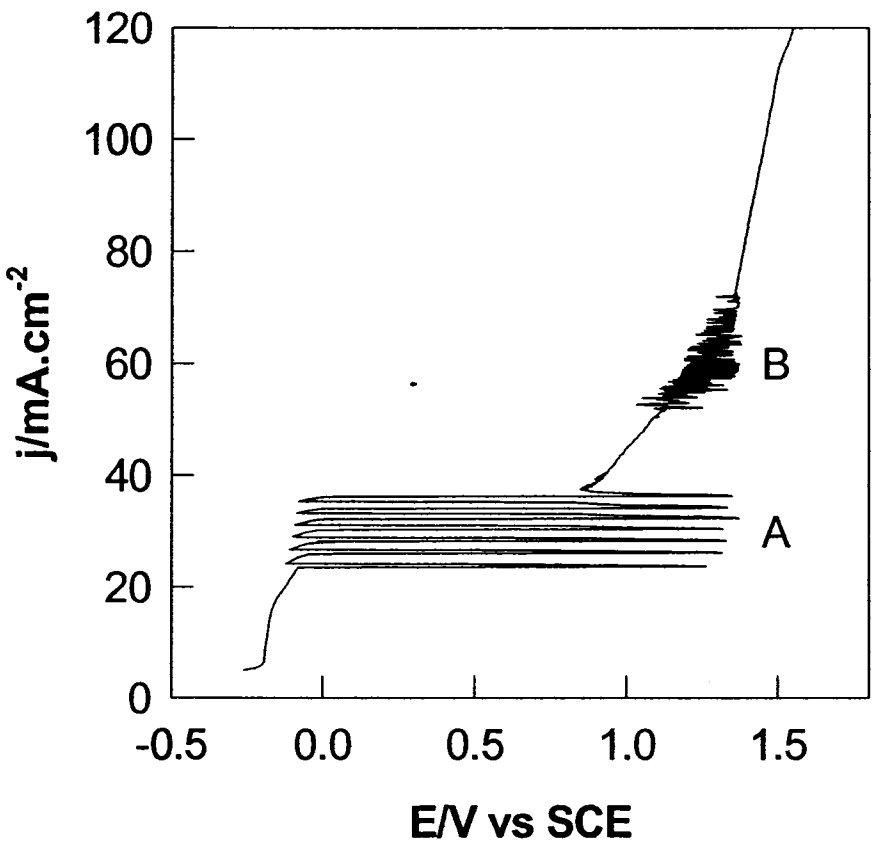

Fig. 4.3. Linear galvanic voltammogram of 0.65 M Na_2S on the Ti/Ta_2O_5-IrO_2 electrode.

Galvanic scan rate: 20 μA/s

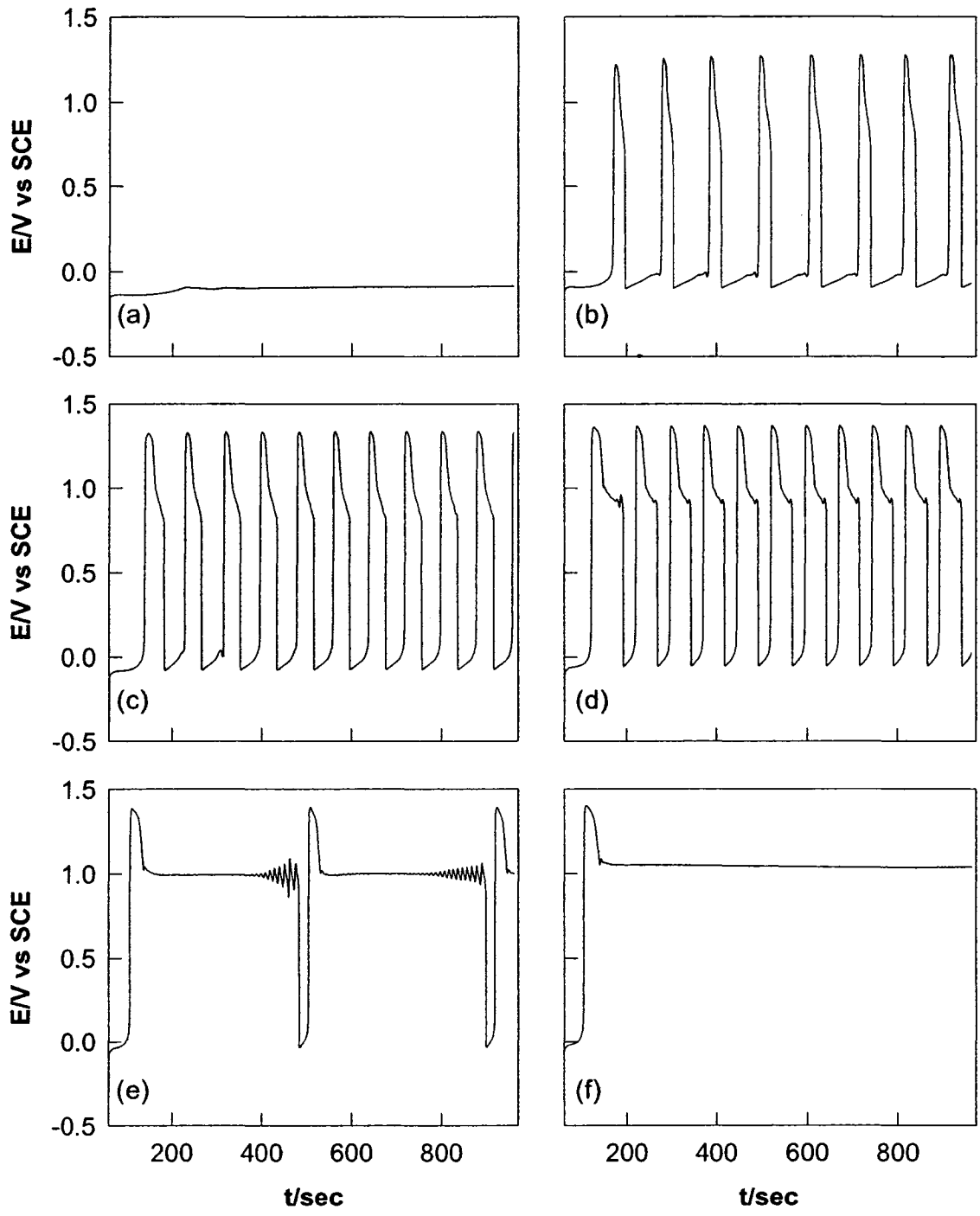

Fig. 4.4. Chronopotentiometric curves of 0.65 M Na_2S: (a) 20 $mA.cm^{-2}$; (b) 25 $mA.cm^{-2}$; (c) 30 $mA.cm^{-2}$; (d) 35 $mA.cm^{-2}$; (e) 40 $mA.cm^{-2}$; and (f) 45 $mA.cm^{-2}$

the current density j_2, the upper boundary of the oscillations remains constant, but the lower boundary of the oscillations shifts to higher potentials. As a result, the amplitude of the oscillation becomes smaller and smaller. The oscillation vanishes at $j_2 = 75$ mA/cm^2, where the potential stays slightly above 1.4 V. As shown in Fig. 4.2, there is no oscillation present in the CV curve, and we did not observe any potentiostatic current oscillations in our investigated potential range from -0.8 V to 1.8 V, which is different from the behavior observed during the anodic oxidation of sulfide on the Pt electrode [49]. In order to understand the nature of the galvanostatic potential oscillations, we did further studies on sulfide oxidation using electrochemical impedance spectroscopy.

4.4. Electrochemical Impedance Study

Figure 4.6 presents six Nyquist plots at different electrode potentials, where Z_r and $-Z_i$ are the real and imaginary components of the impedance, respectively. The frequency was changed from 25 kHz to 25 mHz as indicated in the plots. The potential chosen in the EIS study was determined from the galvanostatic results. The behavior of the impedance plot at -0.05 V is totally different from the Nyquist plot recorded at -0.1 V; negative impedance appears at the potential -0.05 V. This is consistent with the galvanostatic study where no potential oscillation were observed at 20 mA/cm^2 when the electrode potential is -0.1 V; and potential oscillations occurred at 25 mA/cm^2 where the electrode potential is above -0.1 V. With increasing potential, negative faradic impedance is also observed at 0.5 and 1.2 V. Those two potentials lie in the range of the potential oscillations. All these results clearly

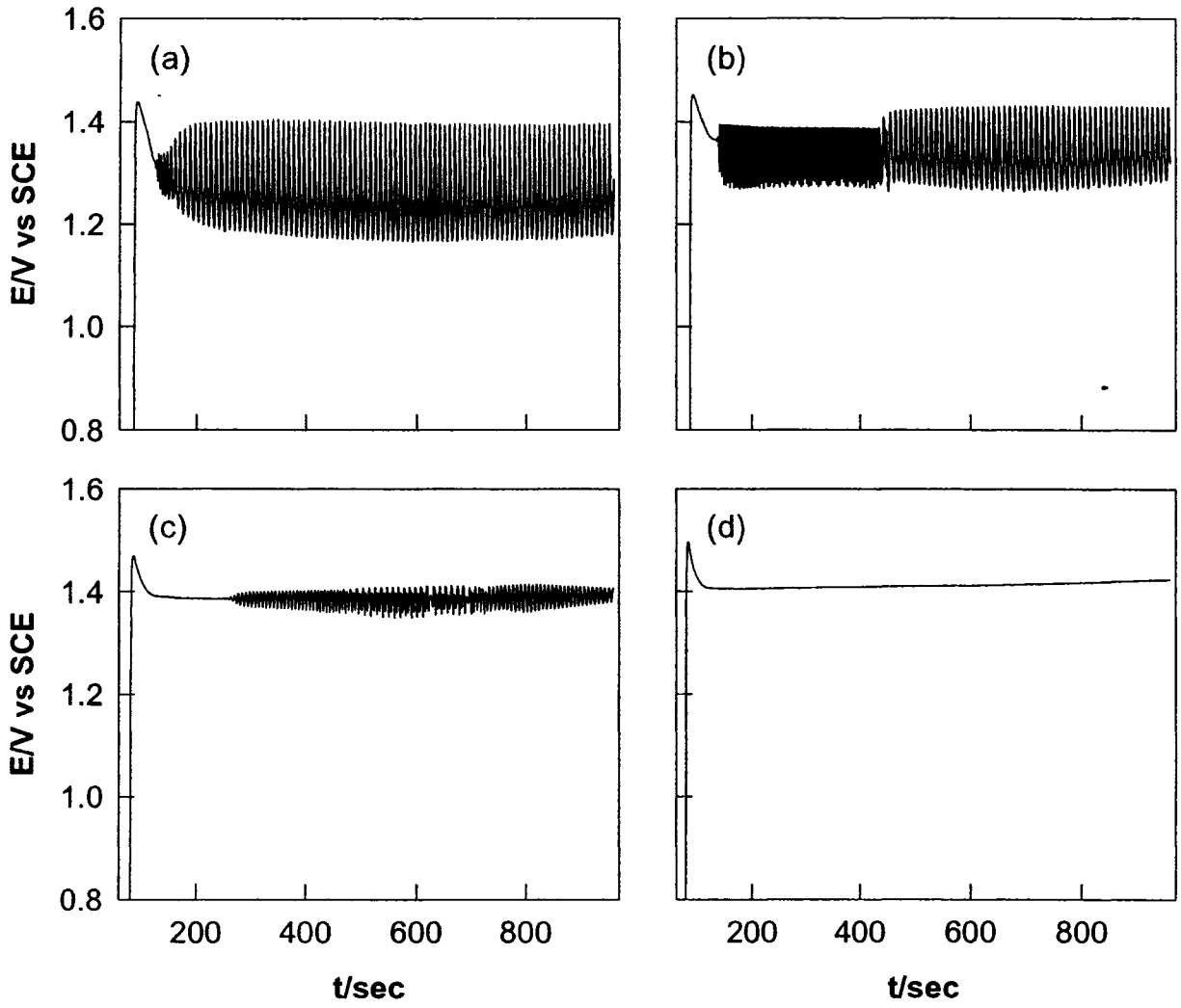

Fig. 4.5. Chronopotentiometric curves of 0.65 M Na_2S: (a) 60 mA.cm^{-2}; (b) 65 mA.cm^{-2}; (c) 70 mA.cm^{-2}; and (d) 75 mA.cm^{-2}

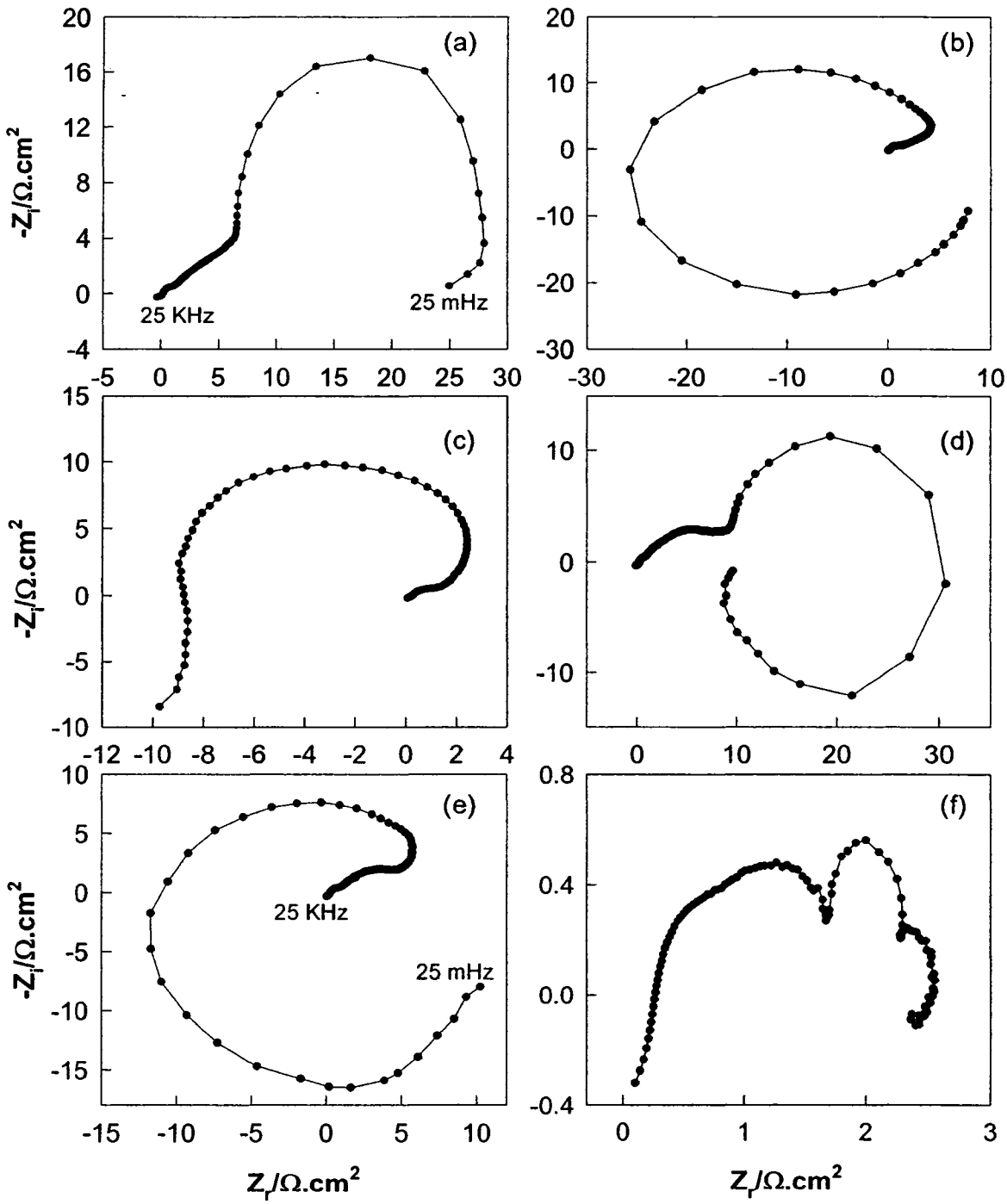

Fig. 4.6. EIS complex plane plots of the Ti/Ta_2O_5-IrO_2 electrode in 0.65 M Na_2S with the electrode potential: (a) -0.1 V; (b) -0.05 V; (c) 0.5 V; (d) 1.0 V; (e) 1.2 V; and (f) 1.4 V

show the presence of a hidden negative differential resistance (HNDR) (i.e., negative differential resistances in a region of intermediate frequencies and positive differential resistances in low frequencies). Thus, both Oscillation A and Oscillation B can be classified as HNDR oscillators with oxygen evolution involved (as shown later in the *in situ* images of the electrode surface). This conclusion can be further supported by the EIS results. The Nyquist plot at -0.05 V is similar to the plot at 1.2 V. At +1.0 and +1.4 V/SCE, only positive faradic impedance is seen. The oscillation vanished at current density j_2 = 45 mA/cm^2 and 75 mA/cm^2, where the corresponding potential is around 1.0 and 1.4 V, respectively. The positive real impedance for 1.0 V is consistent with the galvanostatic results: a broad shoulder is observed at the top part of the Oscillation A, and the potential range for Oscillation B is above 1.0V. Moreover, three capacitive loops presented in the frequency-dependent impedance (Fig. 4.6f) indicate a stable electrochemical system at 1.4 V with three chemical processes on different time scales.

4.5. Effect of Stirring and Purging on the Potential Oscillations

Figure 4.7 shows the effect of purging/stirring on the potential oscillations at 30 mA/cm^2. In Fig. 4.7(a), purging with ultrapure Ar starts at the bottom of the oscillation; while in Fig. 4.7(b), purging begins at the upper part of the oscillation. Curves 4.7(a) and 4.7(b) are almost identical, which indicates that the effect of purging is independent of the start point where the bubbling is applied during the potential oscillation. In Fig. 4.7(c), magnetic stirring was turned on at the bottom part of the oscillation. With either purging or stirring, the electrode potential stays at around -0.1 V and the oscillation disappears. This is

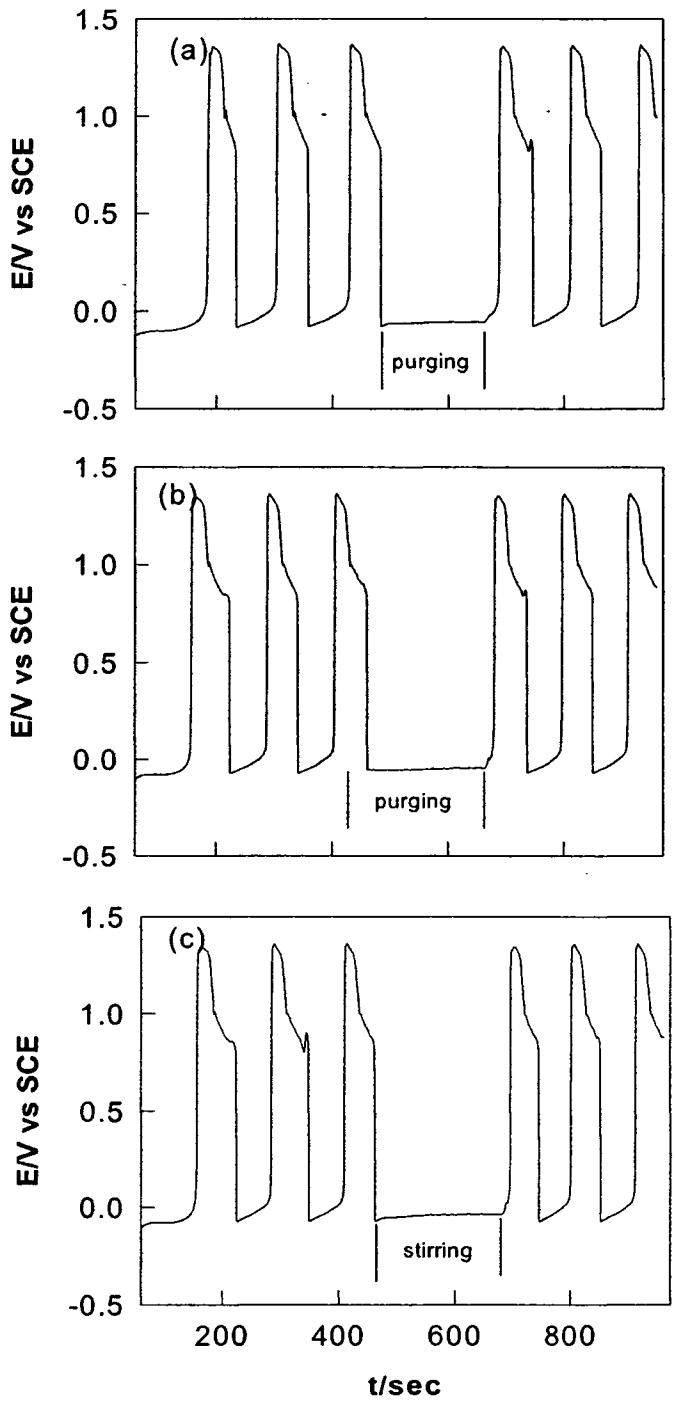

Fig. 4.7. Stirring/purging effects on the chronopotentiometric curves of 0.65 M Na_2S at 30 $mA.cm^{-2}$: (a) purging at bottom of the oscillation; (b) purging at top of the oscillation; (c) stirring at bottom of the oscillation

consistent with the above impedance study. Only positive impedance (rather than negative faradic impedance) was observed at the potential -0.1 V in the Nyquist plot. After the purging/stirring was turned off, the potential oscillation quickly recovers to its initial behavior.

Figure 4.8 shows the effect of purging/stirring on the potential oscillations in the Oscillation B region. With either stirring or purging at j_2 = 60 mA/cm^2, the periodic potential oscillations still appear in the galvanostatic curve. The shape of the wave form is similar to that without stirring and purging. The frequency of the oscillations is only slightly different from that without stirring. The amplitude of the potential oscillation becomes slightly larger with the stirring/purging, between 1.15 and 1.4 V. Based on the results of our impedance study (negative impedance observed at 1.2 V/SCE) one can predict that the potential oscillations can occur in this potential range. As shown in Fig. 4.8(c), the electrode potential at 85 mA/cm^2 is higher than 1.4 V and no potential oscillation is present in the galvanostatic curve. However, when the stirring is turned on, the electrode potential is lowered and the potential oscillations appear. The oscillations vanish right away when the stirring is stopped. All the above results are very consistent with our impedance study, and also indicate that mass transfer plays an important role in the potential oscillations during the electrooxidation of sulfide.

4.6. Oscillation Mechanisms

The mechanisms for the electrochemical oxidation of sulfide are complicated since sulfur has a number of different oxidation states such as -2, 0, +4 and +6. Anodic oxidation of sulfide can produce elemental sulfur, polysulfides or sulfur oxyanions depending on the

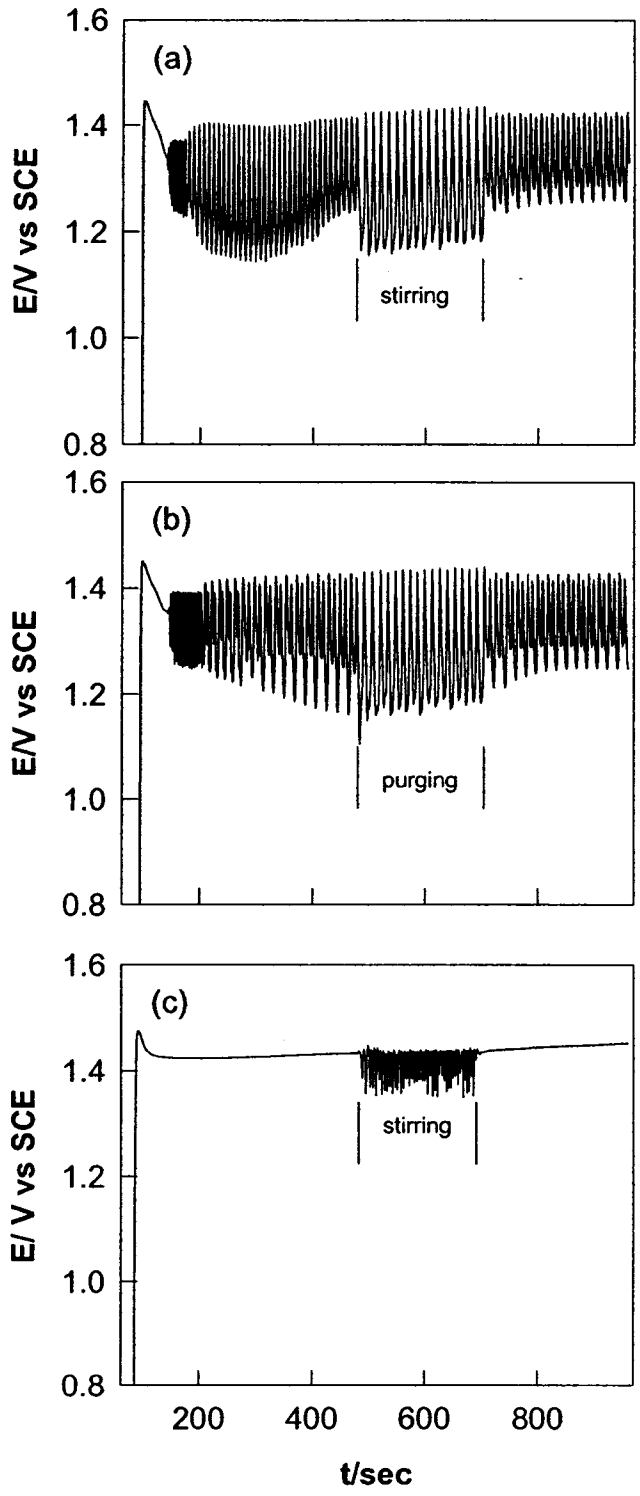

Fig. 4.8. Stirring/purging effects on the chronopotentiometric curves of 0.65 M Na_2S at: (a) 60 mA.cm^{-2} (stirring); (b) 60 mA.cm^{-2} (purging); and (c) 85 mA.cm^{-2} (stirring)

potential, pH and temperature of the electrolyte. As described in Section 4.2, the pH of the 0.65 M Na_2S electrolyte used in this study is close to the pH value of a 0.65M NaOH solution, which indicates that HS^- ions are the predominant species. Some possible anodic reactions [37, 41-43] are listed here:

$$HS^- + OH^- = S + H_2O + 2\ e^- \quad (4.1)$$

$$S^{2-} = S + 2\ e^- \quad (4.2)$$

$$2\ HS^- + 2\ OH^- = S_2^{2-} + 2\ H_2O + 2\ e^- \quad (4.3)$$

$$S_2^{2-} = 2\ S + 2\ e^- \quad (4.4)$$

$$HS^- + 9\ OH^- = SO_4^{2-} + 5\ H_2O + 8\ e^- \quad (4.5)$$

Figure 4.9 shows five *in situ* images of the electrode surface taken by a digital camera at 20 mA/cm^2 (Image a) where no potential oscillation occurs, at 35 mA/cm^2 in the Oscillation A region (Image c, d and e), and at 65 mA/cm^2 (Image f) where Oscillation B is located. Fig. 4.9b indicates where the images c, d and e were taken during the oscillation. Our galvanostatic study shows that the electrode potential is -0.1 V/SCE at 20 mA/cm^2. Under the potential -0.1 V, all the above listed anodic reactions can occur, except Reaction 5 as this takes place at much higher potential 1.1 V [43]. For instance, the electrode potentials for the reactions 1 and 2 are -0.48 and -0.51 V/SCE, respectively [42]. Hydrosulfide can be oxidized to sulfur and/or polysulfides. Sulfide and polysulfides can also be oxidized to form sulfur. However, there is no sulfur build-up on the electrode surface as shown in the image 4.9a. It has been reported that the sulfur layer can be dissolved by forming polysulfides [57], i.e.

$$S + HS^- + OH^- = S_2^{2-} + H_2O \quad (4.6)$$

$$S + S_2^{2-} = S_3^{2-} \quad (4.7)$$

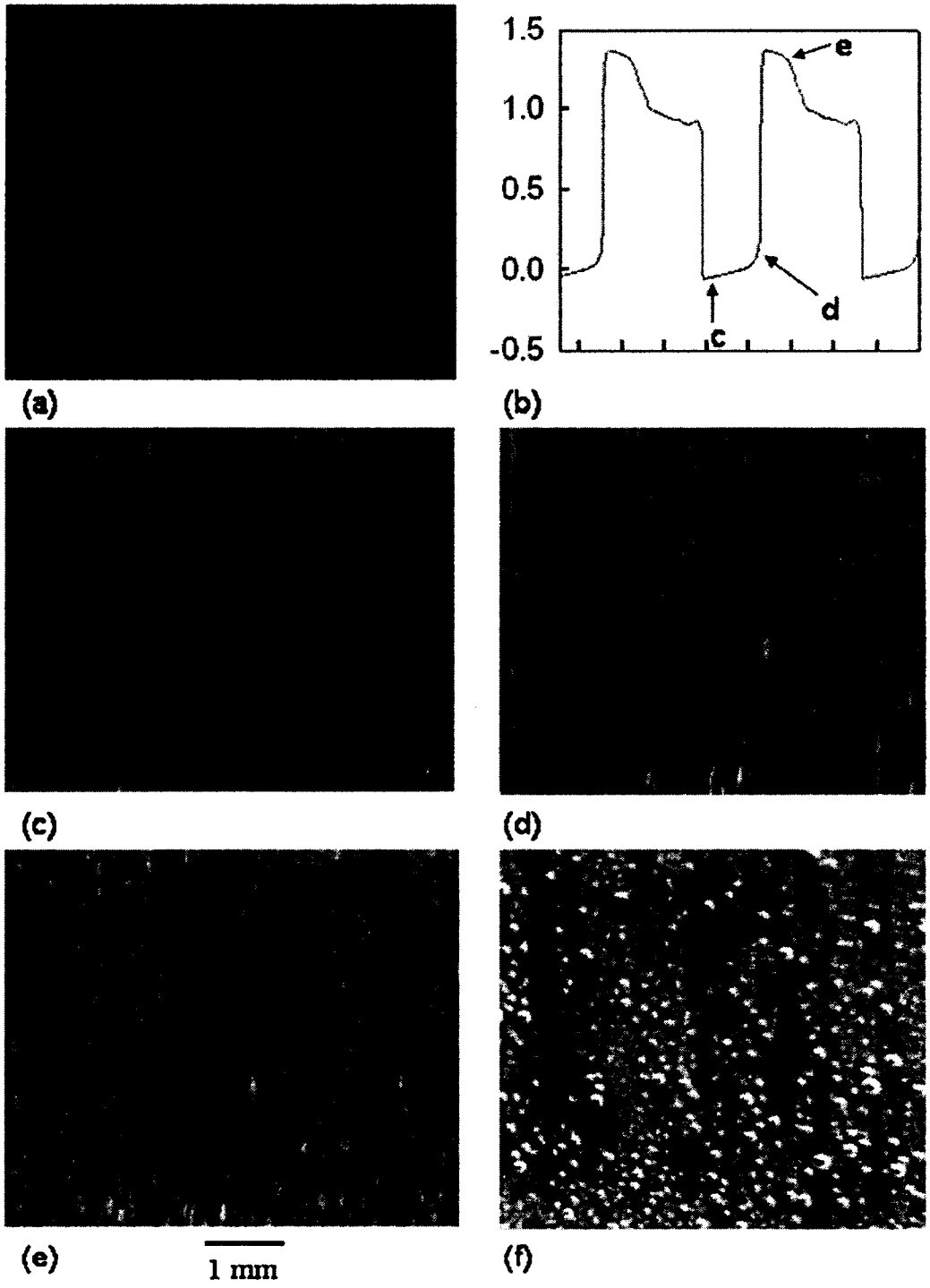

Fig. 4.9. *In situ* images of the Ti/Ta_2O_5-IrO_2 electrode surface at 20 mA/cm^2 (a), at 35 mA/cm^2 (c, d and e), and at 65 mA/cm^2 (f). Fig. 9b indicates where the images c, d and e were taken during the oscillation.

Thus, even if it occurred, one would not see sulfur build-up on the electrode surface, if the dissolution of sulfur is faster than its formation. This is also supported by the results shown in Fig. 4.8. The potential oscillations vanish and the electrode potential stays at around -0.1 V when the stirring/purging was turned on. The stirring/purging increases the mass transfer by moving HS^-, $S^{2-}$and OH^- to the electrode surface and moving sulfur away. Because there is no sulfur build-up on the electrode surface the potential oscillations vanish.

Fig. 4.9b shows the potential oscillations at 35 mA/cm^2 in the Oscillation A region. As shown in Fig. 4.9b, Images c and d were taken at the bottom part of the oscillation, and Image f was taken at the top portion of the oscillation. As seen in Images c and d, more and more sulfur deposits are formed on the electrode surface as the electrode potential increases from -0.1 to 0.0 V. The conductivity of the sulfur layer is very low, which explains why negative impedance is observed in the impedance spectrum at -0.05 V. Once the electrode potential reaches approximately 0.0 V, it jumps to around +1.4 V and then drops slowly. When the potential decreases to 0.9 V, it suddenly drops to -0.1 V. As seen in Image e, oxygen evolution is present in Oscillation A in the upper potential regions, which stops as the potential decreases according to the experiment results (Figure 2a and 3). In other words, periodic oxygen evolution occurs in Oscillation A. In addition, Oscillation A appears above the limiting current (Figure 2a and 3) and the current for the backward scanning is larger than that for the forward scanning (Figure 2a) for a range of potentials, while the potential is reversed at 1 V where oxygen evolution occurs. Oscillation A stops by imposing a constant convection as no depletion could occur because of stirring or purging (Figure 4.7). Thus, the variation of the S2-/HS- surface

concentration from the diffusion-limited depletion by oxidation and from the convection-induced replenishment by oxygen evolution, respectively, might be the main reason for oscillation A. The sulfur deposit/removal might also cooperate with the depletion/replenishment in Oscillation A, depletion accompanying sulfur deposition and replenishment accompanying sulfur removal. To test whether the sulfur deposits can be directly oxidized to sulfate or not, we first deposited sulfur on the electrode surface at 0.6 V for five mintues in a 0.65M Na_2S solution and then transferred the electrode into a 0.65 M NaOH solution. After five-minute electrolysis at 1.4 V in the 0.65M NaOH, we could still see sulfur deposits on the electrode surface. Therefore, the removal of sulfur from the electrode surface is mainly through forming soluble polysulfides rather than through oxidation of sulfur into sulfate.

As seen in image 4.9f, there are sulfur deposits and gas bubbles on the electrode surface at 65 mA/cm^2, where Oscillation B is located. As seen in Fig. 4.3, the potential range for Oscillation B is only a portion of Oscillaiton A. However, the rates for the electrode processes in Oscllation B are dramatically different from those in Oscillation A, since Oscillation B appears at a much higher current range. Oscillation B is irregular, and has much smaller amplitudes and higher frequencies in comparison with Oscillation A. The surface concentration of S^{2-}/HS^- depletes much more rapidly (higher frequency), and the oxygen evolution immediately becomes predominant, which prevents the S^{2-}/HS^- surface concentration from being completely restored resulting in smaller amplitude oscillations. As a result, oxygen evolution continuous and the electrode surface is similar to what is shown in Figure 4.9f although it may vary from time to time (irregular). Additional stirring of the solution is helpful to lower the potential by partially restoring the S^{2-}/HS^-

surface concentration. The negative potential shift is due to the stirring as shown in Figure 4.8. All these results indicate that the Oscillation B is due to the synergic effect of sulfur formation/removal and constant oxygen evolution.

4.7. Summary

The electrooxidation of sulfide on a microstructured oxide electrode Ti/Ta_2O_5-IrO_2 has been investigated by.a number of electrochemical methods such as cyclic voltammetry, differential capacity, galvanostatic measurements and electrochemical impedance spectroscopy. Sulfide and hydrosulfide can be oxidized to sulfur, polysulfides and sulfate depending upon the electrode potential. The SEM analysis shows that the Ti/Ta_2O_5-IrO_2 electrode prepared in this study has a 'cracked mud' structure with oxide particles sitting on the top. The particle size is around 100 nm. This oxide electrode has much larger surface area than planar metal electrodes such as Au and Pt. Two distinct ranges of galvanostatic potential oscillations, Oscillation A and Oscillation B, are observed during the electro-oxidation of sulfide on the oxide electrode. Oscillation A is in the range from 20 to 45 mA/cm^2, while Oscillation B is located in the region between 55 and 75 mA/cm^2. It is also found that mass transfer plays an important role in the potential oscillations. The variation of the S^{2-}/HS^- surface concentration from the diffusion-limited depletion by oxidation and from the convection-induced replenishment by periodic oxygen evolution, respectively, might be the main reason for oscillation A, while Oscillation B is due to the synergic effect of sulfur formation/removal and constant gas evolution. The EIS studies show that both Oscillation A and Oscillation B can be classified into a new type of HNDR oscillator with oxygen evolution involved. The oxide Ta_2O_5-IrO_2 is a promising electrocatalyst in the

electrochemical treatment of sulfide solutions, and the influence of the oscillations on the life time of the Ti/Ta_2O_5-IrO_2 is being investigated by our group. In summary, we have demonstrated that the electrooxidation of sulfide on the oxide electrode Ti/Ta_2O_5-IrO_2 is an excellent system for understanding the nature of the oscillations as one can directly observe the change of the electrode surface during the potential oscillations caused by sulfur formation/removal.

Chapter 5

Effect of concentration and temperature on electrochemical oscillations during sulfide oxidation on Ti/Ta_2O_5-IrO_2 electrodes

5.1. Cyclic voltammetry and linear galvanic voltammetry

Fig. 5.1a shows two cyclic voltammograms (CV) recorded at a sweep rate of 20 mV/s for solutions of 1.0 M Na_2S (solid line) and 1.0 M NaOH (dotted line). The onset of oxygen evolution for the sodium hydroxide solution occurs near 0.5 V and the current for oxygen evolution increases linearly with increasing potential. In comparison, when sweeping the potential from -0.8 to 1.8 V/SCE with sulfide present, a broad hump starting at approximately -0.65 V/SCE as well as a large wide peak centered at ~ 0.1 V is observed during the forward scan. This large wide peak could be due to sulfide oxidation to polysulfide or sulfur in combination with the chemical formation of polysulfides through dissolution of the sulfur layer on the electrode [Chapter 4]. The return scan demonstrates two sharp peaks with shoulders occurring at approximately 1.25 and 0.9 V as well as broader peaks occurring at 0.6 and 0.45 V. The numerous peaks shown in the CV curve indicate that many possible potential-dependent oxidative state sulfur compounds can be formed, most likely involving oxyanions of sulfur. In addition, Fig. 5.1b shows a linear galvanic voltammogram of a 1.0 M Na_2S solution ranging from 10 to 150 mA recorded at a sweep rate of 20 μA/s. Two potential oscillatory regions can be distinguished, with the first ranging from 40 to 105 mA and the second appearing from 110 to 135 mA. As can been seen in the galvanic voltammogram, the first oscillatory region is of large amplitude and high frequency whereas the second region appears to have a somewhat erratic amplitude and low frequency. Obviously, the potential oscillations strongly depend

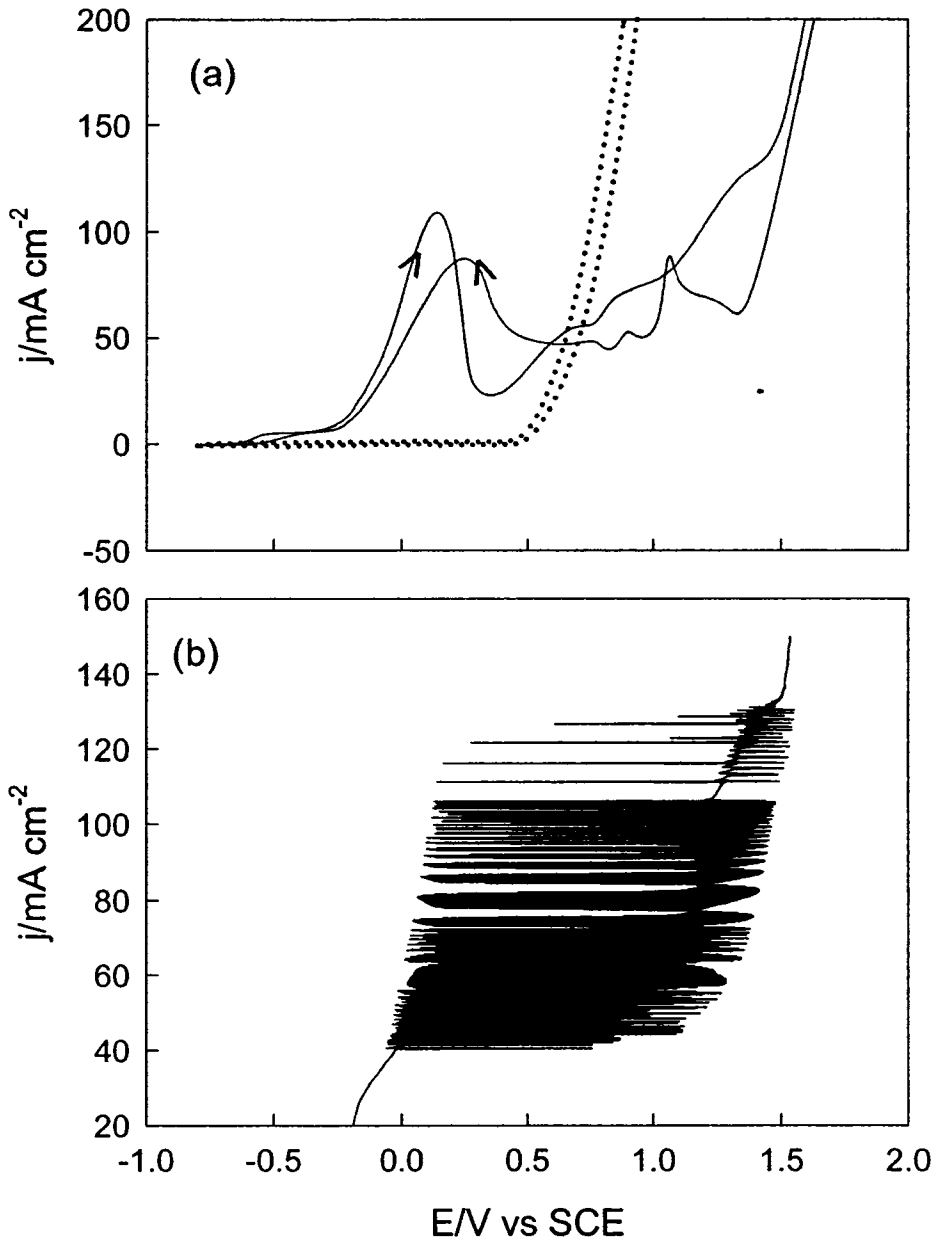

Fig. 5.1: (a) Cyclic voltammograms of 1.0 M Na_2S (solid line) and 1.0 M NaOH (dotted line) with a potential sweep rate of 20 mV/s and (b) linear galvanic voltammogram of 1.0 M Na_2S with a galvanic sweep rate of 20 μA/s.

on the applied current.

5.2. Effect of current densities on the potential oscillations

Fig. 5.2 presents a series of curves under galvanostatic conditions with current densities ranging from 40 to 125 mA/cm^2. In all cases the initial current density (j_1) was held at 0 mA/cm^2 for one minute and then stepped to j_2 and held there for 15 minutes. For clarity purposes, only the portion between 400 and 800 seconds of each experiment is shown in Fig. 5.2. As seen in Fig. 5.2a, at the low current density (j_2 = 40 mA/cm^2) the potential initially starts at around -0.05 V and slowly increases until the potential reaches 0 V where there is a sudden and large increase in potential to approximately 1.1 V. The potential then decreases to -0.05 V, with the appearance of a small shoulder around 0.75 V as the potential drops. As the current density is increased, both the frequency as well as the peak potential of the oscillation increases with the shoulder becoming more distinct. The observed shoulder then disappears once the current density is further increased to 95 mA/cm^2. At 125 mA/cm^2 (Fig. 5.2h), the character of the oscillations changes dramatically. The potential starts around 1.3 V and slowly increases until it reaches 1.35 V at which point the potential drops sharply to 0.1 V. These periodic potential oscillations are caused by the synergic effect of sulfur formation/removal and oxygen evolution at the high potential range. At the bottom part of the oscillations, the predominant reaction is sulfide oxidation to sulfur. Indeed, sulfur deposits were observed on the electrode surface. Because of the sulfur build up, the electrode potential increases. As shown in Fig. 5.1a, oxygen evolution strongly depends on the applied potential. When the electrode potential increases, oxygen evolution significantly increases. Thus, at the

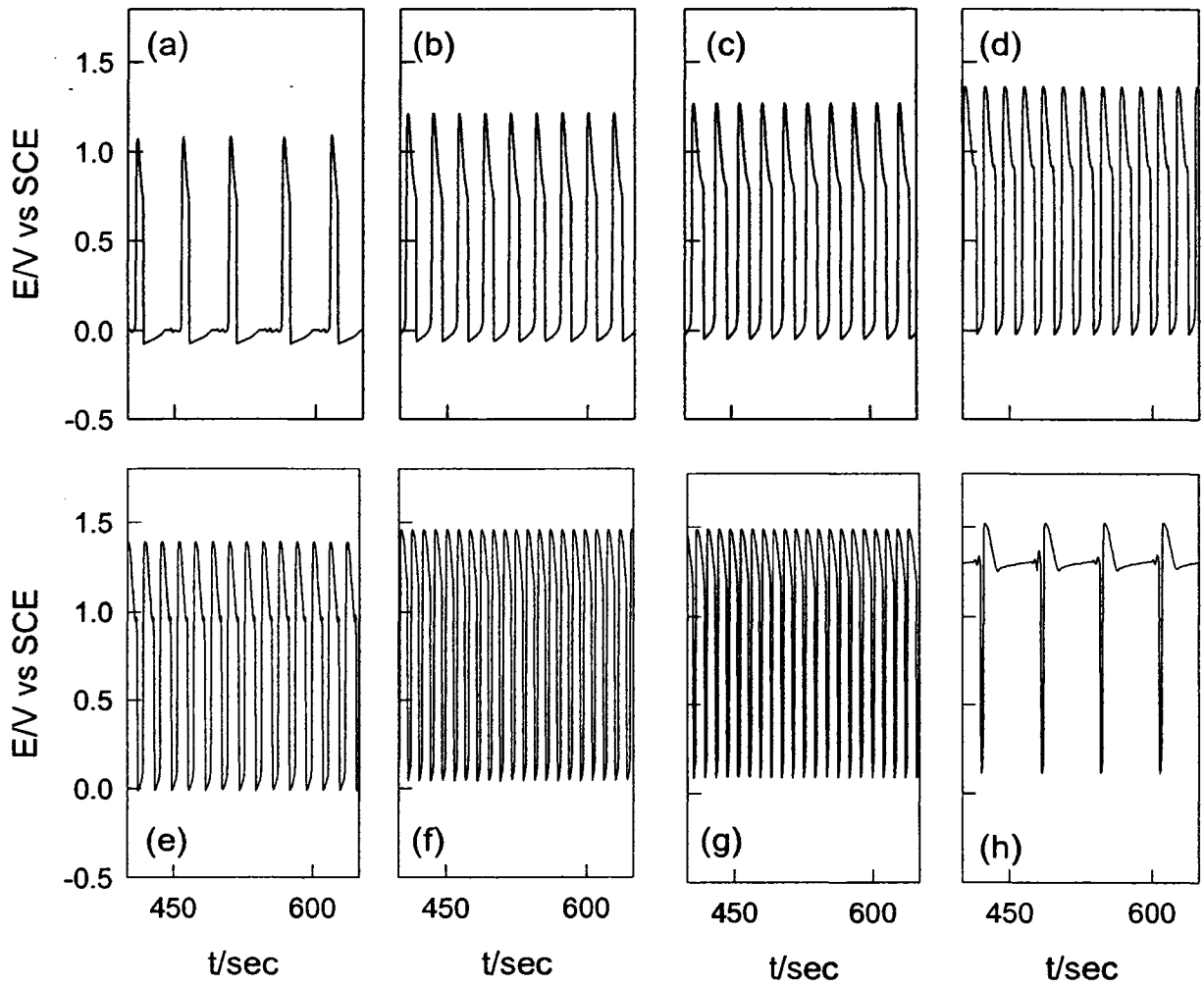

Fig. 5.2: Chronopotentiometric curves of 1.0 M Na_2S at: (a) 40 mA/cm^2; (b) 45 mA/cm^2; (c) 50 mA/cm^2; (d) 60 mA/cm^2; (e) 65 mA/cm^2; (f) 95 mA/cm^2; (g) 110 mA/cm^2 and (h) 125 mA/cm^2.

top part of the oscillations, oxygen evolution becomes the predominant reaction, i.e., much less sulfur is produced at the top part of the oscillations than at the bottom of the oscillations since the applied current is constant. Therefore, more HS^-/S^{2-} are used for sulfur dissolution at the top part of the oscillation than at the bottom of the oscillation. Furthermore, oxygen evolution increases mass transport, thus, more HS^-/S^{2-} are available for sulfur dissolution. The above results demonstrate that the applied current density has a large impact on the behavior of the potential oscillation, most notably affecting the amplitude and frequency.

5.3. Impact of concentration on potential oscillations

Fig. 5.3 shows four linear galvanic voltammograms (LGV) of Na_2S solutions with concentration of (a) 0.3 M, (b) 0.65 M, (c) 1.0 M and (d) 2.0 M. One oscillatory region is observed for the 0.3 M Na_2S solution, starting at ~10 mA/cm^2 and stopping at 20 mA/cm^2. The oscillation shows large amplitude with low frequency. Further increasing current density does not generate a second region of oscillation. Increasing the Na_2S concentration to 0.65 M (Fig. 5.3b), shifts the onset of oscillation to slightly above of 20 mA and extends the upper limit to 40 mA. These oscillations have similar amplitude to those observed for the 0.3 M case but the frequency is higher. The increased concentration also leads a second region of oscillation between 55 mA and 65 mA. This second region of oscillation has an appreciably reduced amplitude when compared to the first region but its frequency is significantly higher. As shown in Fig. 5.3c, a further increase of concentration to 1.0 M shifts the onset of potential oscillations to 40 mA. Also, the first region of oscillation is greatly expanded now ranging between 40 and 105

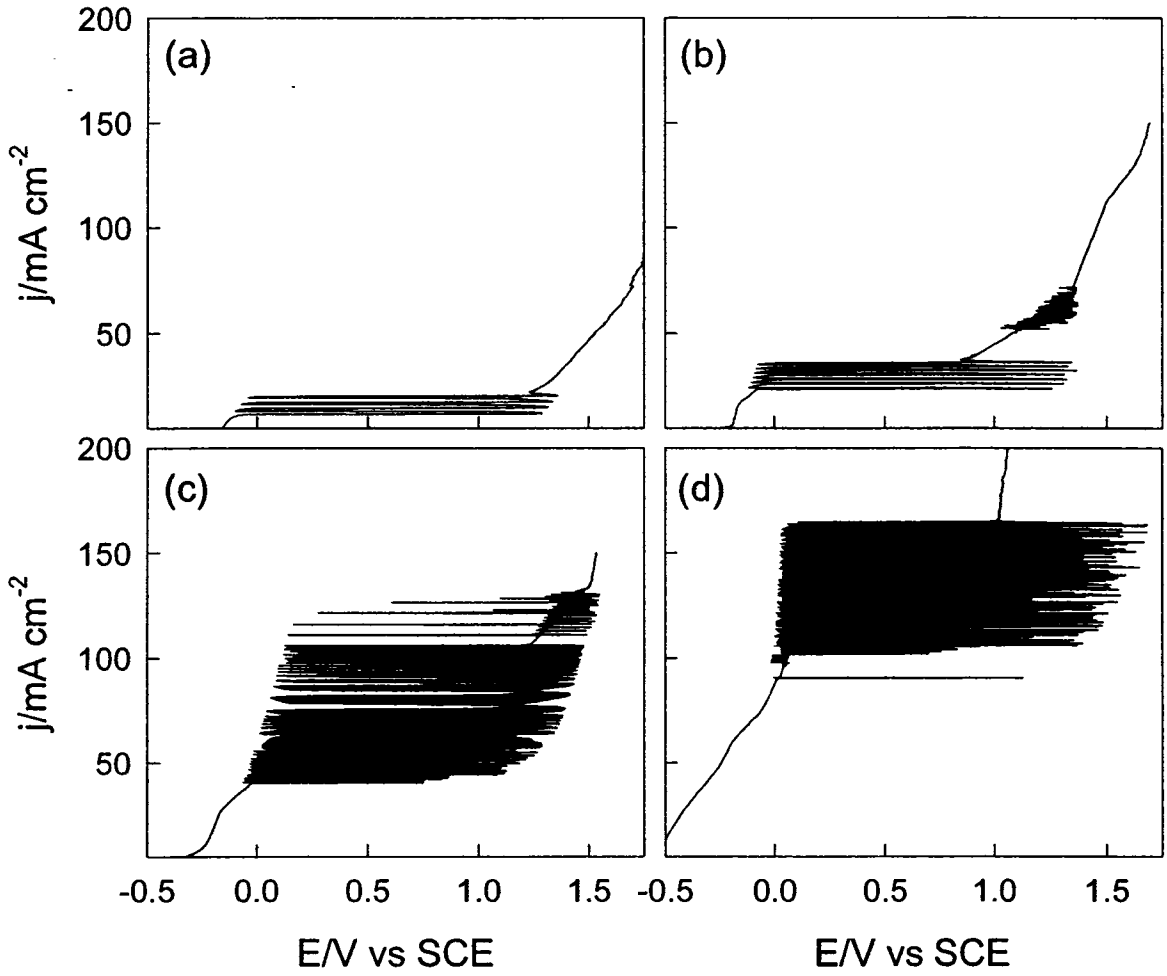

Fig. 5.3: Linear galvanic voltammograms of Na_2S: (a) 0.3 M; (b) 0.65 M; (c) 1.0 M and (d) 2.0 M.

mA. Again, although the amplitude is similar to the previous curves, the frequency of the oscillation has dramatically increased. The character of the oscillations located in the second region has also changed with a decrease in the frequency and non-periodic large potential drops are observed. Fig. 5.3d shows the linear galvanic voltammogram of the 2.0 M sulfide solution. The onset of oscillations occurs at 100 mA and runs up to 170 mA. Unlike in the 0.65 M and 1.0 M cases, only one oscillation range is observed. These four voltammograms demonstrate that sulfide concentration plays an important role in the appearance and location of potential oscillations. These results are consistent with the oscillatory mechanisms proposed in chapter 4 where by the oscillations are driven by a combination of formation/removal of the sulfur layer via sulfide oxidation, oxygen evolution and formation of polysulfides. The shift to higher current densities prior to the onset of potential oscillations for these solutions can be explained by the increase in sulfide concentration since chemical dissolution of the sulfur layer on the electrode surface increases with increasing sulfide concentration. The lack of a second oscillation region at the low sulfide concentration may be a result of insufficient sulfide in solution to remove the sulfur layer faster than it can be formed at higher current densities. The 2.0 M sulfide also yielded only one oscillatory region which can most likely be attributed to the opposite case: where the sulfide in solution is in a high enough concentration, in combination with oxygen evolution, to prevent the formation of any significant sulfur layer. This is further supported by the potential that is observed after the oscillations have finished. After the oscillations stop the potential stays around 1.0 V, whereas in the other three solutions the potential observed after the oscillations stop approaches or exceeds 1.5 V, indicating a thicker sulfur layer is present at higher current

densities. The influence of sulfide concentration was further investigated using electrochemical impedance spectroscopy (EIS).

5.4. Impact of concentration on the switch point potential for negative faradaic impedance

Fig. 5.4 presents six EIS complex plane plots of the Ti/Ta_2O_5-IrO_2 electrode in (a, b) 0.3 M Na_2S, (c, d) 0.65 M Na_2S and (e, f) 1.0 M Na_2S. As seen in Fig. 5.4a, c and e, only positive faradic impedance is observed at –0.2 V for these three different concentrations. Negative faradic impedance is observed for all three concentrations (Fig. 5.4b, d and f) at less negative electrode potentials. The onset potential for negative faradaic impedance increases with increasing sulfide concentration. At 0.3 M Na_2S (Fig. 5.4b) the onset potential for negative faradic impedance occurs at –0.1 V. At 0.65 M Na_2S (Fig. 5.4d) it shifts to –0.05 V. For both 1.0 M and 2.0 M Na_2S solutions negative faradic impedance is first observed at 0.0 V. Therefore we did not include the impedance spectra for 2.0 M Na_2S in Fig. 5.4. These results are consistent with the LGV shown in Fig. 5.3. In Fig. 5.3a, which corresponds to the 0.3 M sulfide solution, the initial potential during the oscillation is ~ -0.1 V. The initial potential for oscillation in 0.65 M Na_2S (Fig. 5.3b) also shows similar characteristics with it starting at ~ -0.05V. At 1.0 M and 2.0 M sulfide solutions (Fig. 5.3 c, d) the onset potential for the oscillation is 0 V. All these results show that the EIS and LGV studies are in excellent agreement with the effect of sulfide concentration on the behavior of the oscillations.

To understand the EIS spectra, equivalent circuits were used to fit the experimental EIS data presented in Fig. 5.4. The circuit shown in Fig. 5.5a was used to fit the positive faradic impedance spectra shown in Fig. 5.4a, c and e; and the

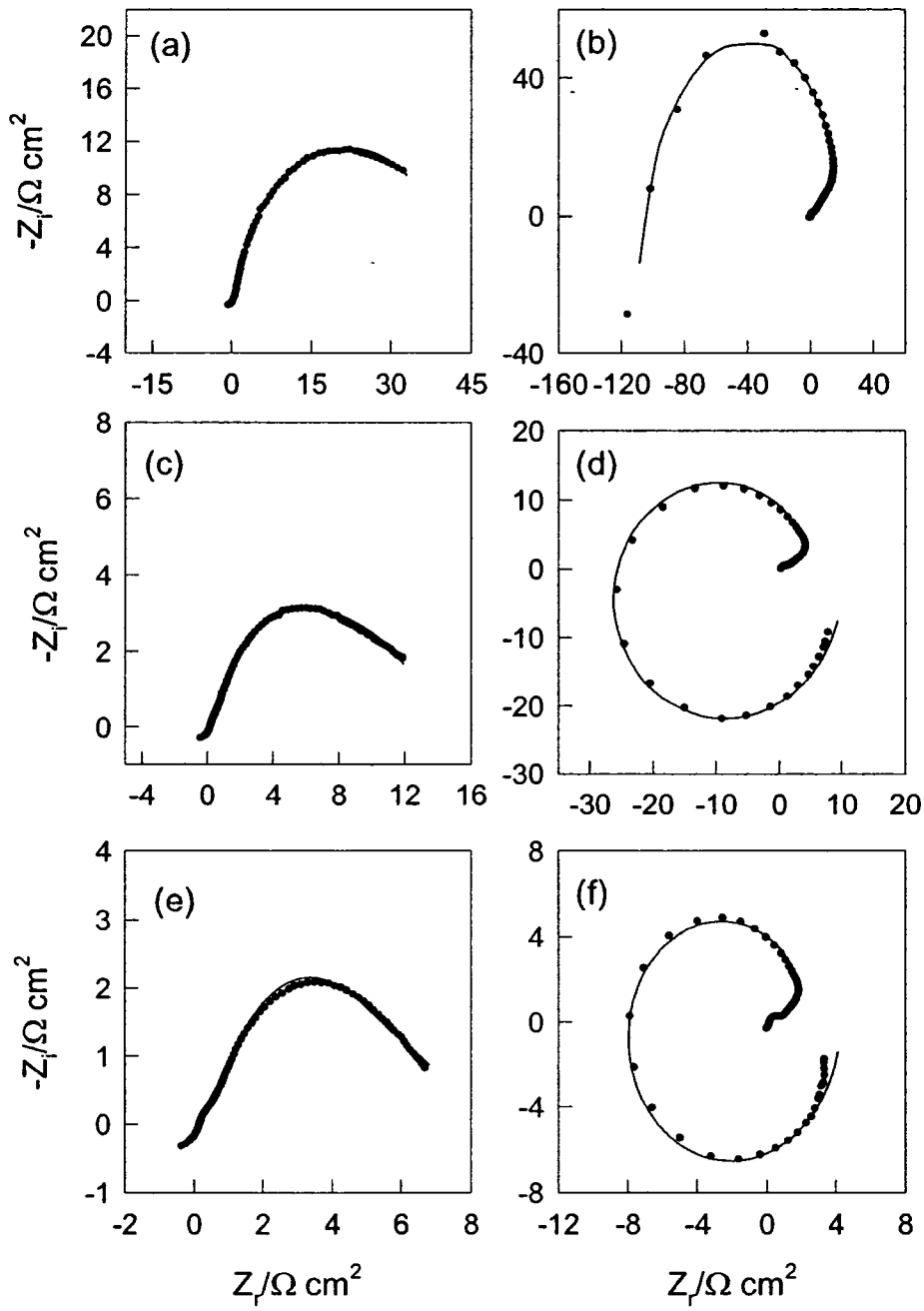

Fig. 5.4: EIS complex plane plots of: 0.3 M (a & b), 0.65 M (c & d) and 1.0 M (e & f) Na_2S. The electrode potential for (a, c & e) was -0.2 V. The impedance spectra (b, d & f) were recorded at the onset potential of the negative faradiac impedance: (b) -0.1 V, (d) -0.05 V and (f) 0.0 V. Symbols: experimental data. Solid lines: fitted results.

circuit shown in Fig. 5.5b was employed to fit the negative impedance spectra shown in Fig. 5.4b, d and f. The fit results match the experimental data very well indicating that the circuits selected can be considered valid. In both circuits, Rs takes into account the solution resistance, the parallel combination of RfCf takes into account the properties of the oxide film [69] and the second parallel combination of R1CPE1 is associated with the oxidation of sulfide. A CPE is composed of two portions: CPE-T and CPE-P. If CPE-P is equal to one then it can be considered a capacitor. The use of a R1CPE1 when CPE1-P is < 1 leads to the generation of a depressed semicircle in complex plane plots. It has been reported earlier that the use of a CPE circuit element as opposed to a capacitor in fitting impedance data obtained from porous type electrodes better accounts for the inhomogenities of the surface structure of the coating material [70]. Circuit b contains additional elements of a resistor (R2) and a capacitor (C2) in parallel with R2 in series with another parallel combination of a resistor (R3) and capacitor (C3). The addition of this second branch takes into account sulfur deposits as well as other specific adsorbed species formed on the electrode surface which generates the negative impedance [66]. The values obtained from fitting the experimental data are presented in Tables 1 and 2. Table 1 presents the data obtained from the fit results of the experimental data for positive impedance (Fig. 5.4a, c, and e) using the circuit shown in Fig. 5.5a. The resistances associated with the oxidation of sulfide decrease with increasing concentration, also the CPE values are shown to increase with increasing concentration. Table 5.2 presents the data obtained from fitting the experimental results shown in Fig. 5.4b, d and f. The elements R2 and C2 shown in Table 5.2 are negative. This is in good agreement with the start of oscillations occurring at these potentials for the three

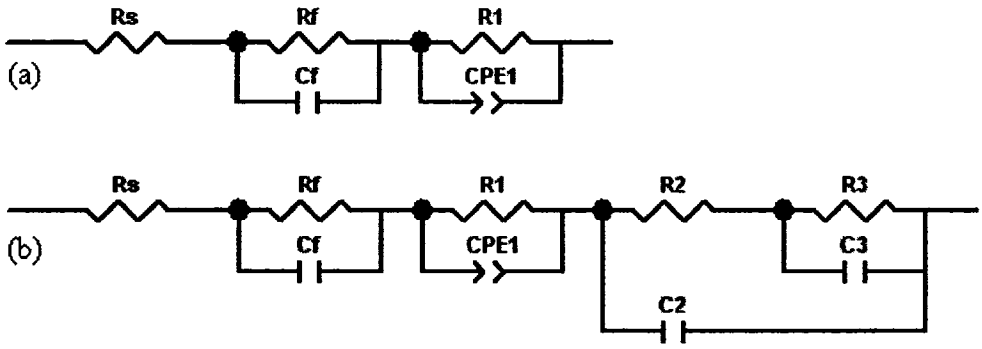

Fig. 5.5: Equivalent circuits used to fit experimental data from Fig. 4: (a) positive impedance and (b) negative impedance

Table 5.1: Impedance Components for the Positive Faradaic Impedance Fitted by the Equivalent Circuit Shown in Figure 5a.

Concentration (mol/L)	Potential (V)	Rf (Ω cm^2)	Cf (mF cm^{-2})	Rct (Ω cm^2)	CPEct-T (mF cm^{-2})	CPEct-P
0.3	-0.2	5.26	14.9	38.63	17.8	0.66
0.65	-0.2	1.88	16.7	11.91	32.3	0.54
1.0	-0.2	2.4	21.3	5.4	76.4	0.46

Table 5.2: Impedance Components for the Negative Faradaic Impedance Fitted by the Equivalent Circuit Shown in Figure 5b.

Concentration (mol/L)	Potential (V)	Rf Ω cm^2	Cf mF cm^{-2}	R1 Ω cm^2	CPE1 mF cm^{-2}	R2 Ω cm^2	C2 mF cm^{-2}	R3 Ω cm^2	C3 mF cm^{-2}
0.3	-0.1	1.67	0.22	16.63	16.5	-86	65.9	125	-68.4
0.65	-0.05	0.79	0.22	3.58	19.1	-19.9	45.1	25.6	-29.4
1.0	0	1.2	15.9	0.82	16.9	-9	42.9	10.54	-83.9

different concentrations. The large values associated with R3 for all concentrations are also an indication that there are sulfur deposits on the electrode since sulfur has poor conducting properties. The R3 values are also consistent within themselves. The largest value of R3 is observed for the 0.3 M Na_2S solution while the smallest is observed for the 1.0 M Na_2S solution. This demonstrates an increase in the sulfur layer at lower concentrations compared to that at the higher concentrations, giving rise to negative impedance at lower potentials for lower sulfide concentrations. This is very consistent with the impact of concentration on the LGV's.

5.5. Effect of temperature on the oxidation of sulfide

Fig. 5.6a presents three linear voltammograms from -0.8 to 1.35 V at a scan rate of 20 mV/s and T = 2, 40, and 60 °C. At 2 °C, the current densities are significantly reduced in the S^{2-}/HS^- oxidation region as well as in the oxygen evolution reaction (OER) region. At room temperature (Fig. 5.1a), the peak current density raises to ~120 mA. Increasing the temperature to 40 °C gives rise to an increase in the peak current density from ~120 mA at 22 °C to over 200 mA as well as an overall increase in current density for the OER region (Fig. 5.6a). Increasing the temperature to 60 °C yields a significant increase in current density in the HS^-/S^{2-} oxidation region, the peak current density being 350 mA. Also, increasing temperature shifts the location of the peak current density to higher potential. As can be seen from Fig. 5.6a, the peak current density at 2 °C is located at ~160 mV, at 40 °C the location of the peak current density shifts to ~255 mV. Finally, at 60 °C, the peak current density shifts to an even higher potential (335 mV). The activation energy (E_a) can be calculated as outlined by De Silva et al [71]. Where the rate of electrode processes can be expressed in terms of current density (j) if the energy of the

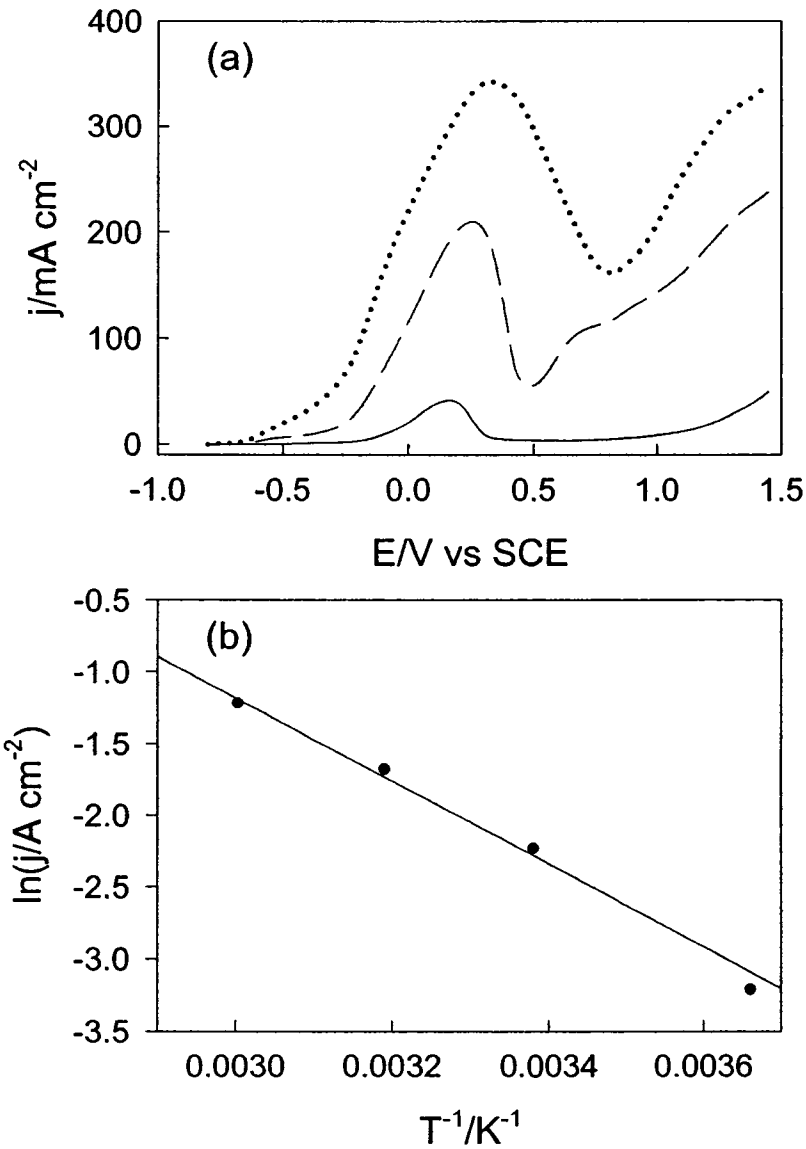

Fig. 5.6: (a) Linear voltammograms of 1.0 M Na_2S with a potential sweep rate of 20 mV/s at 2 °C (solid line); 40°C (dashed line); and 60°C (dotted line). (b) Arrhenius plot for sulfide oxidation at 0.16 V.

reactant follows a Maxwell distribution:

$$j = k*\exp(-E_a/R*T) \qquad (5.1)$$

where k is the rate constant, E_a is the activation energy, R is the gas constant, and T is the temperature in Kelvin. De Silva et al also demonstrated that activation energy is a function of the overpotential (η) and is related by the following equation [71]:

$$E_a^{\eta} = E_a - \alpha_T*F*\eta \qquad (5.2)$$

with α_T the transfer coefficient at constant temperature, and F the Faraday constant. Therefore, at a constant overpotential η, one can calculate the activation energy from the dependence of j on temperature (Arrhenius plot) using the following relation:

$$(d\ln j/dT^{-1})_{\eta} = -(E_a^{\eta}/R) \qquad (5.3)$$

In determining the activation energy for sulfide oxidation the current densities corresponding to the peak current density potential for the CV curve of the oxidation of sulfide at 2 °C was selected. This corresponds to a potential of 0.16 V and gives current densities of 40, 107, 187 and 295 mA/cm^2 for 2, 22, 40 and 60 °C, respectively. Fig. 5.6b shows the resulting Arrhenius plot for the current densities at 0.16 V and gives an activation energy for the oxidation of sulfide of 24 kJ/mol.

Continuing the investigation into the temperature effects on the electroxidation of sulfide, Fig. 5.7 presents the effect of temperature on the potential oscillations observed during a linear galvanic voltammetric study. Fig. 5.7a shows a LGV of 1.0 M Na_2S taken at 2 °C. For the selected current range a steady increase in potential is observed with no oscillations present. This indicates that there is no periodic formation and removal of sulfur on the surface at such a low temperature. Increasing the temperature to 40 °C (Fig. 5.7c), yields a large increase in current prior to the onset of oscillations. The onset of

oscillations now occurs around 80 mA instead of 40 mA, as observed at room temperature (Fig. 5.7b). The frequency of the oscillation is somewhat erratic with some fluctuations in the amplitude as well. A further increase in temperature to 60 °C gives a significant increase in current to ~145 mA before the onset of oscillations occurs as seen in Fig. 5.7d. The overall amplitude of the potential oscillations at 60 °C appears to be slightly reduced when compared to those observed at 40 °C and 22 °C. These results demonstrate that the behavior and appearance of the potential oscillations is highly dependant on the applied temperature. They also show that increased temperature prevents the formation of a sulfur layer on the electrode until the rate of formation of the sulfur layer exceeds that of the rate of dissolution, which can only occur at high current densities. This is due to: (1) increasing temperature increases the mass transfer of HS^- /S^{2-} ions from the bulk solution to the electrode surface; and (2) increasing temperature promotes the sulfur dissolution and polysulfides formation (Reaction 4 & 5). Thus, the periodic formation and removal of sulfur occurs at a higher current density when increasing temperature.

5.6. Effect of potential oscillations on electrode lifetime

In an effort to determine the impact of the potential oscillations on electrode lifetime, investigations were performed at four different current densities in a 1.0 M Na_2S solution. Current densities were selected to determine the behavior of the Ti/Ta_2O_5-IrO_2 towards sulfide oxidation below the first oscillation region (20 mA/cm^2), in the first oscillation region (65 mA/cm^2), in the second oscillation region (125 mA/cm^2) and at 180 mA/cm^2 (which is well above both oscillation regions). The Ti/Ta_2O_5-IrO_2 electrode has excellent activity towards oxygen evolution [35] as well as strong affinity for sulfide

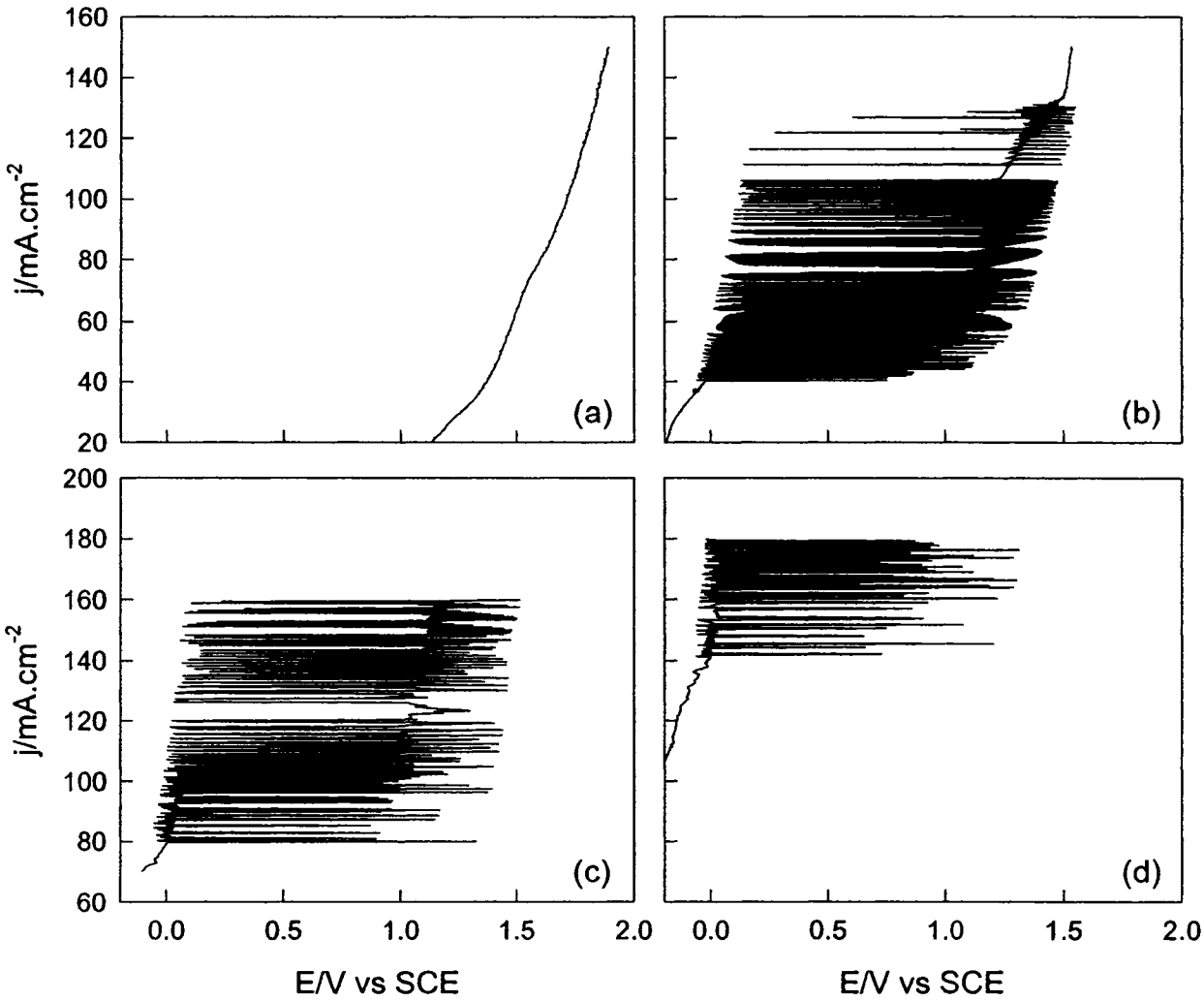

Fig. 5.7: Linear galvanic voltammograms of 1.0 M Na_2S with a galvanic scan rate of 20 μA/s at: (a) 2 °C; (b) 22 °C; (c) 40 °C; and (d) 60 °C.

oxidation [Chapter 4], indicating the possibility of a long lifetime. Our investigations are not directed towards total electrode deactivation. Instead, we selected an endpoint of 200 hours which gives a good indication of the impact of potential oscillations during sulfide oxidation on the electrode lifetime.

EIS studies were performed to determine the change in the electrical behavior of the electrodes after 200 hours of operation at the selected current densities. Fig. 5.8a shows five complex plane EIS spectra of the Ti/Ta_2O_5-IrO_2 electrodes in 1.0 M NaOH at 0.5 V which corresponds to the onset of oxygen evolution for the Ti/Ta_2O_5-IrO_2 electrode. Before the lifetime tests, all four Ti/Ta_2O_5-IrO_2 electrodes were characterized in 1.0 M NaOH; their impedance spectra are very similar and are represented by Curve 1. After the lifetime tests, the electrodes were washed completely using NANOpure water and then heated using a hot plate to ~ 200 °C for 20 minutes. Curves 2 – 5 are the corresponding impedance spectra after the 200-hour test at 20, 180, 125 and 65 mA/cm^2 respectively. Compared to the fresh Ti/Ta_2O_5-IrO_2 (Curve 1), all tested Ti/Ta_2O_5-IrO_2 electrodes exhibit an increase in impedance. The EIS studies indicate an almost ten fold increase in impedance for the electrode that was run at 65 mA/cm^2 (Curve 5) followed by larger impedance for the second oscillation region (125 mA/cm^2, Curve 4). As expected, the impedance spectrum associated with the electrode run at 20 mA/cm^2 (Curve 2) shows the smallest increase in impedance. Surprisingly, the highest current, density 180 mA/cm^2 (Curve 3), does not give rise to the largest increase in impedance, indicating that the oscillatory regions have a detrimental impact on the electrode lifetime.

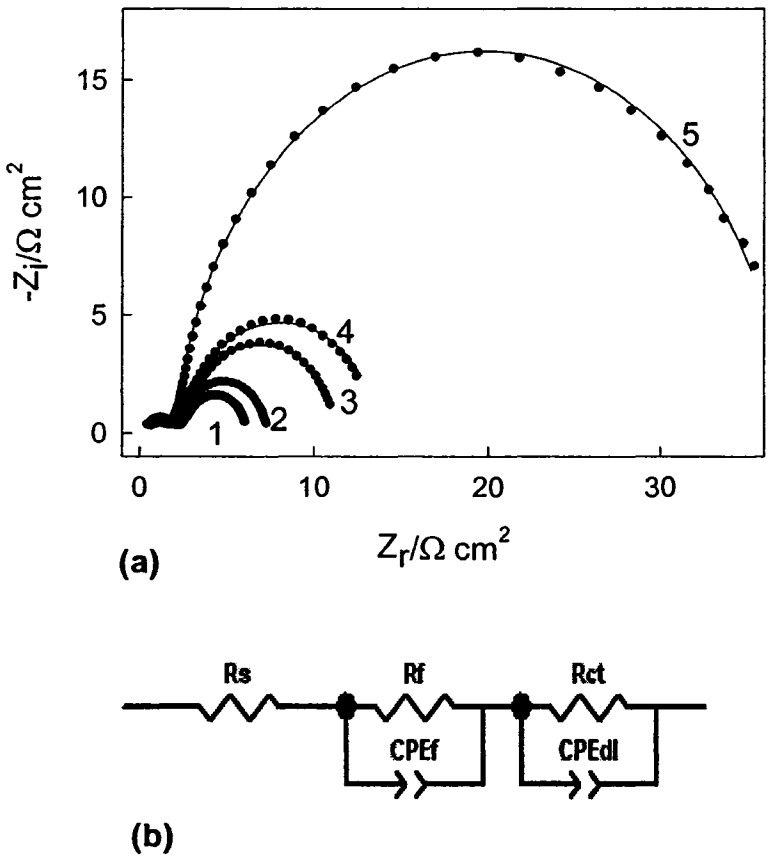

Fig. 5.8: (a) EIS complex plane plots of Ti/Ta_2O_5-IrO_2 electrode in 1.0 M NaOH at 0.5V vs SCE: Curve 1: initial; Curve 2 – 5: the corresponding impedance spectra after the 200-hour test at 20, 180, 125 and 65 mA/cm^2, respectively. (b) Equivalent circuit used to fit impedance spectra. Symbols: experimental data. Solid lines: fit results.

Table 5.3: Impedance Components for the Oxygen Evolution Reaction Fitted by the Equivalent Circuit Shown in Figure 8b.

Electrode	Rf	CPEf-P	CPEf-T	Rct	CPEdl-P	CPEdl-T
	$\Omega\,cm^2$	$mF\,cm^{-2}$		$\Omega\,cm^2$	$mF\,cm^{-2}$	
Initial	2.35	13.3	0.38	3.087	79.8	0.94
20 $mA\,cm^{-2}$	1.73	5.3	0.51	4.87	38.1	0.85
65 $mA\,cm^{-2}$	1.55	7.4	0.52	26.48	14.2	0.95
125 $mA\,cm^{-2}$	1.82	0.79	0.73	10.6	30.8	0.86
180 $mA\,cm^{-2}$	1.86	1.8	0.60	7.96	38.4	0.86

The equivalent circuit shown in Fig. 5.8b was used to fit the experimental data shown in Fig. 5.8a, where the symbols represent the experimental data and the solid lines indicate the fit curves. In this Rs(RfCPEf)(RctCPEdl) circuit, the normal notations are applicable where Rs is the solution resistance and RfCPEf corresponds to the film properties [69]. The combination of Rct and CPEdl takes into account the charge transfer resistance and double layer capacitance associated with the oxygen evolution reaction. In our initial fitting trials a capacitor was put in place of both CPE elements. The fitting results did not correspond well to the experimental data. Table 5.3 gives the resulting data obtained from fitting the experimental data using the circuit shown in Fig. 5.8b. In general, a slight decrease is observed in the film resistance (Rf) and the film capacitance (CPEf-P). The charge transfer resistance shows similar trends with the largest increase found to correspond to the first oscillation region (26.48 Ω cm^2) and the smallest increase with the electrode tested at 20 mA/cm^2. Based on the impedance results, the electrode lifetime t would change in the following order:

$$t\,(20\ \text{mA/cm}^2) > t\,(180\ \text{mA/cm}^2) > t\,(125\ \text{mA/cm}^2) > t\,(65\ \text{mA/cm}^2)$$

The periodic formation and removal of sulfur at 65 mA/cm^2 from the electrode surface would greatly decrease the electrode lifetime. The surface morphology of the IrO_2-Ta_2O_5 oxide coatings was examined by scanning electron microscopy (SEM). Fig. 5.9 shows SEM images of (a) the unused oxide coating and (b) the electrode tested at 65 mA/cm^2. Compared to the unused sample, the tested sample is seriously corroded. Our weight measurements before and after the 200-hour lifetime test reveal that the sample tested at 65 mA/cm^2, where harmonic potential oscillations were observed, has the highest weight loss. These results indicate that the observed potential oscillations have a detrimental

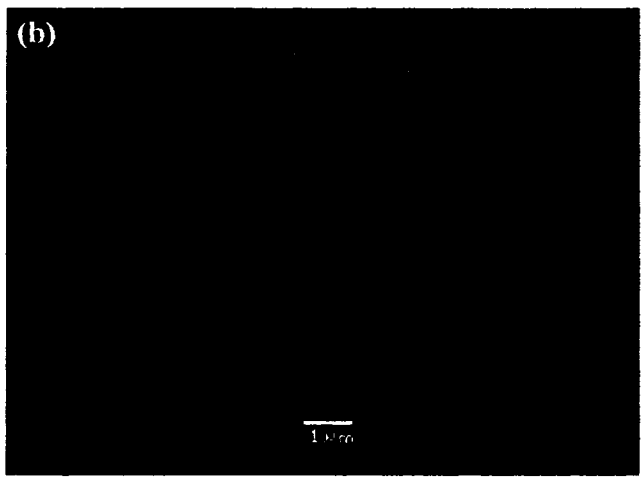

Fig. 5.9: Scanning electron micrographs of the Ti/Ta_2O_5-IrO_2 electrodes: (a) unused; and (b) after a 200-hour test at 65 mA/cm^2 in 1.0 M Na_2S solutions. Magnification: x 10,000.

impact on electrode lifetime.

5.7. Deactivation Mechanism of Ta_2O_5-IrO_2 during Sulfide Oxidation

To further understand the impact of both oscillations and sulfide oxidation on the lifetime of Ta_2O_5-IrO_2 electrodes we continued the lifetime experiments until the first deactivated (point at which a large increase in potential is observed) anode occurred. The primary deactivation mechanism of IrO_2-based DSA® is coating consumption [72-73]. This can be caused by chemical consumption associated with interactions involving the electrolyte or impurities, electrochemical consumption (electrooxidation and dissolution of the metal oxides), and/or erosion of the oxide particles by way of gas evolution which can lead to detachment of coating particles. In addition to coating consumption it is also possible to form an insulating TiO_2 interlayer between the Ti substrate and the oxide coating. This can occur during the calcination process [74] where the substrate is oxidized to TiO_2. It can also occur from selective loss of catalysts and active sites of the coating allowing for the substrate to be exposed to the electrolyte and the anodic oxidation of the Ti substrate to TiO_2 [75]. The deactivation point in this study corresponds to the electrode run at 65 mA cm^{-2} and a time of 360 hours. Figure 5.10 presents the resulting CV (Figure 5.10a) and EIS (Figure 5.10b) of the initial and final electrochemical characterizations. It has long been known that the integration of a CV curve in the double-layer region is proportional to the active surface area of a DSA®, giving an indication of the number of active sites on the electrode surface [35]. The CV curve after 360 hours (dotted line) shown in Figure 5.10a demonstrates a significant decrease in the EASA when compared to the initial characterization (solid line). Integration of the region between the hydrogen and oxygen evolution regions indicates a

16-fold decrease in the EASA after 360 hours of oxidation of sulfide in the first oscillatory region. Figure 5.10b presents the EIS spectra of both the initial characterization (circles) and the deactivated characterization (triangles) in 1.0 M NaOH at 500 mV of the Ta_2O_5-IrO_2 anode. The EIS spectrum of the deactivated Ta_2O_5-IrO_2 shows a significant increase in impedance compared to the initial Nyquist plot. This is very consistent with the observed results for the CV studies where a significant decrease in the EASA is observed. Figure 5.11a shows the SEM image of the deactivated Ta_2O_5-IrO_2 anode. When compared to the fresh Ta_2O_5-IrO_2 anode we can see that significant degradation of the oxide coating has occurred to such an extent that the cracked mud structure is now completely absent. The EDS spectra shown in Figure 5.11b further support this as well. The spectrum of the fresh Ta_2O_5-IrO_2 anode shows well defined peaks associated with Ta and Ir and the absence of evidence of Ti (indicating little to no TiO_2 was formed during the electrode fabrication process). However, after deactivation of the Ta_2O_5-IrO_2 anode the peaks associated with Ta are completely absent and the generation of a very strong Ti peak occurs. This is further supported with elemental analysis. The initial composition of the fresh Ta_2O_5-IrO_2 anode was 70% IrO_2, 30% Ta_2O_5 and 0% TiO_2. At the end of its lifetime the composition of the anode has changed dramatically. The final composition of the anode was 20% IrO_2, 0% Ta_2O_5, and 80% TiO_2 indicating the preferential dissolution of Ta_2O_5 from the coating mixture. The above information the deactivation mechanism of the Ta_2O_5-IrO_2 anode during sulfide oxidation in the first oscillatory region can be described as follows: 1) the oscillations accelerate the removal of loosely bound coating particles, 2) preferential chemical dissolution of the Ta_2O_5 component of the Ta_2O_5-IrO_2 anode, and 3) the loss of Ta_2O_5

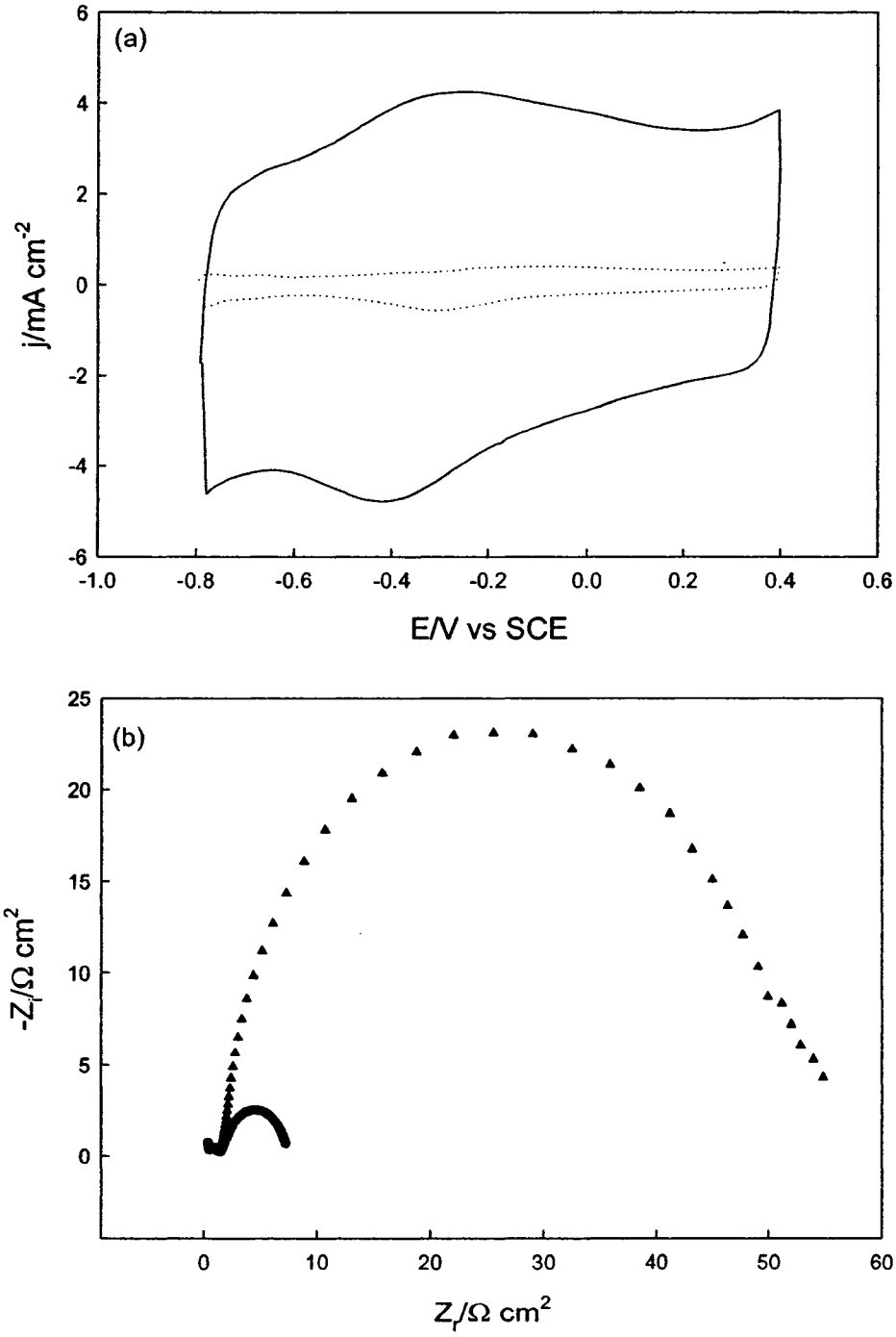

Figure 5.10. (a) Cyclic voltammogram of initial (solid) and deactivated (dotted) Ta_2O_5-IrO_2 electrode in 1.0 M NaOH. (b) EIS complex plane plots of initial (circle) and deactivated (triangle) Ta_2O_5-IrO_2 in 1.0 M NaOH at 500 mV.

opens up the Ti substrate to the electrolyte allowing for its oxidation to non-conducting TiO_2. Therefore the primary deactivation mechanism for this process is the oxidation of the Ti substrate to form non-conducting TiO_2. However, the manner in which this process occurs is quite different from the loss of the electroactive component that is traditionally found to be the cause of the formation of the TiO_2 insulating layer. To the best of our knowledge this is the first time that the loss of Ta_2O_5 (stabilizing component of the oxide mixture) has been the cause of the deactivation of a Ta_2O_5-IrO_2 anode.

Consequently, when using an electrochemical process to treat a sulfide solution, one should try to avoid potential oscillations in order to achieve a long lifetime for Ti/Ta_2O_5-IrO_2 electrodes.

5.8. Conclusions

The influence of current density, concentration and temperature on the electrochemical oscillations during anodic oxidation of sulfide on the Ti/Ta_2O_5-IrO2 oxide electrode was investigated. The observed potential oscillations are caused by the periodic formation/removal of sulfur from the electrode surface. Increasing current density increases the frequency of the potential oscillations as well as shifting the onset potential to slightly higher values. The concentration of sulfide in solution has a large impact on the location and amplitude of the observed potential oscillations. Increasing the concentration shifted the potential oscillations to higher current densities as well as shifting the onset potential to slightly higher values. EIS studies further showed that the onset of negative impedance increases in potential with increasing sulfide concentration; and equivalent circuit models were developed to fit the impedance spectra. Temperature also significantly influences the behavior of potential oscillations. Increasing

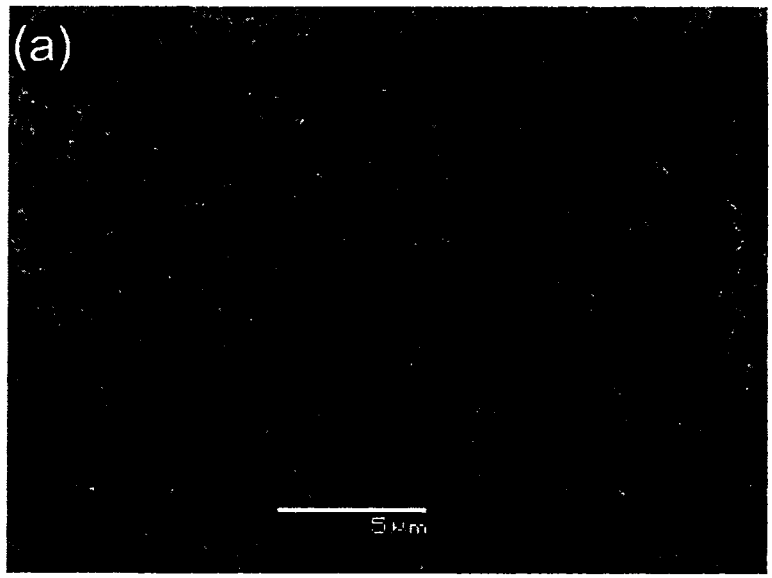

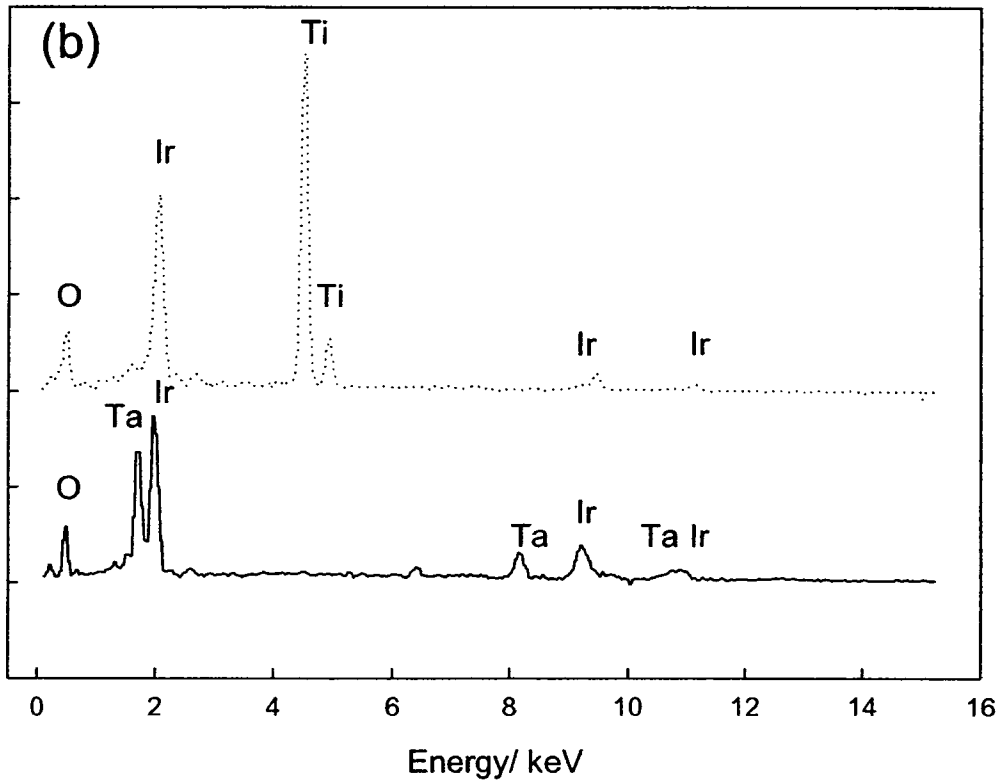

Figure 5.11. (a) SEM image of deactivated Ta_2O_5-IrO_2 electrode. Magnification: x 10000; (b) EDS spectra of initial (solid line) and deactivated (dotted line) Ta_2O_5-IrO_2 anode.

temperature shifts the location of the oscillations to much higher current densities. The activation energy of sulfide oxidation was estimated as 24 kJ/mol based on the Arrhenius plot. Finally, the effect of potential oscillations on electrode lifetime was also investigated. It was found that potential oscillations appear to have a detrimental impact on the electrode lifetime. In addition, it was determined that the preferential dissolution of Ta_2O_5 exposed the Ti substrate to the electrolyte. This exposure of the substrate allows for the formation of an anodically grown insulting TiO_2 interlayer which is the main reason for the deactivation of the Ta_2O_5-IrO_2 electrode during sulfide oxidation.

Chapter 6

Summary

The ability to effectively reduce or eliminate sulfide emissions from waste processes is becoming increasingly important as environmental regulations continue to tighten allowable limits for sulfide emissions. Currently, sulfide species are removed through adsorption, chemical oxidation and precipitation reactions [76-77]. However, these processes are expensive and it is difficult to achieve desirable economical benefits [78]. On the other hand, electrochemical oxidation of aqueous and gaseous sulfide has garnered significant attention for detection and removal/conversion of the highly toxic sulfide species [37, 39, 44-48]. However, the mechanisms of sulfide oxidation and soluble polysulfide ion formation, as well as the nature of the deposited sulfur, are still not clear. In addition, oxyanions of sulfur such as thiosulfate and sulfate can also be formed. Thus, further investigation of sulfide oxidation is critical in order to effectively remove sulfide from wastewater streams and convert sulfide economically into polysulfides for use in the kraft pulping process.

During my M. Sc. program, I studied electrochemical oscillations (which play an important role in the study of nonlinear dynamics) during the anodic oxidation of aqueous sulfide on Pt and Ta_2O_5-IrO_2 electrodes. To accomplish this I used a number of electrochemical methods (*e.g.*, cyclic voltammetry, cyclic and linear galvanic voltammetry, differential capacitance, chronoamperommetry, chronopotentiommetry, galvanostatic technique, and electrochemical impedance spectroscopy). Also, surface analytical techniques such as scanning electron microscopy (SEM) and energy dispersive

X-ray spectroscopy (EDS) were used to study changes in the composition and structure of the Ta_2O_5-IrO_2 electrode. The main results of my studies are summarized below.

6.1. Electrochemical oxidation of sulfide on a Pt electrode

The oxidation of sulfide on a Pt electrode demonstrated a current oscillation, and two potential oscillations (Oscillations α and β). A bistability feature has also been observed. The current oscillations are thought to be caused by periodic formation and removal of PtO_x and sulfur deposits. The removal of PtO_x is most likely accomplished through reduction with sulfide. The sulfur deposits can be removed by a number of different mechanisms including polysulfide and sulfate formation. The two potential oscillations labeled α and β have been classified as hidden negative differential resistance (HNDR) type oscillators using EIS. Oscillation α appears at low current densities with amplitude of 0.3 V and is caused by the formation and removal of sulfur on the Pt surface, which turns the direct oxidation of S^{2-}/HS^- to polysulfides on and off. Oscillation β occurs at higher current densities with the electrode potential ranging between 1.4 and 1.8 V. Oscillation β occurs on a PtOx surface that is formed at higher potentials from the Pt metal. The oscillation is due to the combined effects of sulfur formation and removal in concert with constant oxygen evolution. The bistability feature observed during the oxidation of sulfide is a result of a change in the surface state of the electrode. In regions of low potential, sulfide is oxidized on a Pt surface. At high potentials Pt is converted to PtO_x and sulfide is oxidized on the PtO_x surface.

6.2. Electrocatalytic oxidation of sulfide on a microstructured Ti/Ta_2O_5-IrO_2 electrode

The Ta_2O_5-IrO_2 electrode used in this study exhibits the typical cracked mud structure (SEM analysis) traditionally seen of oxide electrodes prepared from the thermal decomposition technique. Particles of IrO_2 (~100 nm) sit on top of the cracked mud structure, further enhancing the surface area. During the electrooxidation of sulfide on this electrode two distinct potential oscillatory regions were observed. Oscillation A ranged from 20 to 45 mA cm^{-2} and oscillation B from 55 to 75 mA cm^{-2}. The features of the oscillations depend on the applied current density. Oscillation A is due to variations in the HS^-/S^{2-} surface concentration caused by oxidative depletion of HS^-/S^{2-} and the replenishment of HS^-/S^{2-} by periodic oxygen evolution. Oscillation B is caused by sulfur formation/removal combined with constant gas evolution. Our EIS studies have demonstrated that these oscillations can be classified into a new type of HNDR oscillator that involves oxygen evolution, indicating that mass transport plays a critical role in the generation of the oscillations.

Investigations were conducted into the impact of current density, concentration, and temperature on the oxidation of sulfide and the behavior of the oscillations. It was determined that raising current density increases both the frequency and the onset potential of the oscillations. Raising the concentration of sulfide yields a significant increase in the current density and onset potential of the oscillation. The increase in current density and onset potential are thought to be a result of the increase in S^{2-} concentration which chemically dissolves the sulfur layer faster than it can form. The

higher sulfide concentrations would require higher current densities before a sufficient sulfur layer is formed causing oscillations to occur. EIS studies showed that the onset potential of negative impedance increases with increasing concentration. Raising temperature causes a significant increase in current density prior to the onset of oscillations, indicating that the formation of the sulfur layer is impeded. There are two reasons for this: (1) increased mass transfer of HS^-/S^{2-} ions from the bulk solution to the electrode surface; and (2) enhanced sulfur dissolution and polysulfide formation. The activation energy for the electrochemical oxidation of sulfide was estimated to be 24 kJ/mol. We also investigated the impact of the potential oscillations on electrode lifetime and subsequently proposed a deactivation mechanism for the Ta_2O_5-IrO_2 electrode during sulfide oxidation. It was determined that potential oscillations have a detrimental impact on electrode lifetime and that the preferential dissolution of Ta_2O_5 exposed the Ti substrate to the electrolyte. This exposure of the Ti substrate allowed for its oxidation to an insulating TiO_2 interlayer and this insulating interlayer is the main cause of the deactivation of the Ta_2O_5-IrO_2 electrode during sulfide oxidation.

6.3. Comparison of the electrochemical oscillations during sulfide oxidation

To understand further the behavior of oscillatory instabilities during sulfide oxidation we compared the performance of Pt and Ta_2O_5-IrO_2 under potential and current control. Figure 6.1 presents potential linear voltammograms of (a) Pt and (b) Ta_2O_5-IrO_2

in 1.0 M Na_2S at a sweep rate of 1 mV/s. In Figure 6.1a, oscillations are observed at higher potential regions during the slow sweep rate scan, with the amplitude and frequency of the oscillations being dependent on the applied electrode potential. Conversely, no oscillations are observed during the slow sweep rate scan with the Ta_2O_5-IrO_2 electrode shown in Figure 6.1b; all that appears is a broad hump centred at ~-0.1 V. This indicates that the current oscillations are highly dependent on the electrode surface where both hydroxide and sulfur have weak adsorption on Ta_2O_5-IrO_2 and strong adsorption on the Pt surface. Figure 6.2 shows a series of galvanostatic curves of Pt in 1.0 M Na_2S: (a) 5 mA/cm^2, (b) 50 mA/cm^2 and Ta_2O_5-IrO_2 in 0.65 M Na_2S: (c) 30 mA/cm^2, (d) 60 mA/cm^2. The amplitude of the oscillation in the case of Pt (fig 6.2a) is quite small (0.15 V) compared to that of Ta_2O_5-IrO_2 (1.5 V) (figure 6.2c) but the frequency is significantly higher. At low current densities we can see that the oscillatory behavior of these electrodes is quite different, this is consistent with the proposed mechanisms. The variation of the $S^{2-}/HS^-/OH^-$ surface concentration from diffusion and oxidation, the deposit of sulfur on the Pt surface, and the removal of sulfur from the Pt surface through forming soluble polysulfides are the main reasons for Oscillation α. The variation of the S^{2-}/HS^- surface concentration from the diffusion-limited depletion by oxidation and from the convection-induced replenishment by periodic oxygen evolution is the main reason for oscillation A. However, at high current densities both Oscillation β and Oscillation B show somewhat irregular behavior, and have small amplitudes and high frequencies. Oscillation B is caused by the synergic effect of sulfur formation/removal and constant oxygen evolution. Consequently, Oscillation β is observed at the high potential range, where the surface concentration

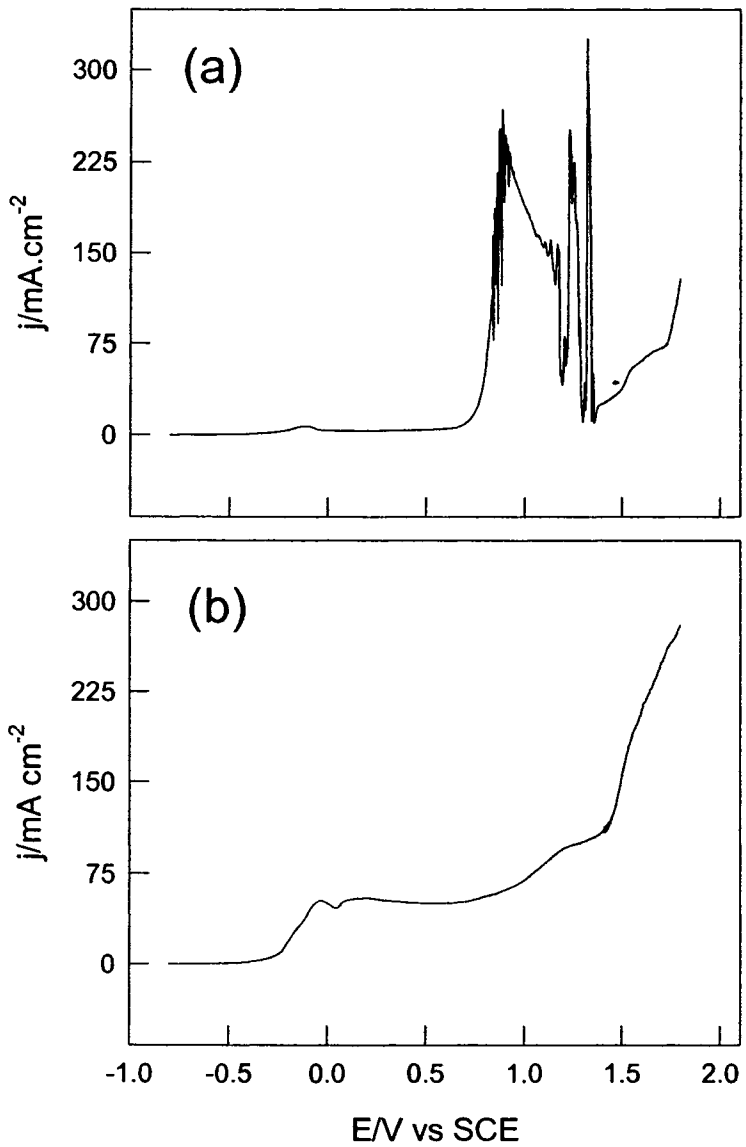

Figure 6.1. Potential linear voltammogram of (a) Pt and (b) Ta_2O_5-IrO_2 in 1.0 M Na_2S at a sweep rate of 1 mV/s.

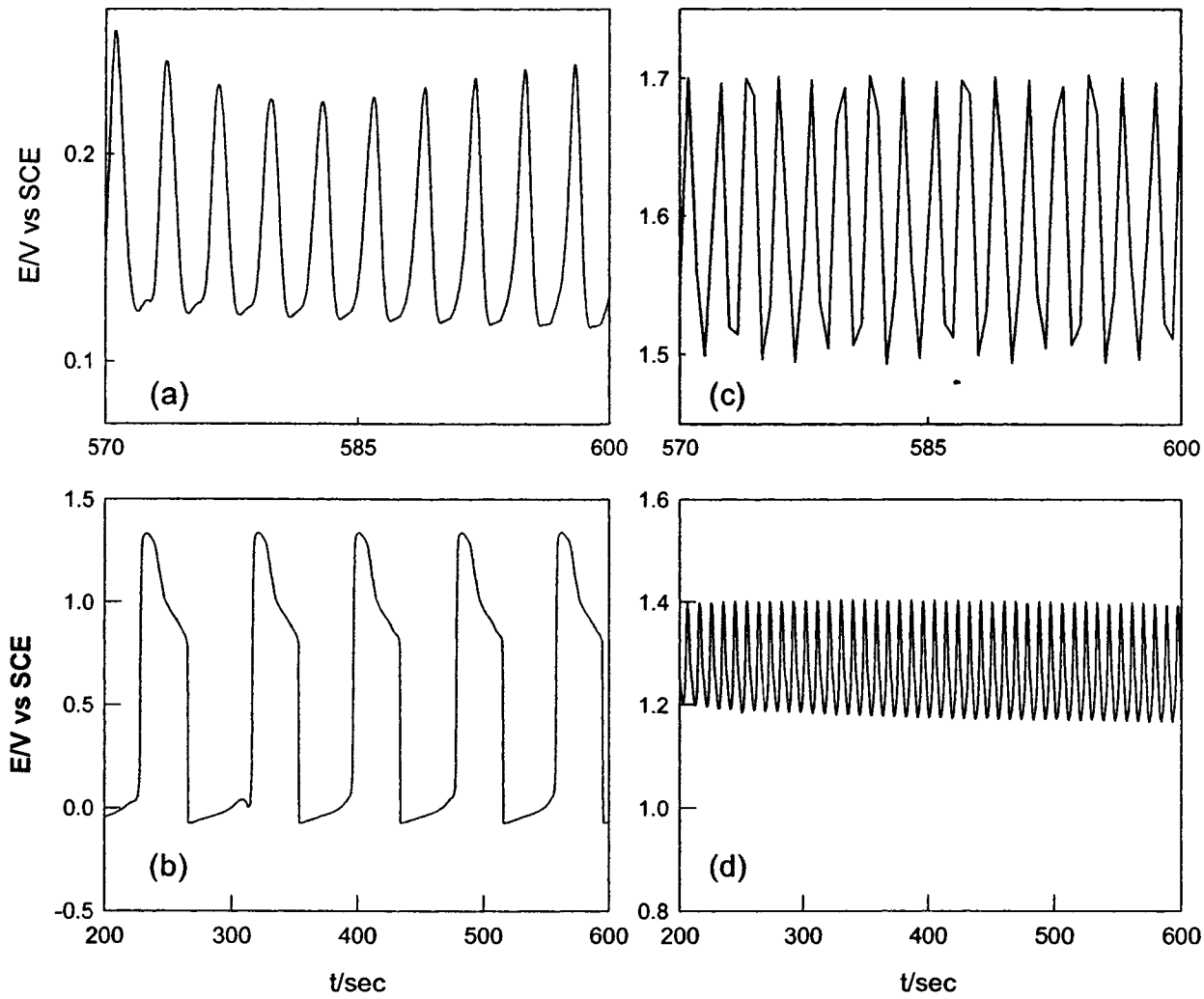

Figure 6.2. GS curves of Pt (a) 5 mA/cm^2 (b) 50 mA/cm^2 in 1.0 M Na_2S and Ta_2O_5-IrO_2 (c) 30 mA/cm^2 (d) 60 mA/cm^2 in 0.65 M Na_2S.

of S^{2-}/HS^- depletes rapidly (high frequency), and the oxygen evolution becomes predominant. This prevents the S^{2-}/HS^- surface concentration from completely restoring giving a smaller amplitude. As a result, oxygen evolution behaves continuously and the surface sulfur deposits remain although their quantities may vary from time to time (irregular) indicating that the same mechanism occurs for both systems at higher current densities.

Overall, the finding of electrochemical oscillations using both Pt and Ta_2O_5-IrO_2 has advanced the understanding of the electrochemical oxidation of sulfide, providing insight into the development of more efficient electrochemical processes to treat sulfide waste streams and to convert sulfide into polysulfides for the white liquor of the kraft pulping process

References

[1] E. S. Hedges, J. E. Meyers, *The Problem of Physico-chemical Periodicity*, Arnol, London, 1926.

[2] H. Degn, *J. Chem. Soc., Faraday Trans.*, **1968**, 64, 1348.

[3] P. Russel, J. S. Newman, *J. Electrochem. Soc.*, **1986**, 133, 2093.

[4] M. Schell, F. N. Albahadily, J. Safar, Y. Xu, *J. Phys. Chem.*, **1989**, 93, 4806.

[5] J. Wojtowicz, N. Marincic, B. E. Conway, *J. Chem. Phys.*, **1968**, 48, 4333.

[6] M Hachkar, M. Choy de Martinez, A. Rakotondrainibe, B. Beden, C. Lamy, *J. Electroanal. Chem.*, **1991**, 302, 173.

[7] T. J. Schmidt, B. N. Grgur, N. M. Markovic, P. N. Jr. Ross, *J. Electroanal. Chem.*, **2001**, 500, 36.

[8] P. Strasser, M. Eiswirth, G. Ertl, *J. Chem. Phys.*, **1997**, 107, 991.

[9] P. Strasser, M. Lübke, F. Raspel, M. Eiswirth, G. Ertl, *J. Chem. Phys.*, **1997**, 107, 979.

[10] M. Krausa, W. Vielstich, *J. Electroanal. Chem.*, **1995**, 399, 7.

[11] Y. Mukouyama, S. Nakanishi, H. Konishi, Y. Ikeshima, Y. Nakato, *J. Phys. Chem. B*, **2001**, 105, 10905.

[12] S. Nakanishi, Y. Mukouyama, K. Karasumi, A. Imanishi, N. Furuya, Y. Nakato, *J Phys. Chem. B*, **2000**, 104, 4181.

[13] G. Flatgen, S. Wasle, Lübke, C. Eickes, G. Radhakrishnan, K. Doblhofer, G. Ertl, *Electrochim. Acta*, **1999**, 44, 4499.

[14] S. Nakanishi, S. Sakai, M. Hatou, Y. Mukouyama, Y. Nakato, *J. Phys. Chem. B*, **2002**, 106, 2287.

[15] Z. L. Li, B. Ren, X. M. Xiao, Y. Zeng, X. Chu, Z. Q. Tian, *J Phys. Chem. B*, **2002**, 106, 6570.

[16] E. V. Radkov, L. G. Ljutov, *J. Electroanal. Chem.*, **1988**, 241, 349.

[17] Z. L. Li, J. L. Cai, S. M. Zhou, *J. Chem. Soc. Faraday Trans.*, **1997**, 19, 3519.

[18] K. Krischer, in R.C. Alkire, D.M. Kolb (Eds.), *Advances in Electrochemical Science and Engineering Vol. 8*, Wiley, 2003, Ch. 2.

[19] J. Wojtowicz, in J. Bockris, B. Conway (Eds.), *Modern Aspects of Electrochemistry, Vol. 8*, Butterworths, London, 1973, p 47.

[20] M. T. M. Koper, *J. Chem. Soc., Faraday Trans.*, **1998**, 94, 1369.

[21] P. Strasser, M. Eiswirth, M. T. M. Koper, *J. Electroanal. Chem.*, **1999**, 478, 50.

[22] M. T. M. Koper, *J. Electroanal. Chem.*, **1996**, 409, 175.

[23] M. T. M. Koper, J. H. Sluyters, *J. Electroanal. Chem.*, **1994**, 371, 149.

[24] M. T. M. Koper, *Electrochim. Acta*, **1992**, 37, 1771.

[25] Z. L. Li, B. Ren, X. M. Xiao, Y. Zeng, X. Chu, Z. Q. Tian, *J. Phys. Chem. A*, **2002**, 106, 6570.

[26] Z. L. Li, Q. H. Yuan, B. Ren, X. M. Xiao, Y. Zeng, Z. Q. Tian, *Electrochemistry Comm.*, **2001**, 3, 654.

[27] S. Trasatti, *Electrochim. Acta*, **2000**, 45, 2377.

[28] H. B. Beer, Brit. Patent 11 147 442, 1965.

[29] R. N. Rhoda, *Trans. Inst. Met. Finish.*, **1952**, 36, 82.

[30] A. Nidola, in S. Trasatti, (Ed.) *Electrodes of Conductive Metal Oxides, Part B*, Elsevier, Amsterdam, 1981, Ch. 11.

[31] G.P. Versesi, J. Rolewicz, Ch. Comninellis, J. Hinden, *Thermochim. Acta*, **1991**, 176, 31.

[32] F. Cardarelli, P. Taxil, A. Saval, Ch. Comninellis, G. Leclerc, *J. Appl. Electrochem.*, **1998**, 28, 245.

[33] S. Trasatti, *Electrochim. Acta*, **1991**, 36, 225.

[34] G. Lodi, C. De Asmundis, S. Ardizzone, E. Sivieri, S. Trasatti, *Surf. Technol.*, **1981**, 14, 335.

[35] Ch. Comninellis, G.P. Vercesi, *J. Appl. Electrochem.*, **1991**, 21, 335.

[36] R. Kötz, S. Stucki, *Electrochim. Acta*, **1986**, 31, 1311.

[37] B. G. Ateya, F. M. Al-Kharafi, *Electrochem. Comm.*, **2002**, 4, 231.

[38] R. Quinn, T. A. Dahl, B. A. Toseland, *Appl. Cat. A*, **2004**, 272, 61.

[39] L. G. Shaidarova, L. G. Popesku, G. K. Budnikov, *Russ. J. Appl. Chem.*, **1998**, 71, 811.

[40] M. Behm, D. Simonsson, *J. Appl. Electrochem.*, **1997**, 27, 507.

[41] J. Szynkarczuk, P.G. Komorowski, J.C. Donni, *Electrochim. Acta,* **1994**, 39, 2285.

[42] W. M. Latimer, *The Oxidation States of the Elements and Their Potentials in Aqueous Solutions, 2nd ed.*, Prentice Hall, Inc., Englewood Cliffs, N. J., 1952.

[43] J. Szynkarczuk, P.G. Komorowski, J.C. Donni, *Electrochim. Acta*, **1994**, 40, 487.

[44] Z. Mao, A. Anani, R.E. White, *J. Electrochem. Soc.*, **1991**, 138, 1299.

[45] A.A. Anani, Z. Mao, R.E. White, S. Srinivason, A.J. Appleby, *J. Electrochem. Soc.*, **1990**, 137, 2703.

[46] Q. Yi, Q. Chen, J. Zhou, P. Zang, *Trans. Nonferrous Met. Soc. China*, **2000**, 10, 534.

[47] Q. Yi, Q. Chen, P. Zhang, J. Zhou, *Aust. J. Chem*, **2000**, 53, 557.

[48] T. Rozan, S.M. Theberge, G. Luther III, *Anal. Chim. Act.*, **2000**, 415, 175.

[49] H. Helms, E. Schlomer, W. Jansen, *Monatsh. Chem.*, **1998**, 129, 617.

[50] T. Loucka, *J. Electroanal. Chem.*, **1971**, 31, 319.

[51] S. Kapusta, A. Viehbeck, S.M. Wilhelm, N. Hackerman, *J. Electroanal. Chem.*, **1983**, 153, 157.

[52] Q.F. Yi, *Acta Phys-Chim. Sin.*, **2000**, 16, 263.

[53] M. Behm, D. Simonsson, *J. Appl. Electrochem.*, **1999**, 29, 521.

[54] A.N. Buckley, I.C. Hamilton, *J. Electroanal. Chem.*, **1987**, 216, 213.

[55] D.G. Wierse, M.M. Lohrengel, J.W. Schultze, *J. Electroanal. Chem.*, **1978**, 92, 121.

[56] K. J. Umiker, M. J. Morra, I. F. Cheng, *Microchem. J.*, **2002**, 73, 287.

[57] W. Giggenbach, *Inorganic Chem.*, **1972**, 11, 1201.

[58] E. Lamy-Pitara, J. Barbier, *Electrochim. Acta*, **1986**, 31, 717.

[59] A. J. Bard, L. R. Faulkner, Electrochemical Methods: *Fundamentals and Applications 2nd ed.*, John Wiley & Sons, New York, 2001.

[60] U. Retter, H. Lohse, in F. Scholz (Ed.) *Electroanalytical Methods: Guide to Experiments adn Applications,* Springer-Verlag, Berlin, 2002, p 149.

[61] Autolab Electrochemical Instruments, *Theory and Practical Aspects of Electrochemical Impedance Measurements*, Application Note.

[62] Princeton Applied Research, *Basics of Electrochemical Impedance Spectroscopy,* Application Note AC-1

[63] G. Popkirov, R. Schindler, *Rev. Sci. Instrum.*, **1993**, 64, 3111.

[64] A. Chen, Z. Shi, D. Bizzotto, J. Lipkowski, C. Bilger, *J. Electroanal. Chem.*, **1999**, 467, 342.

[65] R. E. Melnick, G. T. R. Palmore, *J. Phys Chem B*, **2001**, 105, 1012.

[66] R. E. Melnick, G. T. R. Palmore, *J. Phys Chem B*, **2001**, 105, 9449.

[67] L. D. Burke, in S Trasatti, G. Lodi (Eds.), *Electrodes of Conductive Metallic Oxides, Part A,* Elsevier, Amsterdam, 1980, Ch. 7.

[68] S. G. Sun, A. Chen, *J. Electroanla. Chem.*, **1992**, 323, 319.

[69] A. Chen, S. Nigro, *J. Phys. Chem. B*, **2003**, 105, 13341.

[70] V. A. Alves, L. A. da Silva, J. F. C. Boodts, *J. Appl. Electrochem.*, **1998**, 28, 1998.

[71] L. M. da Silva, L. A. De Faria, J. F. C. Boodts, *Electrochim. Acta,* **2003**, 48, 699.

[72] G. N. Martelli, R. Ornelas, G. Faita, *Electrochim. Acta*, **1994**, 39, 1551.

[73] A. S. Pilla, E. O. Cobo, M. M. E. Duarte, D. R. Salinas, *J. Appl. Electrochem.*, **1997**, 27, 1283.

[74] T. A. F. Lassali, J. F. C. Boodts, L. O. S. Bulhoes, *J. Appl. Electrochem.*, **2000**, 30, 625.

[75] B. V. Tilak, C. P. Chen, V. I. Birss, J. Wang, *Can. J. Chem.*, **1997**, 75, 1773.

[76] B. Mayer, *Sulphur, Energy and Environment*, Elsevier, Amsterdam, 1987, Ch. 7.

[77] L. Gaverick, (Ed.), *Corrosion in the Petrochemical Industry*, ASM International, Metals Park, OH, 1997, p. 259.

[78] J. E. Noring, E. A. Fletcher, Energy, **1982**, 7, 651.